

2

PL-TR-94-2007

AD-A277 891



**INVESTIGATIONS ON LOCAL SEISMIC PHASES
AND MODELING OF SEISMIC SIGNALS**

**B. Massinon
P. Mechler**

**Radiomana - Societe Civile
27 Rue Claude Bernard
75005 Paris, FRANCE**

**DTIC
ELECTE
APR 07 1994
S E D**

31 October 1993

**Final Report
1 September 1990-31 August 1993**

94-10537

APPROVED FOR PUBLIC RELEASE; DISTRIBUTION UNLIMITED



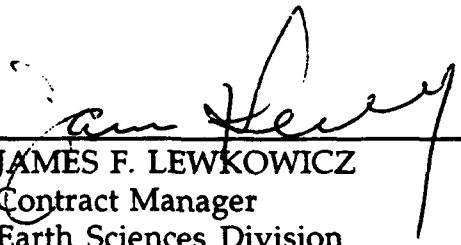
**PHILLIPS LABORATORY
Directorate of Geophysics
AIR FORCE MATERIEL COMMAND
HANSCOM AIR FORCE BASE, MA 01731-3010**

DATE QUALITY INSPECTED 3

94 4 6 05T

The views and conclusions contained in this document are those of the authors and should not be interpreted as representing the official policies, either express or implied, of the Air Force or the U.S. Government.

This technical report has been reviewed and is approved for publication.



JAMES F. LEWKOWICZ
Contract Manager
Earth Sciences Division



JAMES F. LEWKOWICZ, Director
Earth Sciences Division

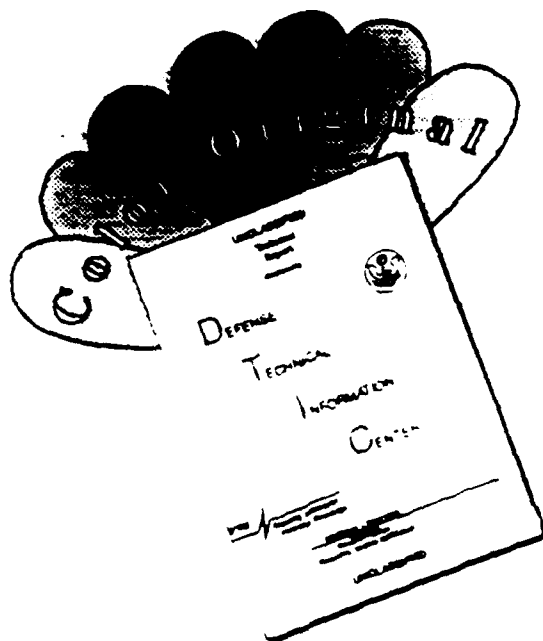
This report has been reviewed by the ESC Public Affairs Office (PA) and is releasable to the National Technical Information Service (NTIS).

Qualified requestors may obtain additional copies from the Defense Technical Information Center. All others should apply to the National Technical Information Service.

If your address has changed, or if you wish to be removed from the mailing list, or if the addressee is no longer employed by your organization, please notify PL/TSI, 29 Randolph Road, Hanscom AFB, MA 01731-3010. This will assist us in maintaining a current mailing list.

Do not return copies of this report unless contractual obligations or notices on a specific document requires that it be returned.

DISCLAIMER NOTICE



THIS DOCUMENT IS BEST QUALITY AVAILABLE. THE COPY FURNISHED TO DTIC CONTAINED A SIGNIFICANT NUMBER OF COLOR PAGES WHICH DO NOT REPRODUCE LEGIBLY ON BLACK AND WHITE MICROFICHE.

REPORT DOCUMENTATION PAGE

Form Approved
OMB No. 0704-0188

Public reporting burden for this collection of information is estimated to average 1 hour per response, including the time for reviewing instructions, searching existing data sources, gathering and maintaining the data needed, and completing and reviewing the collection of information. Send comments regarding this burden estimate or any other aspect of this collection of information, including suggestions for reducing this burden, to Washington Headquarters Services, Directorate for Information Operations and Reports, 1215 Jefferson Davis Highway, Suite 1204, Arlington, VA 22202-4302, and to the Office of Management and Budget, Paperwork Reduction Project (0704-0188), Washington, DC 20503.

1. AGENCY USE ONLY (Leave blank)	2. REPORT DATE 31 October 1993	3. REPORT TYPE AND DATES COVERED Final (1 Sept 1990-31 Aug 1993)
4. TITLE AND SUBTITLE Investigations on Local Seismic Phases and Modeling of Seismic Signals		5. FUNDING NUMBERS PE: 61101E PR 0A10 TA DA WU AD
6. AUTHOR(S) B. Massinon P. Mechler		Contract AFOSR-90-0356
7. PERFORMING ORGANIZATION NAME(S) AND ADDRESS(ES) Radiomana - Societe Civile 27 Rue Claude Bernard 75005 Paris, FRANCE		8. PERFORMING ORGANIZATION REPORT NUMBER
9. SPONSORING/MONITORING AGENCY NAME(S) AND ADDRESS(ES) Phillips Laboratory 29 Randolph Road Hanscom AFB, MA 01731-3010		10. SPONSORING/MONITORING AGENCY REPORT NUMBER PL-TR-94-2007
Contract Manager: James Lewkowicz/GPEH		

11. SUPPLEMENTARY NOTES

12a. DISTRIBUTION/AVAILABILITY STATEMENT Approved for public release; distribution unlimited	12b. DISTRIBUTION CODE
--	-------------------------------

13. ABSTRACT (Maximum 200 words)

During this three years period of activity we have worked on the basic topic of our grant that is to say 'Investigations on local seismic phases and modeling of seismic signals' but we have also enlarged this resarch in some cases to teleseismic distances. We also worked on data processing of seismic waves recorded at regional distances by a mini-array in order to improve the capability of automatic detection and localisation of events.

Within the frame of the study of regional phases, we have used methods of numerical simulation to model data from the french and spanish seismic networks in order to study the influence of crustal heterogeneities on the attenuation of these phases.

DTIC QUALITY INSPECTED 3

14. SUBJECT TERMS Simulation Regional phases Mini-array	Correlation Neuronal network Localization	Nuclear explosion Topography Geology	15. NUMBER OF PAGES 128
			16. PRICE CODE
17. SECURITY CLASSIFICATION OF REPORT Unclassified	18. SECURITY CLASSIFICATION OF THIS PAGE Unclassified	19. SECURITY CLASSIFICATION OF ABSTRACT Unclassified	20. LIMITATION OF ABSTRACT SAR

CLASSIFIED BY:

DECLASSIFY ON:

The approach is done in two parts : first, the analysis and modelisation of Lg waves which propagate through the Pyrenean Chain ; second, a numerical simulation study of the propagation and of the diffraction of S and Lg waves in irregular crustal models. The aim of these two studies is to better understand the main characteristics of seismic waves at regional distances (100 to 1000 km from the earthquakes or the explosion) and more precisely to understand how the complexity of geological and tectonical structures might affect their propagation.

Within the same frame of studies we investigate the propagation of Lg waves in laterally-varying crustal structures by numerical simulation. The results show that the Lg wave amplitude is only slightly affected by the presence of these heterogeneities and they confirm the robustness of Lg wave propagation in presence of lateral heterogeneities observed in other simulations. They show that large scale geometry features of the crust cannot account alone for the strong attenuation of Lg waves observed in many regions but suggest a possible relation between the level of Lg wave coda and the degree of roughness of the Moho.

Besides that research program, we have model for two test sites, the Nevada Test Site and the Hoggar Test Site, the wave field propagating at local and teleseismic distances. This numerical simulation which takes into account the site structure and the topography effects, propagates up to teleseismic distances waves forms with amplitudes anomalies in good agreement with the waves forms recorded on the french seismic network (case of NTS). Concerning the french test site of Hoggar, we have for now studied the influence of the topography on the shape and the amplitude of seismograms recorded at short distances from the sources.

The third part of our research program concerns different aspects of data processing adapted to a mini-array both on teleseisms and regional events detection and location.

An interesting method of location different from the classical f-k method has been investigated and gives already good results in terms of accuracy and flexibility. It is based on cross-correlation processing and Chasles relationship for resolution.

Automatic phase identification for regional phases using neuronal networks adapted to the output of the mini-array processing (velocity at various frequencies for each regional phase) has been developed.

CONTENTS

I.	Regional Waves Propagation	2
	I-1 Crustal Wave Propagation Anomaly Across the Pyrenean Range	2
	I-2 Calculation of Synthetic Seismograms in a Laterally Varying Medium by the Boundary Element Discrete Wavenumber Method	3
	Crustal Wave Propagation Anomaly Across the Pyrenean Range. Comparison Between Observations and Numerical Simulations	4
	Calculation of Synthetic Seismograms in a Laterally-Varying Medium by the Boundary Element - Discrete Wavenumber Method	23
II.	Modeling of Seismic Waves Generated by Nuclear Tests in the NTS and Taourirt Tan Afella, Hoggar	55
	II-1. Teleseismic Wave Form Modeling Including Geometrical Effects of Superficial Geological Structures Near the Seismic Sources at the NTS	55
	II-2. Modeling of French Nuclear Tests in Taourirt Tan Afella Massif, Hoggar, Sahara	55
	Teleseismic Waveform Modeling Including Geometrical Effects of Superficial Geological Structures Near to Seismic Sources	56
	Modeling of French Nuclear Tests in Taourirt Tan Afella massif, Hoggar, Sahara	75
III.	Data Processings Associated With a Mini-Array Recently Built in the Center of France	94
	III-1 Detection and Phase Identification Capabilities	94
	III-2 Automatic Processing of Seismic Events Recorded on a Mini-Array (Signal Analysis Combined With Neural Networks)	96
	Earthquake Location Applied to a Mini-Array: K-Spectrum versus Correlation Method	99

Automatic Processing of Seismic Events Recorded on a Mini-Array 103
(Signal Analysis Combined With Neural Networks)

The Giat Mini-Array in Central France: Preliminary Detection 110
and Phase Identification Results

Accession For	
NTIS CRA&I	<input checked="" type="checkbox"/>
DTIC TAB	<input type="checkbox"/>
Unannounced	<input type="checkbox"/>
Justification	
By	
Distribution /	
Availability Codes	
Dist	Avail and/or Special
A-1	

DARPA SCIENTIFIC REPORT 91-93

During these three years of activity we have concentrated our efforts on the following subjects :

- I - Regional waves propagation and attenuation which are one of our basic topics for several years,**

- II - Modeling of local and teleseismic waves generated by underground nuclear explosions in the NTS and in the Hoggar Massif, Sahara.**

- III - First data processing associated with a mini-array recently built in the Center of France.**

I - Regional waves propagation :

I - 1 Crustal wave propagation anomaly across the Pyrenean Range :

Following our previous studies, we are using Lg records analysis and numerical modelling of Lg propagation to find out to what extent this phase can be seen as a marker of unidentified structural anomalies within the crust.

This study is based on Lg propagation through the Pyrenean range from earthquakes located in Spain.

We have first evaluated the mean value of the S-wave quality factor for Central-Spain. We have computed simultaneously the seismic station responses and the source functions. The correction for propagation effects, assuming an homogenous attenuation and the theoretical evaluation of the Lg excitation lead to the seismic moment of each event. The moment magnitude we obtained fits the magnitude proposed by the local networks.

This gives the confirmation of the Q model in the low frequency range (1-5Hz). As we intended to compare traces of different Spanish earthquakes recorded in France at different epicentral distances, we had to make amplitudes independent of propagation and sources effects. Therefore we corrected the spectral amplitudes for geometrical spreading, anelastic attenuation and normalized them to equal seismic moment.

We then plotted the records as a function of group velocity, in order to make up a fan profile along the Pyrenean axis. The resulting section reveals that in the central and the eastern parts of the range, neither the North-Pyrenean-Fault, nor the Moho jump deduced from seismic-refraction experiments and vertical seismics, seem to affect the Lg propagation. However, there is an extinction of the Lg phase in the western part of the chain. The lateral extent of this area is correlated with a zone of positive gravity anomaly, probably linked to the presence of dense material of mantle origin.

A numerical simulation in the low frequency band indicates that the Moho topography inferred from deep seismic soundings does not explain the strength of the observed attenuation. Ray-tracing seismograms show that, at high frequency, the conclusion is the same.

The attenuation effect of the structure lateral variation should not be so strong. We therefore think that attenuation of guided waves is not basically due to large scale geometry effects, but more probably to local properties of the crustal materials, possibly apparent attenuation due to scattering on small scale heterogeneities.

This work has been submitted to the Geophysical Journal and revised in march 1993.

I - 2 Calculation of synthetic seismograms in a laterally varying medium by the boundary element discrete wavenumber method :

We present a theoretical investigation of the effect of lateral crustal heterogeneities on the propagation of seismic waves. We study particularly how Lg waves are affected by the crossing of complex crustal structures. The work is carried out by numerical simulation and the method of calculation is based on boundary integral / boundary element techniques. The Green's functions necessary to the implementation of these techniques are evaluated in the frequency - wavenumber domain using the discrete wavenumber method and reflectivity/transmissivity matrices. This formulation has the advantage over purely numerical methods of allowing the calculation of the wavefields over large distances (several hundred kilometers) corresponding to several hundred times the wavelengths.

We investigate how crustal waves are affected by the crossing of faults and by the presence of lateral variations in crustal thickness. We find that the Lg waveforms are extremely sensitive to the presence of lateral heterogeneities along their path, but that their energy stays remarkably stable as long as the heterogeneities encountered are not too strong. On the basis of the theoretical results obtained, the observations of Lg wave extinction or strong attenuation over specific continental paths are difficult to explain by purely geometric diffraction and scattering.

The numerical simulation results also show that the back scattered Lg wavefield induced by lateral variations in crustal thickness can be strong. This suggests that in real observations part of the Lg wave coda is due to back scattering and that the level of coda present might be related to the roughness of the Moho.

CRUSTAL WAVE PROPAGATION ANOMALY ACROSS THE PYRENEAN RANGE. COMPARISON BETWEEN OBSERVATIONS AND NUMERICAL SIMULATIONS

A. Chalazon¹, M. Campillo¹, R. Gibson² and E. Carreno³

¹ Laboratoire de Géophysique Interne et Tectonophysique, I. R. G. M. BP 53 X, 38041 GRENOBLE CEDEX FRANCE.

² Earth Resources Laboratory M. I. T., 42 Carleton St. Cambridge, MA 02142 USA.

³ Servicio de Ingeniería Sísmica, Instituto Geográfico Nacional, Gral Ibañez Ibero 3, 28003 MADRID, SPAIN

Accepted 1993 April 23 Received 1993 March 31 ; in original 1992 November 10.

SUMMARY

Lg records analysis and numerical modelling of *Lg* propagation are used to find out to what extent this phase can be seen as a marker of unidentified structural anomalies in the crust. This study is based on *Lg* propagation through the Pyrenean range from earthquakes located in Spain.

We have first evaluated the mean value of the *S*-wave quality factor for Central Spain. We have computed simultaneously the seismic station responses and the source functions. The correction for propagation effects, assuming a homogeneous attenuation and the theoretical calculation of the *Lg* excitation, lead to the seismic moment of each event. The moment magnitude obtained correlates well with the magnitude proposed by the local networks. This gives a confirmation of the *Q* model in the low frequency range (1-5Hz). As we intended to compare traces of different Spanish earthquakes recorded in France at different epicentral distances, we had to make amplitudes independent of propagation and source effects. Therefore, we corrected the spectral amplitudes for geometrical spreading, anelastic attenuation and normalized them to equal seismic moment.

We then plotted the records as a function of group velocity, in order to make up a fan profile along the Pyrenean axis. The resulting section reveals that in the central and the eastern parts of the range, neither the North-Pyrenean-Fault, nor the Moho jump deduced from seismic-refraction experiments and vertical seismics, seem to affect *Lg* propagation. However, there is an extinction of the *Lg* phase in the western part of the chain. The lateral extent of this area is correlated with a zone of positive gravity anomaly, probably linked to the presence of dense material of mantle origin. A numerical simulation in the low frequency band indicates that the Moho topography inferred from deep seismic soundings does not explain the strength of the observed attenuation. Ray-tracing seismograms show that, at high frequency the conclusion is the same. The attenuation effect of the structure lateral variation should not be so strong. We, therefore, think that attenuation of guided waves is not due to large-scale geometry effects, but is due to local properties of the crustal materials, possibly apparent attenuation due to scattering on small-scale heterogeneities.

Key words : *Lg* waves, Pyrenees, quality factor, synthetic seismograms.

INTRODUCTION

In the range between 150 and several thousand kilometres, crustal waves are dominant on short-period seismograms in continental areas. Thus, the *Lg* phase, which consists of *S* waves trapped in the crust, is the major phase observed on regional records.

Lg amplitude is known to be sensitive to important changes in crustal structure: propagation paths through oceanic crust are the origin of high attenuation or extinction of the *Lg* phase, as found in the early analysis of this phase (Press & Ewing 1952; Bath 1954). Zones of strong local weakening of *Lg* also exist in continental domains. Such observations have been reported in the Himalayan Belt (Ruzaikin *et al.* 1977), in the North Sea Graben (Kennett *et al.* 1985), in the Eurasian Shield (Baumgardt 1991) and in the south-western part of the Alpine range (Campillo *et al.* 1993).

It seems that some geological features partially or completely stop crustal guided wave propagation. Our purpose is to investigate what structure may produce these *Lg* amplitude variations and blockage effects. Is it a large-scale geometry result of a local attenuation or scattering effect? As there already exists evidence of an *Lg* propagation anomaly in the Western Alps, our study has been aimed at the analysis of *Lg* propagation across the Pyrenean range, in order to improve our knowledge about the influence of such orogenic structures.

DATA SPECIFICATIONS

For this study, we have used Spanish and French data obtained by the IGN (Instituto Geografico Nacional) array and the LDG (Laboratoire de Détection Géophysique) network respectively. All seismic stations are short-period vertical instruments with natural period of 1s. The characteristics of the networks are described in an IGN report (IGN 1991) and by Nicolas *et al.* (1982) for the LDG network. We have examined records available from these two networks and we confirmed that *Lg* waves effectively propagate in France and in Spain, on both sides of the Pyrenean range. As we intended to study the propagation from natural sources located in Spain, to see whether or not *Lg* waves are able to cross the Pyrenees, we had to determine the anelastic attenuation of the crustal phases in Spain.

The data set consists of 12 earthquakes with hypocentres in the crust, recorded in Spain. Their parameters are described in Table 1. As is the case in most continental areas, *Lg* is the dominant phase on most of the records. The source-receiver pairs have been chosen in such a way that the propagation paths were sampling the central part of Spain, considered to be a stable continental area. We did not take into account stations located in southern Spain because we observed strong attenuation in the region of Gaudalquivir sedimentary basin Fig. 1 shows the paths used in this part of the study.

EVALUATION OF THE S-WAVE MEAN QUALITY FACTOR

To evaluate the *S*-wave mean quality factor, we used *Lg* phases that consist of multiply reflected *S* waves. Calculation of the crustal quality factor Q is done by computing the spectral density per time unit as a function of epicentral distance, in the time window providing the largest amplitudes, i.e. in the group velocity window 3.6-3.2 km s⁻¹.

For each station i and each earthquake j , this amplitude can be written in the form :

$$A_{ij}(f, d) = S_j(f) \cdot AA(f, d) \cdot E(d) \cdot ST_i(f), \quad (1)$$

f representing the frequency and d the epicentral distance. $S_j(f)$ is the source contribution, proportional to the seismic moment at low frequency $AA(f, d)$ is given by

$$\exp\left(\frac{-\pi fd}{QV_m}\right) \quad (2)$$

and represents the anelastic attenuation for a phase propagating with a mean velocity QV_m . $E(d)$ denotes the geometrical spreading in the time domain needed to correct the spectral density per time unit. It is taken in the form:

$$E(d) = d^{-0.83} \quad (\text{Campillo, Bouchon \& Massinon 1984}) \quad (3)$$

$ST_i(f)$ is the station response, corresponding to the effects of local geology structure.

This equation is solved by an iterative process given in detail by Campillo, Plantet & Bouchon (1985). Only the data obtained for earthquakes that were recorded by at least four stations, were used. We first took $ST = 1$ and evaluated the mean value of Q by least-square fitting for each earthquake. We then computed the mean value of Q for the entire set of events. ST could be evaluated by computing a simple residue at each station. This process converged after a few iterations. The root-mean-square residue between the observed amplitudes and the ones predicted by eq. 1 was computed to check the convergence and the stability. The shape of the displacement spectrum was obtained after deconvolution of the instrumental response of the IGN network stations. Thus, we got the sources-displacement spectra in m s.

We found $Q(f)$ in the form :

$$Q = (330 \pm 30) f^{0.51 \pm 0.06} \quad (4)$$

This result is close to the mean crustal quality factor computed for central France (Campillo *et al.* 1985)

ESTIMATION OF THE SEISMIC MOMENTS

We computed the seismic moment using the theoretical excitation of Lg for a point source dislocation. We neglected the radiation pattern since Lg is a superposition of S waves leaving the source in a wide range of take-off angles. To perform the estimation, we computed synthetic seismograms in a flat layered medium corresponding to the crustal structure of central Spain. Table 2 summarizes the characteristics of the model.

The theoretical calculation was performed, for a seismic moment of 1, using the discrete wavenumber representation (Bouchon 1981), combined with the Kennett propagation technique (1983). We evaluated the Lg spectral density from the synthetics in exactly the same way as for the data. We can, therefore, obtain the theoretical value of S of eq. 1 for a unit moment. For frequencies lower than the corner frequency, we can relate the seismic moment to the observed amplitudes, corrected for spreading and attenuation. To test the accuracy of our results we have calculated the Lg magnitudes from each seismic moment value, from which we deduced M_w as defined by Kanamori (1977) M_w is given by:

$$\log M_0 = 1.5M_w + 9 \quad (M_0 \text{ in Nm}). \quad (4)$$

Table 1 presents the local magnitudes reported in the bulletins and the values of our M_w magnitudes. We can see that the seismic moments measured from the Lg phase vary consistently with the magnitudes proposed by the local networks. Fig 2 shows the source spectra which allow us to find out the seismic moments and the magnitude values. We plotted all spectra on a log-log diagram, in order to compare their shape and their dimension. One can see that the corner frequency measured on our spectra varies between 3 and 8 Hz. Considering the events with seismic moment between 10^{13} and 10^{16} Nm i.e. $M_w < 5$, and assuming a self-similar model, f_c should be in the range 0.6-7 Hz for a 100 to 200 bars stress drop. Beyond f_c , the observed high-frequency spectra decrease as ω^{-2} .

The Lg magnitudes we found are systematically smaller than those given by the local networks from direct waves. We have tested that the crustal model used for the numerical simulation of Lg propagation has no significant influence on the seismic moment values. On the other hand, changes in the parameters of fault geometry cause variations in the Lg magnitudes. However, azimuthal dependence is weaker for Lg than for direct waves (Campillo 1990) because this phase is made up of a superposition of rays, sampling a wide range of take-off angles. The good agreement of the linear correlation we obtained between Lg moment magnitudes and local magnitudes confirms the possibility of using the source spectra to correct the amplitudes.

PROPAGATION ANALYSIS THROUGH THE PYRENEES

Most of the earthquakes whose records were used for the Q calculation did not provide data of adequate quality at the French stations because of the great epicentral distances. Only four events located in northern Spain provide a large enough signal-to-noise ratio: Sotos, Cucalon and the two closely spaced events Camero and Arnedo (see Fig. 1).

First we looked at the records obtained at the French station EPF, which is located in the Pyrenees, north of the North Pyrenean Fault (NPF, Fig. 3). This zone of deep subvertical faults is a major structural feature of the mountain range, clearly apparent in the oriental and in the central Pyrenees. In the western Pyrenees, it is assumed that the discontinuity is overlain by Cretaceous sediments. The NPF constitutes the limit of the North Pyrenean Zone and the axial zone of the range. The available information concerning the tectonics of the region shows that, in the central part of range (Fig. 4), an underthrust of the Iberic crust to the North takes place along the NPF (Pinet *et al.* 1987; Choukroune *et al.* 1989). On the other hand, the oceanic lithosphere in the Gulf of Biscay dives under the Iberic plate (Boillot *et al.* 1971).

For the earthquakes we examined, the seismograms recorded at EPF have the same typical shape of continental short-period records as observed at all nearby Spanish stations: the crustal wave Pg and Lg are dominant. This is illustrated in Fig. 5 (a and b): the Lg phase produces a clear onset at 3.5 km s^{-1} . However, the records obtained at stations in central France show very different characteristics. The corresponding paths are plotted in Fig. 6. In the case where the path crosses the western part of the Pyrenean Chain, the larger arrivals on the seismograms have a group velocity higher than Lg (about 4.2 km s^{-1}) and consist of the mantle wave Sn (Fig. 5c). The Lg phase vanishes along this path. For a path that crosses the central part of the chain, Sn and Lg exhibit similar amplitudes (Fig. 5d). These seismograms suggest that the regional phases are affected very differently when they cross the Pyrenees at different locations along the axis of the range.

In order to verify this effect we plotted a series of seismograms as a function of the location where the waves cross the Pyrenees. We measured the locations of the crossing along an axis from Bilbao to Perpignan shown as a thick solid line in Fig. 6. The identification of the various regional phases in the data set is simplified by plotting the records as a function of group velocity. We consider the records in France from a series of earthquakes in northern Spain (Table 3 and Fig. 6). The records are bandpassed between 1 and 5 Hz. Amplitudes are corrected for geometrical spreading, anelastic attenuation and normalized to equal seismic moment. The effect of attenuation is crudely removed from the whole seismogram by correcting the spectra with a filter defined from our results of the quality factor for S waves (eq. 4). The seismic moment used for the normalization is obtained from the least-square regression of the spectral amplitude of Lg with distance for the LDG stations. In case of a strong effect of attenuation of Lg at the crossing of the Pyrenees, the moment is underestimated. This results in an unrealistically high amplitude of the other seismic phases such as Sn .

Figure 7 presents the section obtained from these Spanish earthquakes recorded in France. One can see that the sampling is not homogeneous because of the poor distribution of earthquakes in northern Spain correctly recorded in France. However, we notice that the waveform is very different in the east and in the west side of the Pyrenean range. In the east, the maximum amplitudes appear for group velocities between 3.5 and 3.0 km s^{-1} these waves are clearly Lg phases. In the west, the largest amplitudes are seen between 4.5 and 4.0 km s^{-1} . These phases are Sn waves corresponding to upper mantle propagation.

As has already been noticed, the way we perform the normalization of seismic moment can explain why the amplitudes of Pn and Sn waves in the western part appear much higher than those in the eastern part. Another reason is the way we corrected amplitudes with distance. The amplitude corrections for spatial attenuation are strictly valid only in the group velocity window 3.2-3.6 km s^{-1} , i.e. for the Lg wave. Phases for which group velocity is greater than the Lg wave velocity are all the more amplified since epicentral distance and frequency increase. Even if the amplitude values are not exact along the entire record, this figure illustrates the Lg blockage and the relative Sn -wave amplification in the western Pyrenees. The Sn waves cannot be observed in the eastern Pyrenees because their amplitudes are much smaller than the ones of Pg and Lg . If we accept that Sn is not sensitive to crustal structure and that the mantle is almost homogeneous beneath this region, the variation of the ratio of amplitude Sn to Lg at a given distance is a crude measure of the variation of attenuation in the crust. Fig. 7 indicates that between eastern and western parts of the Pyrenees, the attenuation effect changes by more than one order of magnitude.

However, for all these earthquakes, the Lg phase can be observed at EPF station. The presence of the Lg phase in the east and at EPF indicates that the Lg blockage is not simply associated with the NPF, which lies along the entire eastern and central part of the range. On the other hand, the Lg phase vanishes when it crosses the western part of the mountain chain and the energy seems to propagate mostly as the Sn wave. This anomaly seems to have a lateral extent of about 100 km. It is noteworthy that this zone of attenuation corresponds to a zone of strong positive gravity anomaly called the 'Labourd anomaly', whose origin is not definitively known. The areas with positive Bouguer anomaly are shown in grey in Fig. 6. A similar anomaly of propagation of the crustal phase Lg has been reported in the western Alps (Campillo *et al.* 1993), correlated with a positive Bouguer anomaly. Crustal materials of deep origin might be associated with both features.

NUMERICAL SIMULATIONS IN MULTILAYERED MEDIA WITH IRREGULAR INTERFACES

We attempted to understand why Lg is not observed through the western part of the range. To investigate the influence of crustal geometry on Lg propagation, we performed some numerical modelling in laterally heterogeneous models for the SH case. Since Lg consists of a superposition of post-critically reflected S waves, the SH case must present most of the effect of the large-scale lateral variations of Moho depth. The calculation method combines the discrete wavenumber Green's function representation with boundary-integral equation techniques (Campillo & Bouchon 1985; Bouchon, Campillo & Gaffet 1989). The wavefield produced by the interfaces is considered to be equivalent to the radiation of body forces distributed along the boundaries. The inversion of a propagator matrix was performed for each interface, so that the computation time and the memory required varies only linearly with the number of interfaces. As many seismic experiments revealed the presence of a 10 km Moho jump between the North Pyrenean Zone and the axial zone (Hirn *et al.* 1980; Roure *et al.* 1989), we have first designed a model with simple change in crustal thickness (Fig 8a), the Moho being deeper on the Spanish side of the Pyrenees. There is no attenuation in this model: only the topography of the Moho is taken into account.

The synthetic seismograms, with a Ricker wavelet of 1.5 s period as the source function, are shown in Fig. 8(b). The maximum frequency reached is 1 Hz. The reduction velocity is 3.5 km s^{-1} , which is the *S*-wave velocity chosen for the crust. One can see the successive reflection branches, which constitute the reflected energy forming the *Lg* phase. The *Sn* head-wave branch appears for distances greater than 250 km with small amplitudes.

We can check that, at low frequencies, the Moho jump does not produce a notable effect on waveforms and amplitudes. One can notice a weak perturbation above the Moho jump, but amplitudes are as large beyond the jump as they are ahead of it. The use of boundary integral equations is limited to relatively low frequencies simply because of the high computation time required by this quasi-exact approach. In order to check the validity of our conclusions at higher frequency, we used the ray theory to compute an 'infinite frequency' response. The calculations were made with the same model of Moho topography. Details of the computations with the paraxial ray approach and of the comparison with the boundary-integration equation method results are given in Gibson & Campillo (1993). The synthetics obtained (Fig. 8c) are very similar to those of boundary integral equations and confirm that the Moho step will only have weak effect on the guided wave amplitude, whatever the frequency band is.

From these numerical tests we concluded that the Moho jump cannot be the reason for the vanishing *Lg* wave. This is strongly supported by the observation that *Lg* waves are not attenuated in the Eastern Pyrenees. We must, therefore, examine in more detail the influence of the particular structure of the western part of the chain.

Figure 9 (a) describes the second model, which includes results of recent deep seismic investigations conducted in the western Pyrenees (preliminary interpretation of the structure of the lithosphere along the Pyrenees-Arzacq Ecors profile, M. Daignières, private communication). These experiments suggest a zone of anomalously high velocity in the crust, in addition to the Moho jump. We, therefore, investigated the influence of such a structure.

The synthetic seismograms from this second model are shown in Fig. 9(b). One can notice that the *Sn* wave is stronger than in the previous model. Therefore, as observed on the real data, the *Sn/Lg* amplitude ratio is higher for the rays travelling through such a zone. But the *Lg* wave is not much affected: the amplitude of the *Lg* wave train is still large beyond the velocity anomaly area. Therefore, the geometry of this structure can not account for the almost complete extinction of the *Lg* phase observed on the data.

This energy blockage must then be explained by the local properties of the crustal material rather than by the large-scale geometry of the crust-mantle structure. The theoretical result is in a good agreement with the observation that *Lg* can propagate across the eastern part of the mountain range where the jump of the Moho between north and south is present as in the western part. The high velocities observed in this area where *Lg* disappears may be due to the presence of lower crustal blocks, brought up to the surface during the compression phases of the orogeny, or due to the presence of slices of mantle materials. Both interpretations would agree with existence of a positive Bouguer anomaly. As the lower crust is known to be layered and very reflective in many parts of western Europe (see Mooney & Brocher 1987, for a review), both interpretations imply an increased heterogeneity of the crust in this region with respect to neighbouring areas. An enhanced scattering of seismic waves by this heterogeneity may be the case of the strong attenuation of crustal phases observed in the zone where the gravity anomaly indicates intrusion of material of deep origin into the upper crust.

CONCLUSION

We combined observations and numerical simulations in order to study crustal wave propagation through the Pyrenees. We first computed a mean crustal value of the *S*-wave quality factor for central Spain to evaluate intrinsic attenuation along the paths. Q has been found in the form

$$Q = 330f^{0.51}$$

The seismogram analysis shows that in the central and eastern part of the mountain chain the North Pyrenean Fault does not block *Lg* propagation and that the Moho jump found in this region does not block either. In spite of the fact that the jump of the Moho is present all along the mountain range, a localized zone of attenuation exists in the western part of the Pyrenees, correlated with a positive Bouguer anomaly. As similar observations were made in the Alps in the Ivrea region and as numerical modellings show that geometrical effects do not explain the observed extinction of *Lg* waves, it seems that the general conclusion can be drawn that strong attenuation of guided waves is probably due to local crustal properties. Scattering by small-scale heterogeneities, such as lower crust or mantle slices, may be the cause of strong attenuation in the frequency range considered here. This interpretation is coherent with the observation of high seismic velocity and the position of a Bouguer anomaly in these regions.

ACKNOWLEDGEMENTS

We thank J. L. Plantet and Y. Cansi (LDG-CEA) and the technical staffs of the LDG and IGN networks for their help in making available the records needed for this study. G. Müller and two anonymous reviewers made valuable suggestions to improve this work. This work was partially supported by the project 'A.A. Tomographie' of INSU/CNRS (France) and by DARPA (USA) under contract 80-0082.

REFERENCES

- Bath, M., 1954 The elastic waves *Rg* and *Lg* along Eurasian paths, *Arkiv Geofysic*, 2, 295-342.
- Baumgardt., D. R., 1991, High frequency array studies of long range *Lg* propagation and the causes of *Lg* blockage and attenuation in the Eurasian continental craton. *Final Report PL-TR-91-2059 (II)*, Philipps Laboratory ADA236984
- Boilot, G., P.A. Dupleuble, M. Lamboy, L. D'Ozouville & J.C. Sibuet, 1971. Une hypothèse d'évolution tectonique du golfe Gascogne, in *Histoire structurale du Golfe Gascogne*, pp. V.6-1 - V.6-52, eds: Debysier, X. Lepichon and L. Montadert. Technip Paris
- Bouchon, M., A, 1981. A simple method to calculate Green' s function for elastic layered media, *Bull seism. Soc. Am.*, 71 , 959-971
- Bouchon, M., Campillo, M. & Gaffet, S., 1989, A boundary integral equation- discrete wavenumber representation method to study wave propagation in multiyered media having irregular interfaces. *Geophysics* 54. 1134-1140.
- Campillo, M., 1990. Propagation and attenuation characteristics of the crustal phase *Lg*. *Pure appl. geophys.*, 132, 1-19.
- Campillo, M. and Bouchon, M. & Massinon, B., 1984. Theoretical study of the excitation, spectral characteristics and geometrical attenuation of regional seismic phases. *Bull. Seism. Soc. Am.* 74, 79-90.
- Campillo, M., Plantet, J. L. & Bouchon, M., 1985. Frequency dependent attenuation in the crust beneath Central france from *Lg* waves, data analysis and numerical modeling. *Bull Seism. Soc. Am.* 75. 1395-1411.
- Campillo, M., Feignier, B., Bouchon, M. & Bethoux, N., 1993. Attenuation of crustal waves across the Alpine range, *J. Geophys. Res.*, 98, 1987-1996.
- Campillo, M. & Bouchon, M., 1985. Synthetic SH seismograms in a laterally varying medium b the discrete wavenumber method. *geophys. J. R. astr. Soc.*, 83, 307-317.

- Choukroune, P. & ECORS Team, 1989. The ECORS Pyrenean deep seismic profile: reflection data on the overall structure of an orogenic belt. *Tectonics*, **8**, 23-39.
- Gibson, R. & Campillo, M., 1993. Numerical simulation of high and low-frequency *Lg*-wave propagation. *Geophys. J. Int.*, submitted
- Hirn, A., Daigneres, M., Gallart, J. & Vadell, M., 1980. Explosion seismic sounding of throws and dips in the continental Moho. *Geophys. Res. Lett.*, **7**, 263-266.
- Instituto Geografico Nacional, 1991. Spanish National Seismic network, in *Seismicity, Seismotectonics and Seismic Risk of the Ibero-Maghrebian Region*, pp. 3-16, eds Mezcua, J & Udias, A., Monografia No. 8 IGN, Madrid.
- Kanamori, H., 1977. The energy release in great earthquakes, *J. geophys. Res.*, **82**, 2981-2987.
- Kennett, B. L. N., 1983. *Seismic wave propagation in stratified media*, Cambridge University Press, Cambridge.
- Kennett, B. L. N., Gregersen, S., Mykkelveit, S. & Newmark, R., 1985. Mapping of crustal heterogeneity in the North sea Basin via the propagation of *Lg* waves, *Geophys. J. R. astr. Soc.*, **83**, 299-306.
- Mooney, W. D. & Brocher, T. M., 1987. Coincident seismic reflection/refraction studies of the continental lithosphere: a global review, *Rev. Geophys.*, **25**, 723-742.
- Nicolas, M., Massinon, B., Mechler, P. & Bouchon, M., 1982. Attenuation of regional phases in Western Europe, *Bull. seism. Soc. Am.*, **42**, 219-228.
- Pinet, B., Montadert, L., Cumelle, R., *et al.*, 1987. Crustal thinning on the Aquitaine Shelf, Bay of Biscay, from deep seismic data, *Nature*, **325**, 513-516.
- Press, F. & Ewing, M., 1952. Two slow surface waves across North America, *Bull seism. Soc. Am.*, **42**, 219-228.
- Roure, F. Choukroune, P., Berastegui, X., Munoz, J. A., Villien, A., Matheron, P., Bareyt, M., Camara, P. & Deramond, J., 1989. ECORS deep seismic data and balanced cross-sections: geometric constraints on the evolution of the Pyrenees, *Tectonics*, **8**, 41-50.
- Ruzaikin, A. I., Nersesov, I. L., Khalturin, V. I. & Molnar, P., 1997. Propagation of *Lg* and lateral variations in crustal structure in Asia, *J. geophys. Res.*, **82**, 307-316.

TABLE 1

Event	Date	Latitude °N	Longitude °W	H Km	MI LDG	MI IGN	Mw-Lg
Ayamonte	20 12 89	23.286	- 07.328	23.	5.4	5.0	44.48
Grandola	23 09 89	38.291	- 08.655	18.	4.0		38.40
Cadix	25 10 87	36.361	- 06.501	66.	4.8	4.2	36.40
Alicante	02 12 88	38.200	+ 00.315	20.	3.8	3.8	33.37
Sotos	07 11 87	43.000	- 03.812	15.	3.9	3.8	35.37
Vilanova	10 08 86	41.128	- 07.213	12.	4.0	4.3	36.39
Laza	30 08 89	42.105	- 07.516	13.	3.7	3.9	35.37
Nazare	31 03 89	39.601	- 09.493	25 ?	3.7	3.5	33.35
Camero	20 09 87	42.138	- 02.476	05.	3.5	3.6	34.35
Aldea	24 05 88	38.400	- 03.406	12.	3.8		34.37
Cucalon	06 07 87	40.951	- 01.001	05.	3.5	3.3	31.33
Armedo	29 11 88	42.146	- 02.112	05.	3.1	3.2	29.31

TABLE 2
Crustal model used for the numerical calculations

Layer s Thickness (km)	P. Wave (km/sec)	S.Wave Velocity (km/sec)	Density (g/cm ³)	P.Wave Q	S.wave Q
2	3.3	2.5	2.1	10000	10000
5	6.1	3.48	2.8	10000	10000
4	5.6	3.18	2.7	10000	10000
13	6.4	3.58	2.9	10000	10000
7	6.85	3.90	3.0	10000	10000
	8.05	4.45	3.3	10000	10000

TABLE 3

Date	Time	Latitude °N	Longitude °W	MI LDG
07 04 86	23h32'07	42.91	- 1.90	3.1
27 10 86	06h48'12	39.88	- 1.12	3.5
24 08 87	18h43'06	41.01	1.49	4.4
20 02 88	16h38'48	42.40	1.48	3.8
16 03 88	21h19'02	42.38	2.17	3.8
26 07 90	16h29'32	42.37	- 1.29	3.7
20 08 90	12h22'33	40.26	- 0.92	3.4

Figure Captions

Figure 1: Locations of earthquake epicenters (stars) and IGN network stations (circles). On the map are also reported the paths used in the calculation of the mean value of crustal quality factor in Spain.

Figure 2: Source displacement spectra plotted for each earthquake in m.s.

Figure 3: Tectonic map of the Pyrenean region. The station EPF is reported on the Figure. NPF: North Pyrenean fault.

Figure 4: Cross section showing the crust geometry and the Moho topography from the Ebro basin in the South to the Aquitaine basin in the North in the central part of the mountain range (from Roure et al., 1989).

Figure 5: Short period records obtained for earthquakes "Camero" and "Cucalon" at station EPF (a and b) and in central France (c and d). The corresponding paths are plotted in Figure 6. The group velocity are indicated in order to make easier the identification of the different phases.

Figure 6: Map showing the location of earthquakes in Spain (black dots) and the seismic stations in France (circles) used to study regional phases crossing the Pyrenees. The lines correspond to the path of the seismograms shown in Figure 5. The heavy line indicates the axis used to locate the crossing of the chain for the different pairs. The grey zones indicate a positive Bouguer gravity anomaly.

Figure 7: Seismograms obtained in France for earthquakes in Spain plotted as function of group velocity to allow a direct comparison of the traces. The horizontal axis represents the position of the crossing of each path with the line Bilbao-Perpignan shown in Figure 6. Amplitudes are corrected from propagation effects and normalized to equal seismic moment using the propagation parameters obtained in central Spain and central France.

Figure 8: Influence of the Moho topography on L_g propagation. a) model used with a simple variation of the Moho depth. b) synthetic seismograms obtained using the boundary integral equation method. c) synthetic seismograms obtained using the asymptotic ray theory. All synthetics are plotted using a reduction velocity of 3.5 km/s.

Figure 9: Influence of the Moho topography on L_g propagation. a) model used with a Moho jump and introduction of high velocity bodies in the crust. b) synthetic seismograms obtained using the boundary integral equation method. Synthetics are plotted using a reduction velocity of 3.5 km/s.

FIGURE 1

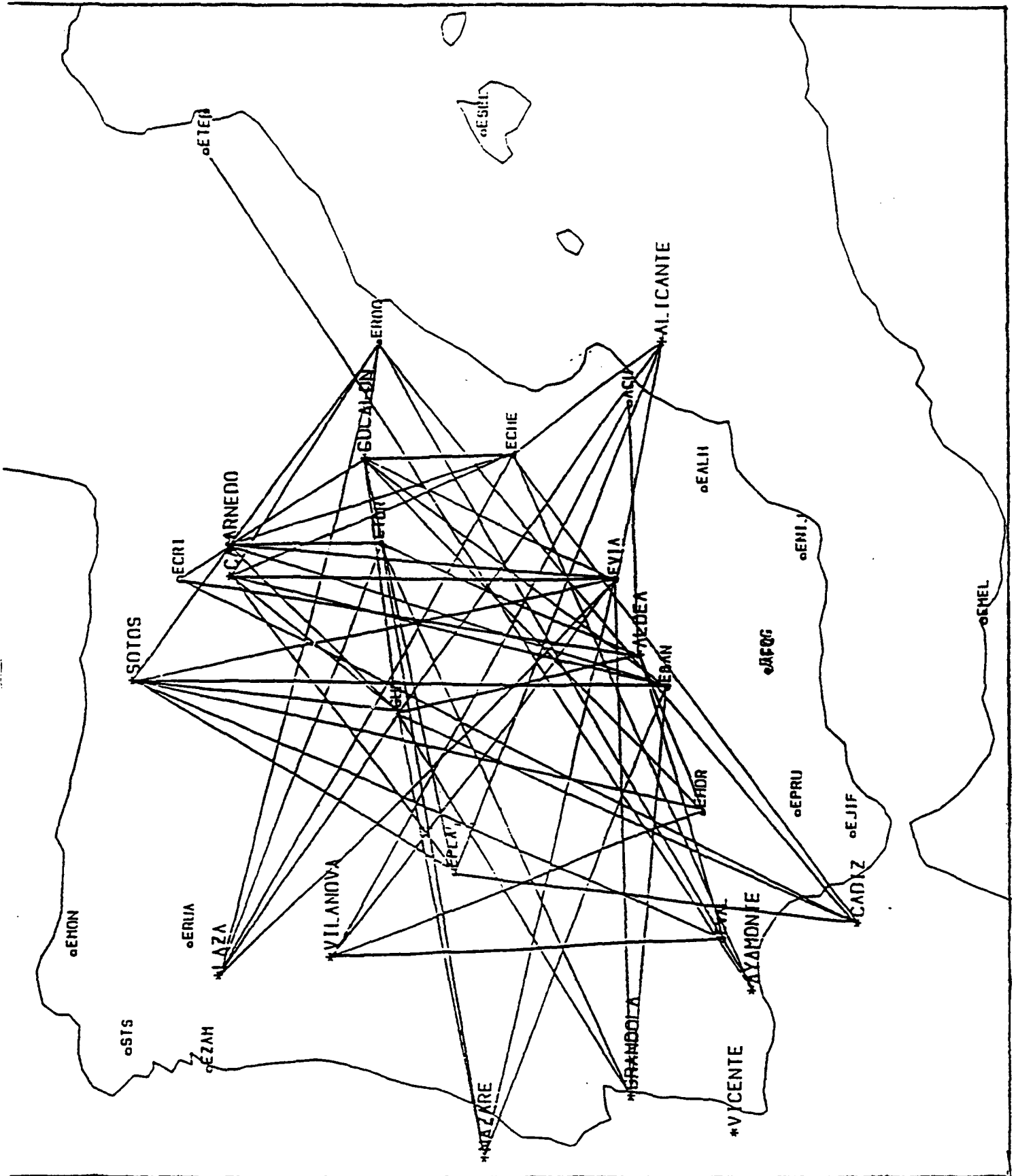
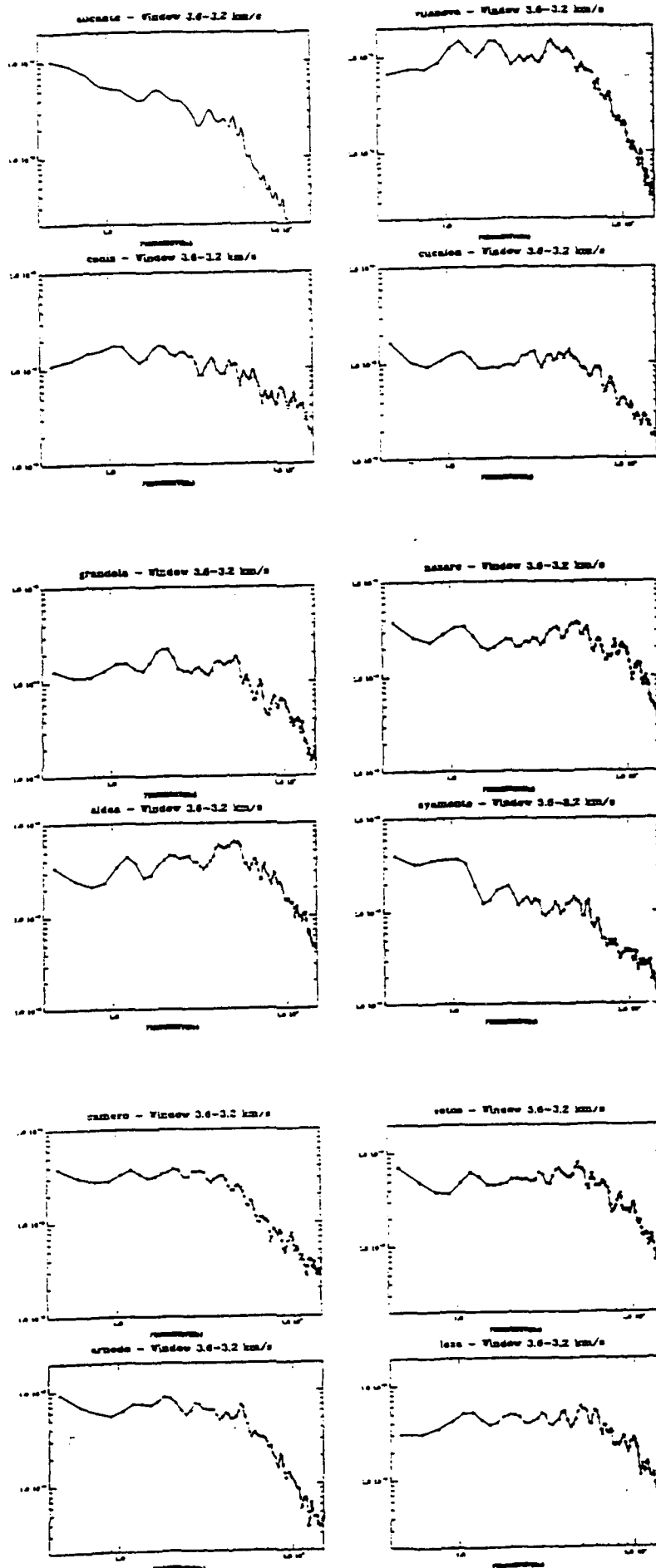


FIGURE 2



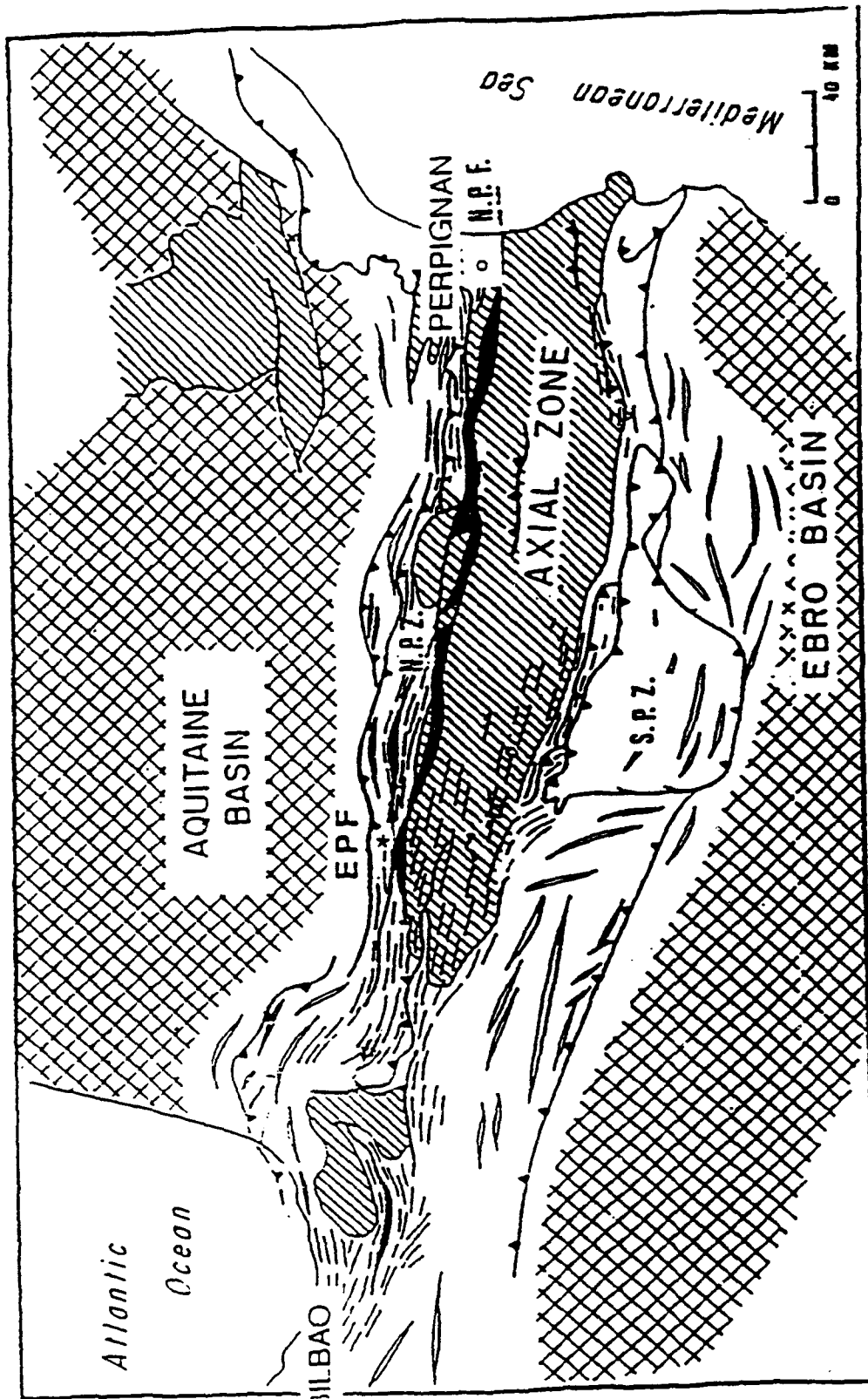


FIGURE 3

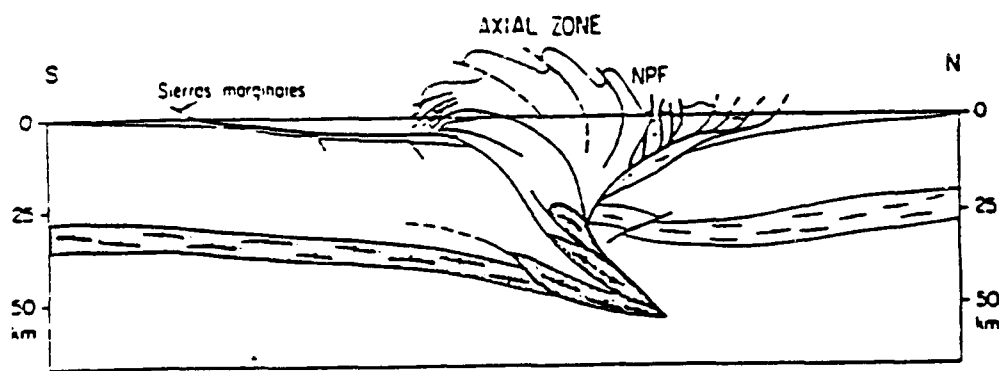
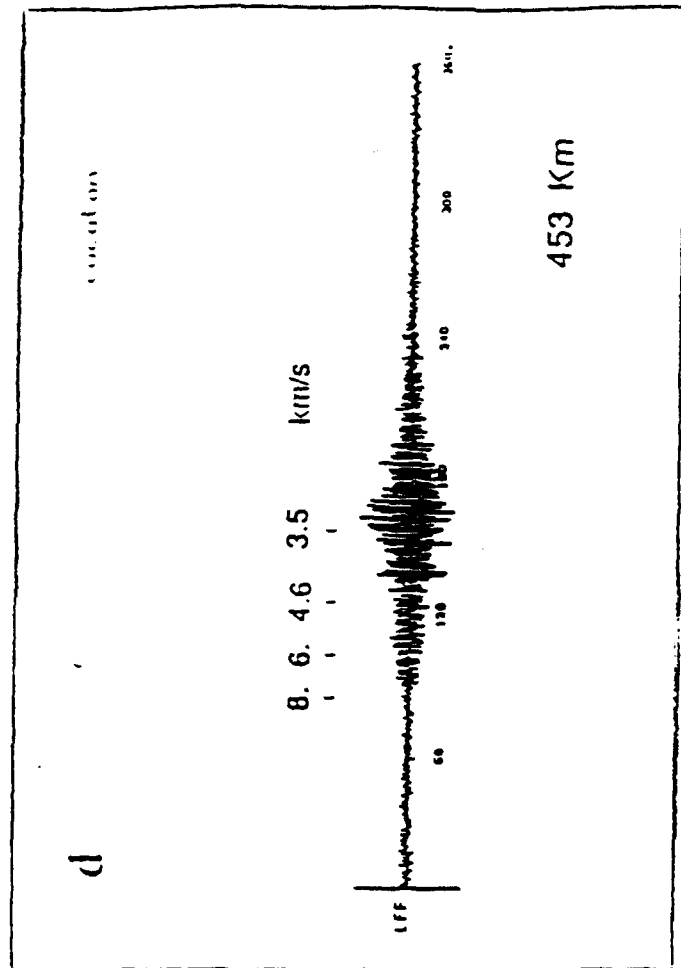
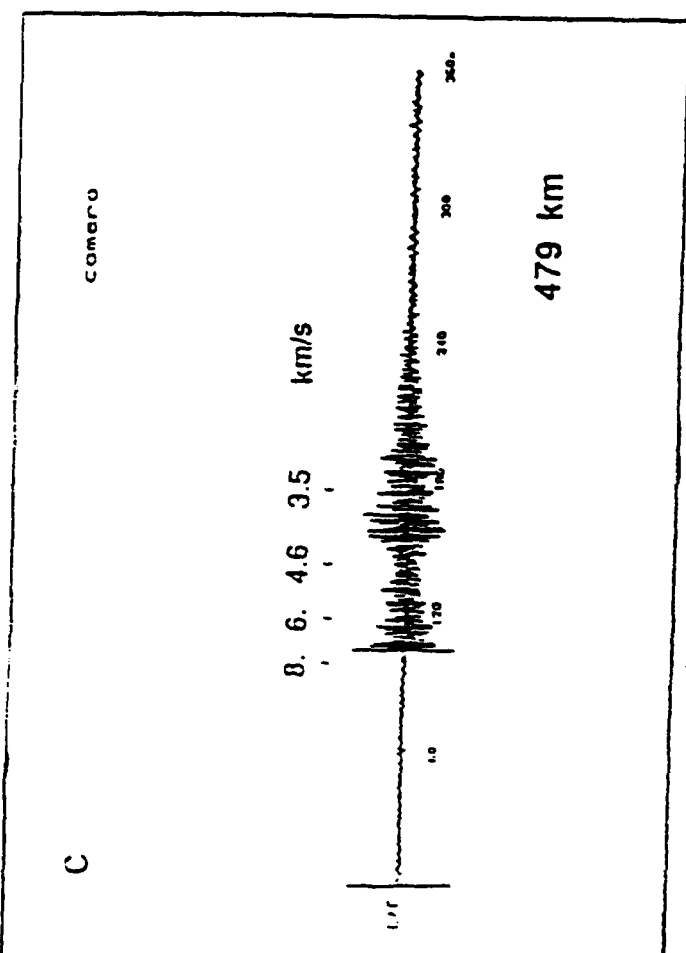
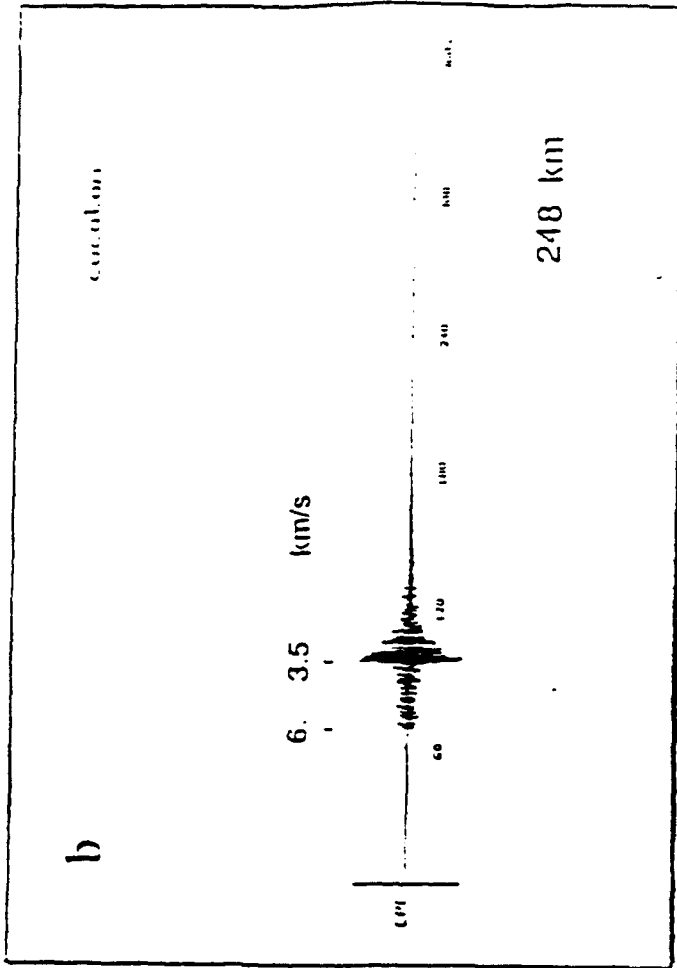
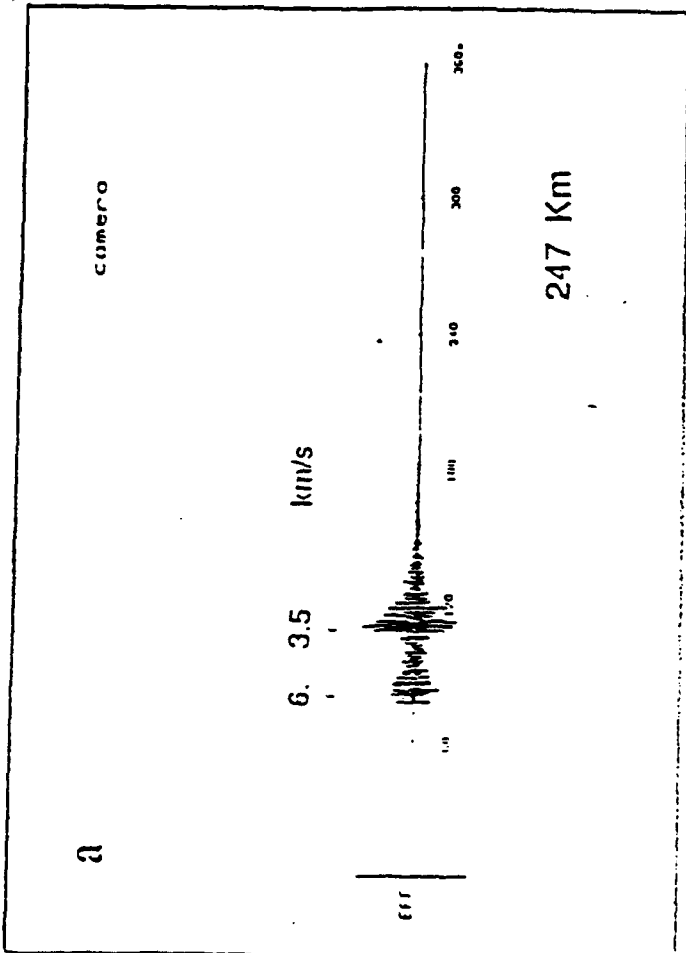


FIGURE 4

FIGURE 5



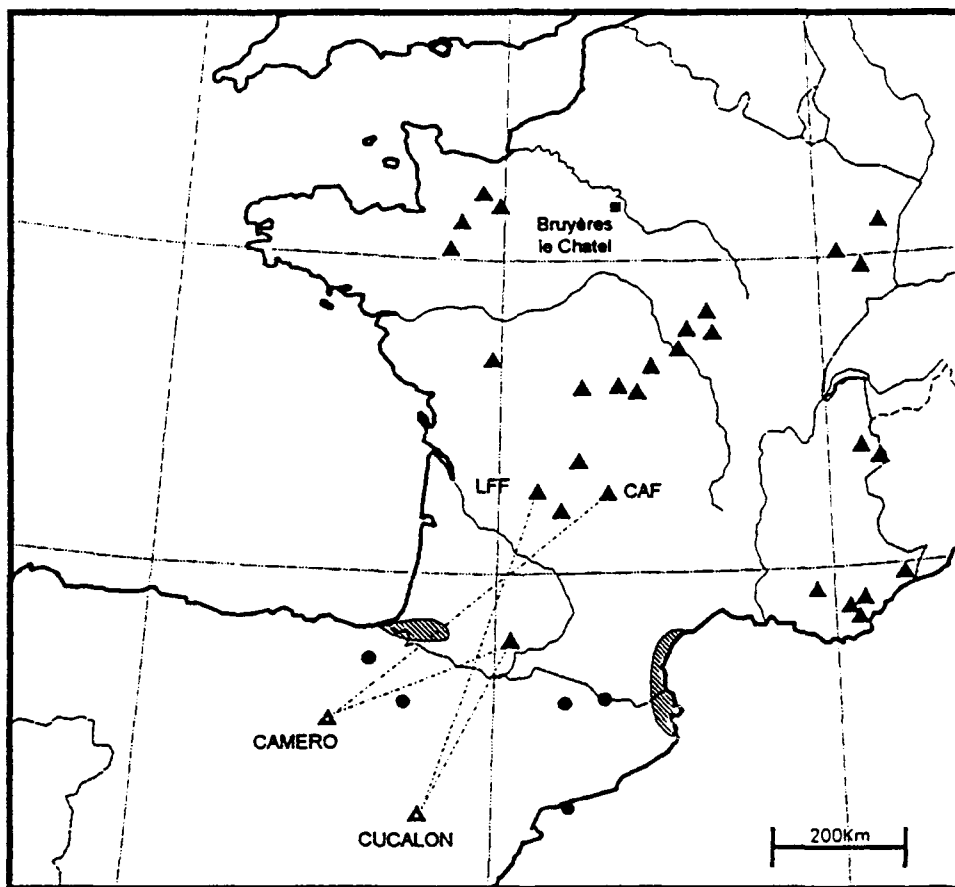
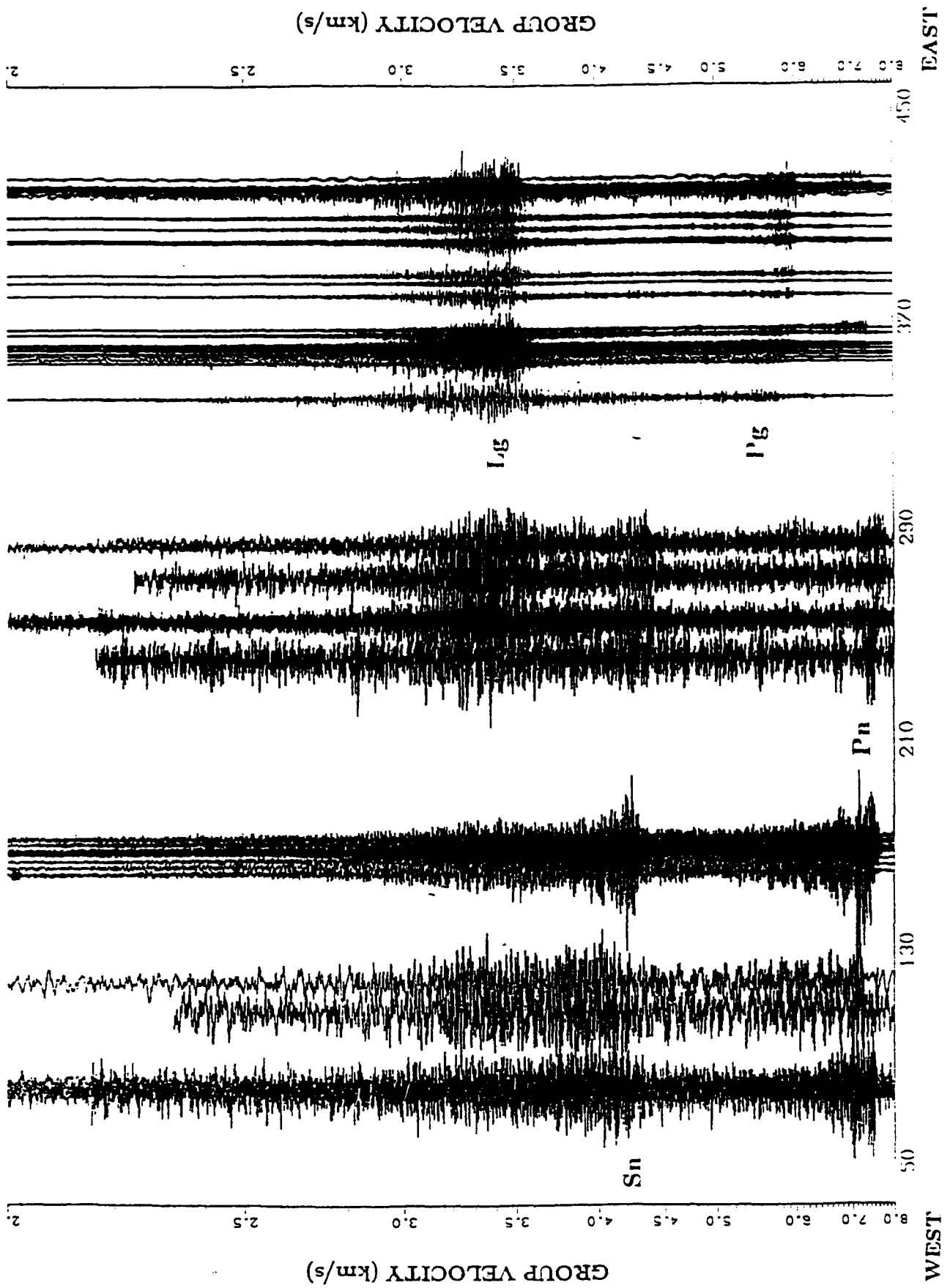


FIGURE 6



POSITION OF CROSSING OF THE PYRENEES MOUNTAIN RANGE (km)
 EAST
 WEST
 FIGURE 7

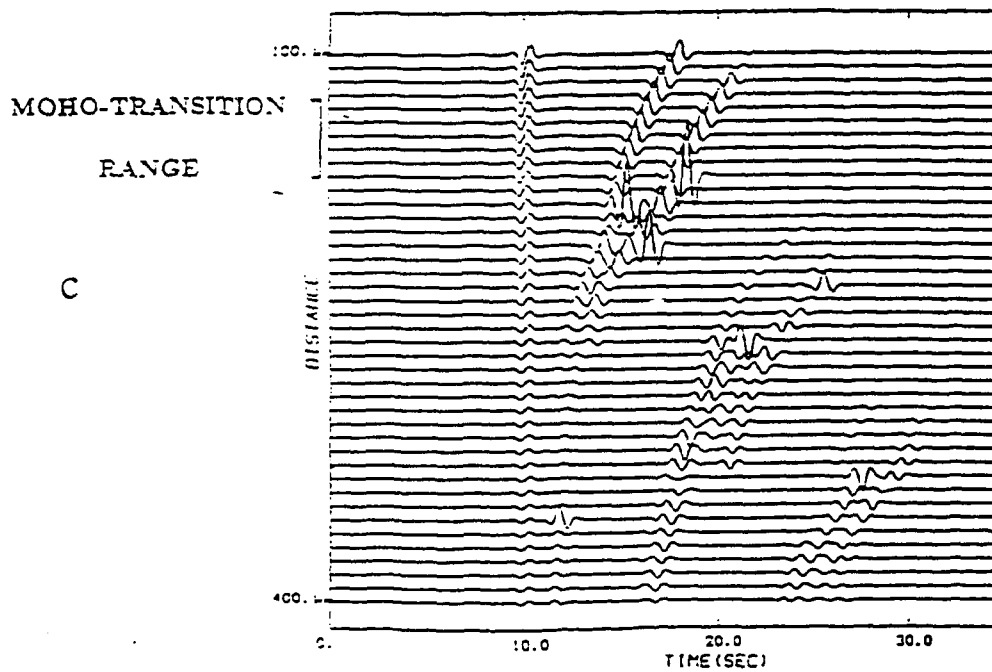
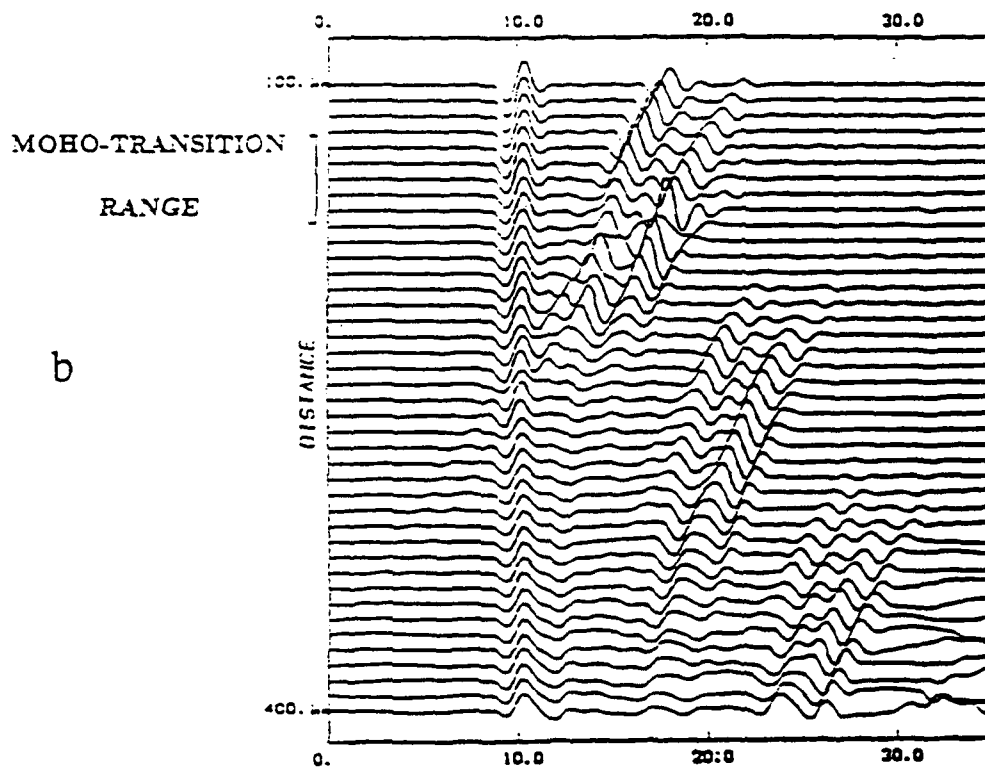
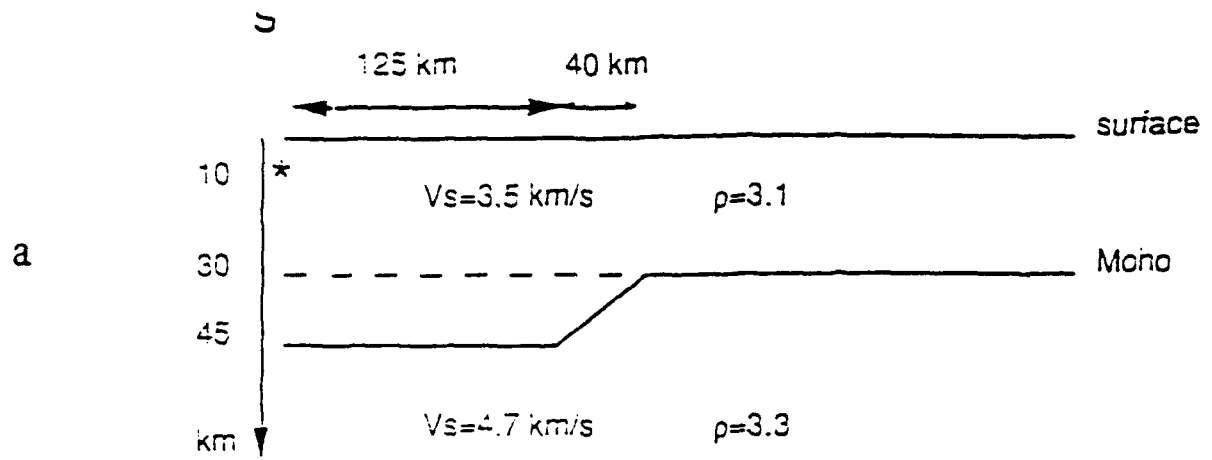


FIGURE 8

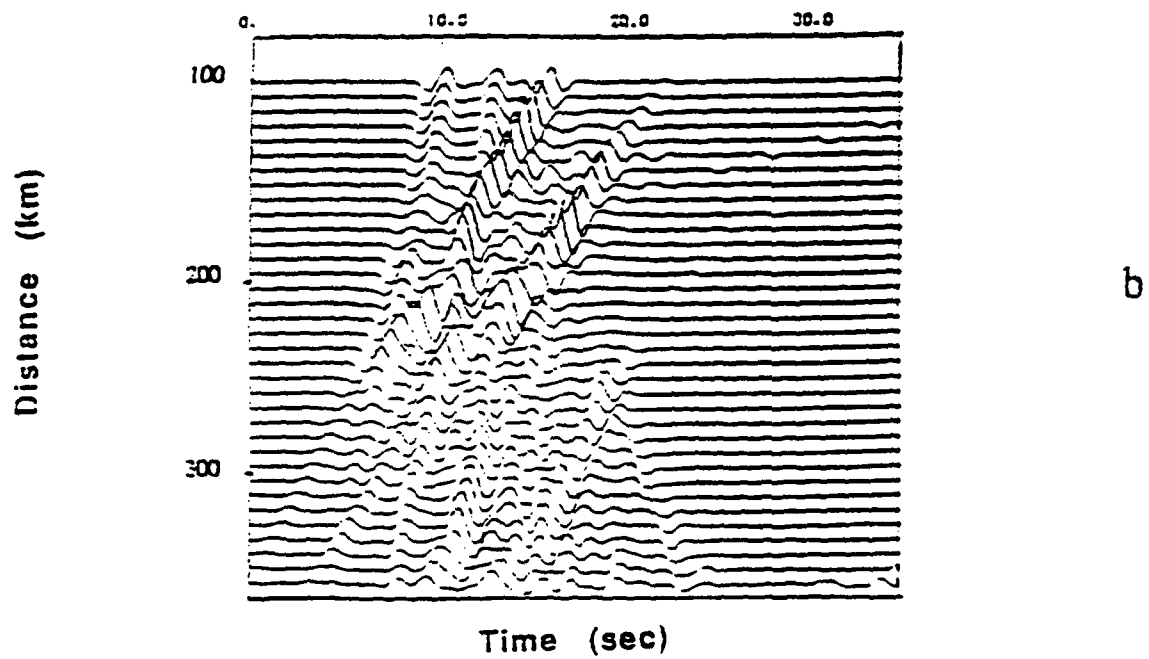
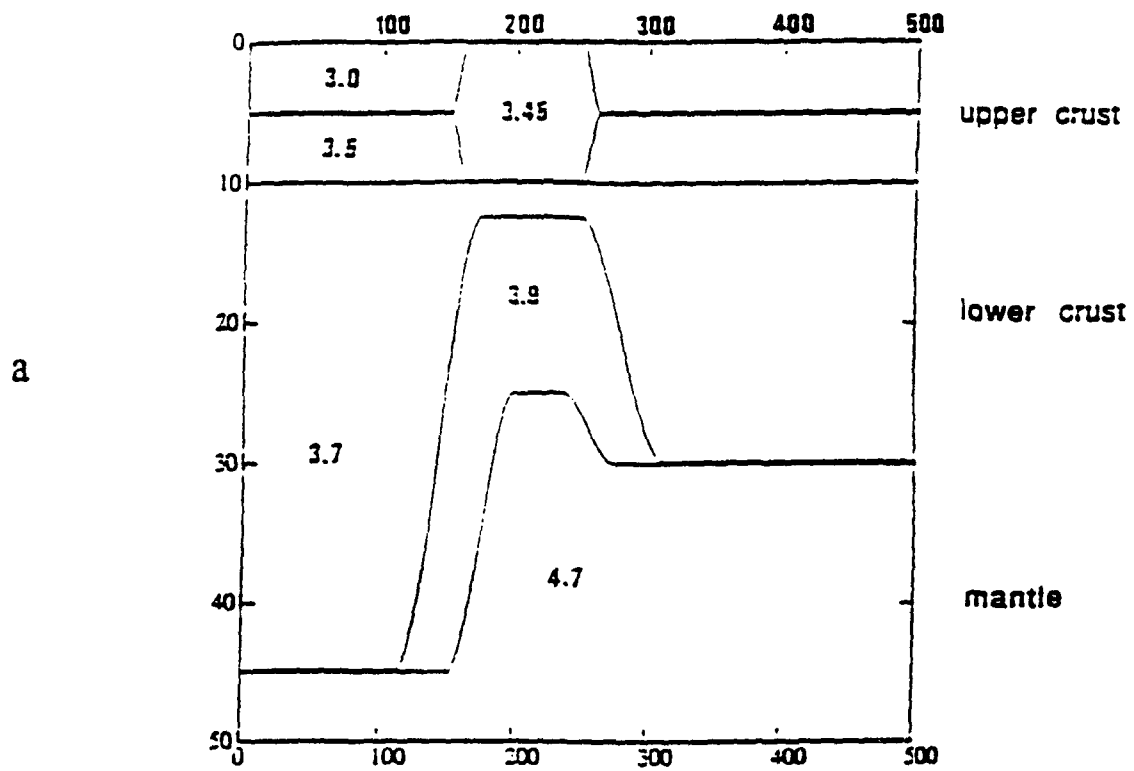


FIGURE 9

**Calculation of synthetic seismograms in a laterally-varying medium
by the boundary element - discrete wavenumber method**

by

Michel Bouchon and Olivier Coutant

Laboratoire de Géophysique Interne et Tectonophysique

Université Joseph Fourier

BP 53X. 33041 Grenoble, France

Abstract

We investigate the propagation of Lg waves in laterally-varying crustal structures by numerical simulation. The method of calculation is formulated in terms of boundary integral equations where the Green's functions are evaluated by wavenumber summation. The approach is well suited to study the propagation of seismic waves in a layered medium where the interfaces are flat in some regions and irregular in other regions. We investigate the effect of a crustal fault with vertical offset and study the case of a lateral change in crustal thickness. The results show that the Lg wave amplitude is only slightly affected by the presence of these heterogeneities. They confirm the robustness of Lg wave propagation in presence of lateral heterogeneities observed in other numerical simulations. They show that large scale geometric features of the crust cannot account alone for the strong attenuation of Lg waves observed in many regions. The results also suggest a possible relation between the level of Lg wave coda and the degree of roughness of the Moho. They further indicate the importance of back scattering and suggest a possible use of the back scattered wave field to map strong crustal heterogeneities.

Introduction

Over the last two decades, numerical simulation techniques have become an increasingly important tool in studying the propagation of seismic waves in complex geological structures. Several methods of elastodynamic calculations have been developed to this effect. The most widely used techniques may be classed in three groups: ray methods, finite-difference finite-element techniques, and boundary integral equation methods.

These numerical simulation studies have been performed for different types of geological structures. Among the most extensively studied geological objects are sedimentary basins and alluvial valleys (Aki and Larner, 1970; Trifunac, 1971; Bouchon and Aki, 1977a; Hong and Helmberger, 1978; Sanchez-Sesma and Esquivel, 1979; Bard and Bouchon, 1980a,b, 1985; Harmsen and Harding, 1981; Dravinski, 1983; Lee and Langston, 1983; Sanchez-Sesma, 1983; Nowack and Aki, 1984; Bard and Gariel 1986; Géli et al., 1987; Koketsu, 1987; McLaughlin et al., 1987; Moczo et al., 1987; Mossessian and Dravinski. 1987, 1992; Benz and Smith, 1988; Bravo et al. 1988; Campillo et al., 1988; Kawase, 1988; Sanchez-Sesma et al., 1988; Vidale and Helmberger, 1988; Kawase and Aki. 1989; Rial, 1989; Seligman et al., 1989; Hill et al., 1990; Horike et al., 1990; Novaro et al., 1990; Gaffet and Bouchon, 1991; Gariel et al., 1991; Koketsu et al.. 1991; Liu et al., 1991; Papageorgiou and Kim, 1991; Frankel and Vidale, 1992; Graves and Clayton, 1992; Kagawa et al., 1992; Kawase and Sato, 1992; Ohori et al., 1992; Toshinawa and Ohmachi, 1992; Uebayashi et al., 1992; Frankel, 1993; Jongmans and Campillo, 1993; Mateos et al., 1993; Zahradnik et al., 1993). Other types of complex geological structures investigated include irregular subsurface layering (Smith. 1975; Kelly et al., 1976; Cervený et al., 1977;

Psencik, 1979; Drake, 1980; Nicoletis, 1981; Chapman and Drummond, 1982; Cerveny and Psencik, 1983, 1984; Hill and Levander, 1984; Mikhailenko, 1984, 1985; Virieux, 1984, 1986; Levander and Hill, 1985; Reshef and Kosloff, 1985; Dablain, 1986; Beydoun and Kebo, 1987; Campillo 1987a; George et al., 1987; Hu et al., 1988; Paul and Campillo, 1988; Reshef et al., 1988; Bouchon et al., 1989; Chavez-Garcia and Bard, 1989; Daudt et al., 1989; Yamanaka et al., 1989; Carcione, 1993; Gibson et al., 1993; Schultz and Toksöz, 1993), laterally-varying crustal structure (Aki and Larner, 1970; Boore, 1970, 1972; McMechan and Mooney, 1980; Cerveny et al., 1984; Müller, 1984; Stephen, 1984; Helmberger et al., 1985a,b; Vidale et al., 1985; Campillo, 1987b; Emmerich, 1989, 1992; Ho-Liu and Helmberger, 1989; Maupin, 1989; Regan and Harkrider, 1989a,b; Vaccari et al., 1989; Regan, 1991; Campillo et al., 1993 ; Gregersen and Vaccari, 1993), and fault zones (Cormier and Spudich, 1984; Cormier and Beroza, 1987; Ben-Zion and Aki, 1990; Kang and McMechan, 1993; Moczo and Bard, 1993).

In the present paper we apply the boundary integral equation method to investigate the propagation of seismic waves over distances of a few hundred kilometers in laterally heterogeneous crustal structures. We use a formulation very close to the one developed by Kawase (1988) and Kawase and Aki (1989, 1990) where the Green's functions are calculated by the discrete wavenumber method and where the singularities inherent to the boundary integral equation approach are removed by integrating analytically the Green's function expressions over surface elements.

Description of the method

The simplest medium configuration involves two homogeneous media separated

by an interface and is depicted in Figure 1a. A source of elastic disturbance is located in one of the medium (denoted thereafter by index 1) and produces at a point P of medium 1 a direct wavefield $V_o(P)$. For simplicity we shall only consider the two-dimensional antiplane problem. Using Huygens principle, the wavefield diffracted by the interface can be described as the radiation from secondary sources distributed all along the interface. The total wavefield at P may thus be written in the form:

$$V(P) = V_o(P) + \int_S \sigma(Q) G(P, Q) dQ \quad (1)$$

where $\sigma(Q)$ is a source density function which represents the strength of the diffracting source at the interface point Q and $G(P, Q)$ is the wavefield radiated at P by a unit source located at Q and is called the Green's function of medium 1. The integration is taken over the surface of separation S .

Similarly, the wavefield diffracted in the second medium may be written in the form:

$$V(P') = \int_S \sigma'(Q) G'(P', Q) dQ \quad (2)$$

where G' is the Green's function of medium 2.

The first step towards the obtention of a numerical solution for the diffracted wavefield requires a discretization of the surface integral. This is achieved by approximating the surface S by N surface elements ΔS_i on which the source density functions σ and σ' are assumed to be constant (Figure 1b). Equations (1) and (2) thus become:

$$V(P) = V_o(P) + \sum_{i=1}^N \sigma_i \int_{\Delta S_i} G(P, Q) dQ \quad (3)$$

$$V(P') = \sum_{i=1}^N \sigma_i \int_{\Delta S_i} G'(P', Q) dQ$$

Then choosing P and P' to lie on the interface itself and denoting by Q_j this particular point (chosen for instance at the middle of the j th surface element, Figure 1c), one gets:

$$V(Q_j) = V_o(Q_j) + \sum_{i=1}^N \sigma_i \int_{\Delta S_i} G(Q_j, Q) dQ \quad (4)$$

(4)

$$V(Q_j) = \sum_{i=1}^N \sigma'_i \int_{\Delta S_i} G'(Q_j, Q) dQ$$

The continuity of the displacement wavefield across the interface requires the equality of the two right hand sides of equations (4) and provides a system of N equations (as $j=1, N$) where the unknowns are the σ_i and the σ'_i . The continuity of the stresses across S provides N more equations and thus leads to a system of $2N$ equations to $2N$ unknowns.

Before inverting the system one need to evaluate the expressions:

$$\bar{G}_{i,j} = \int_{\Delta S_i} G(Q_j, Q) dQ \quad (5)$$

and

$$\bar{G}'_{i,j} = \int_{\Delta S_i} G'(Q_j, Q) dQ$$

for $i=1, N : j=1, N$

and

$$T_{i,j} = \int_{\Delta S_i} T(Q_j, Q) dQ \quad (6)$$

$$T'_{i,j} = \int_{\Delta S_i} T'(Q_j, Q) dQ$$

where $T(Q_j, Q)$ is the surface traction produced at Q_j by a unit line force acting at Q , and T' is the same quantity calculated for the elastic parameters of medium 2.

Using the discrete wavenumber method (Bouchon and Aki, 1977b), the two-dimensional antiplane Green's function expressed in the frequency domain may be written in the form:

$$G(Q_j, Q) = \frac{1}{2i\rho\beta^2 L} \sum_{n=-M}^M \frac{e^{-i\gamma_n(z_j-z_Q)} e^{-ik_n(x_j-x_Q)}}{\gamma_n} \quad (7)$$

with:

$$k_n = \frac{2\pi n}{L},$$

$$\gamma_n = \left(\frac{\omega^2}{\beta^2} - k_n^2\right)^{1/2}, \quad \text{Im}(\gamma_n) \leq 0.$$

where (x_j, z_j) are the coordinates of Q_j and (x_Q, z_Q) those of Q , ρ is the medium density, β is the shear wave velocity, L is the periodicity length associated with the method, and M is an integer large enough to insure convergence of the series.

The traction T is thus given by:

$$T(Q_j, Q) = \rho\beta^2 \left[n_{x,j} \frac{dG(Q_j, Q)}{dx_j} + n_{z,j} \frac{dG(Q_j, Q)}{dz_j} \right] \quad (8)$$

where $n_{x,j}$ and $n_{z,j}$ denote the x and z components of the normal to the interface at Q_j . If we approximate each surface element ΔS_i by a plane surface, the analytical

integration of G and T (equations (5) and (6)) in their discrete wavenumber form is straightforward as long as $i \neq j$. When $i=j$ equation (8) breaks down for $Q=Q_j$, and equation (6) must be replaced by (see appendix):

$$T_{i,i} = T'_{i,i} = \frac{1}{2} \quad (9)$$

The inversion of the linear system expressing the continuity of displacement and stress across the interface then leads to the two source density distributions σ_i and σ'_i representing the diffracted wavefield in the two media.

The use of the discrete wavenumber method of calculating Green's functions in the boundary element scheme has the advantage of preventing the occurrence of mathematical or numerical singularities often associated with boundary element or boundary integral equation techniques. It is also easy to implement when one of the medium or the two media are made up of flat layers. In such a case, the full-space Green's functions are simply replaced by the layered medium Green's functions through the use of a Thomson-Haskell or Kennett algorithm (Kennett, 1974; Müller, 1985) and the surface integrals (5) and (6) are still evaluated analytically. We shall now present such examples of calculation.

Test of accuracy of the method

In order to check the precision of the method we consider the configuration depicted in Figure 2a. The medium consists of a homogeneous crustal layer, 30 km thick, overlaying a mantle half-space. The source is a line of horizontal shear dislocation occurring on a vertical plane and located at 10 km depth. The receivers are placed along a linear profile which extends in a direction perpendicular to the

line of dislocation. The time dependence of the dislocation is a smooth step-function defined by:

$$f(t)=[1+atan(t/t_0)]/2 \quad \text{with a rise time } t_0 \text{ equal to } 0.5\text{s} \quad (10)$$

Two calculations are made: For the first one we consider the problem as one involving a source embedded in a flat layered medium and use the discrete wavenumber method coupled with reflectivity matrices. For the second calculation we consider that we have two independent layered media separated by a fictitious vertical interface located at 200 km from the source. We thus treat the problem as if the crustal-mantle structure on both sides of the 200 km mark were different. We divide the fictitious vertical boundary into 100 surface elements. We calculate the mathematical expressions of the Green's functions G and G' for the crust-mantle structure using the discrete wavenumber method. We integrate analytically over each surface element (equations (5) and (6)) the resulting expressions. We invert the resulting linear system of equations and obtain the two source distributions σ and σ' . We finally use the two source distributions inferred to calculate the seismic displacement produced at the receivers. In carrying out this procedure we assume that the fictitious surface of separation between the two media extends from the free surface down to a finite depth (chosen as 45 km) below which little seismic energy is present.

The comparison between the two sets of results is displayed in Figure 2b. The calculation is made over a time window of 60s and for frequencies up to 2Hz. The periodicity length L used in the discrete wavenumber method for the two calculations is 850 km. The agreement between the two solutions proves the validity of the approach. The choice of the number of elements to represent the

diffracting surface (100) is somewhat arbitrary. In general, the number of elements depends on the particular frequency considered: At low frequencies a minimum number of elements is required, while at high frequencies this number should be chosen such that at least three surface elements are sampled per seismic wavelength. For this reason the element size may vary from one layer to the next according to the layer shear wave seismic wavelength.

Effect of a vertical fault

We now investigate how the propagation of Lg waves is affected by the presence of a fault. Below periods of a few seconds and up to very high frequencies the Lg wave train is the most prominent seismic phase produced by crustal earthquakes at regional distances (100km to 1000km from the source). These waves are made up of shear waves multiply-reflected in the crust and incident on the Moho at angles more grazing than the critical angle defined as the incident angle beyond which all the downgoing shear energy is reflected back into the crust. The prominence of the Lg waves arises from the waveguide nature of their propagation and it is interesting to investigate how irregularities of the waveguide affect their amplitude and characteristics.

The crustal model considered is shown in Figure 3a. A vertical fault with 2km offset extends from the surface to the Moho. The fault is represented by boundary elements and the Green's functions are calculated for the two flat-layer structures present on both sides of the fault. The criterion used to determine the number of elements is the one described in the previous section. The boundary extension is limited to 45km depth. The earthquake is modelled as a line of horizontal shear dislocation occurring on a vertical plane at a depth of 10km and is located 200km

from the fault. The time dependence of the dislocation is governed by equation (10) and the frequency range extends from 0 to 3Hz. The receivers are placed along a linear array perpendicular to the line of dislocation and to the fault. The corresponding seismograms are displayed in Figure 3b. The presence of a back scattered wavefield originating from the fault is clearly seen. Its amplitude is about 1/10th the amplitude of the primary field. At the crossing of the fault a change in the character of the seismograms occurs with the near-disappearance of the surface wave trains. Also a shift in the arrival time of the refracted mantle shear wave (S_n) takes place when crossing the fault.

A comparison between the seismogram obtained 300km away from the source with those that would be obtained in the absence of the fault is shown in Figure 4. The first comparison (CRUST1) corresponds to the case of a flat-layer crust similar to the one present on the left hand side of the fault. The second one (CRUST2) corresponds to the crustal model on the right hand side of the fault. These results show that the presence of the fault changes entirely the Lg waveform but does not affect significantly its energy. These observations can be accounted for by the nature of the Lg phase. Because its waveform is the result of the interference pattern between numerous shear wave arrivals, relatively small changes in crustal structure produce phase differences between the interfering waves and thus affect the waveform. On the other hand the amplitude of each individual shear wave constituting the Lg wave train is not significantly affected by a small variation in crustal structure so that the total energy of the Lg wave is almost unchanged.

Effect of a change in the Moho depth

We now investigate the effect on the seismograms of a lateral change in crustal

thickness. The structure considered is depicted in Figure 5a. It involves a change in the Moho depth which rises from 35km to 25km over an horizontal distance of 10km. The earthquake source and the receivers have the same characteristics and locations as in the previous example. The position of the diffracting boundary used in the calculation is represented by the dashed line. It extends from the free surface down to 47km depth and includes the dipping Moho. The verticality of the two boundary segments extending in the crust and in the mantle is chosen to minimize the number of boundary elements required.

The results are presented in Figure 5b. They show that the back scattered wave field is very strong which suggests that in real observations part of the Lg wave coda is due to back scattering induced by variations in crustal thickness and that the level of coda present might be related to the roughness of the Moho. This simulation also shows that the position where the change in crustal thickness takes place may be inferred by a well-placed seismic array.

The comparison of the seismogram obtained at 300km with those that would be obtained if the crust were laterally homogeneous is depicted in Figure 6. The two flat-layer models correspond to the structures on both sides of the region where the variation of crustal depth occurs. Like for the previous configuration, the high sensitivity of the Lg waveform to the crustal structure is apparent, while the amplitude stays stable. On the contrary the surface waves, which sample only the upper part of the crust, are in phase between the three models and display similar waveforms. The arrival time of the refracted mantle shear wave (S_n) lies between the arrival times predicted by the two flat-layer models.

In order to gain more physical insight into the diffraction phenomenon induced by the change in crustal thickness, we present in Figure 7 a space-time display of

the wavefield. The amplitude of the waves is calculated at a grid of points extending from the surface down to a depth of 45km and between epicentral distances of 150km and 250km. Fifteen snapshots taken at 3.5s interval and starting 39s after the occurrence of the earthquake are presented. The first ones show the propagation of the shear wave fronts which form the Lg wave. The back propagation of the scattered wavefield becomes apparent after about 63s. The last five snapshots show the presence of a nearly-cylindrical wavefront which seems to originate from the free surface area located above the dipping Moho. We interpret this feature as shear waves scattered upward by the Moho slope and subsequently reflected downward by the free surface. Because of the dominance of the primary wavefield at earlier times, only the downward propagation is visible.

Conclusion

We have investigated the propagation of Lg waves in a laterally-varying crust using a numerical simulation technique formulated in terms of boundary integral equations where the Green's functions are evaluated by discrete wavenumber summation. The method is well suited for studying the propagation of seismic waves in a layered crustal structure which varies laterally over part of the propagation path.

We have considered the case where a fault with vertical offset is present and the case of a change in crustal thickness. Our results confirm the simulation experiments of Maupin (1989), Regan and Harkrider (1989a), Campillo et al. (1993), and Gregersen and Vaccari (1993) which all clearly show that Lg wave propagation in crustal structures with strong lateral variations is surprisingly robust and that large scale geometric features of the crust are not sufficient to account for the

strong attenuation of Lg waves observed in many regions.

The present results also suggest a possible relation between the level of Lg wave coda and the degree of roughness of the Moho. They further indicate the importance of the back scattered wave field and suggest its possible use to map crustal heterogeneities.

Acknowledgements

This research was supported by the Advanced Research Projects Agency and was monitored by the Air Force Office of Scientific Research under grant 90-0356.

Appendix

The Somigliana representation theorem (see e.g. Aki and Richards, 1980) gives the expression of the displacement or stress fields as a function of their value on an interface S delimiting a volume V . In the SH case for the interior problem, the displacement is written as:

$$cu_y(\xi) = \int_S [G_{yy}(\mathbf{x}, \xi) \tau_{yj}(\mathbf{x}) - T_{yyj}(\mathbf{x}, \xi) u_y(\mathbf{x})] dS_j(\mathbf{x}) \quad (1a)$$

where G_{yy} and T_{yyj} are the displacement and stress Green's functions evaluated at \mathbf{x} for a source at ξ . The volumic body forces are assumed to be null and c is a constant which takes the value 0, 1 or 0.5 for \mathbf{x} respectively outside, inside V , and on S , assuming S has smooth boundaries. Different equivalent representations may be derived from (1a) to obtain a form equivalent to Huygens principle which involves a single surface distribution (see e.g. Coutant, 1989). In the SH case, the Kirchhoff-Helmholtz representation for instance uses a single layer force distribution (or unidirectional forces as opposed to a double layer dipole with moment distribution) whose amplitude is given by a stress discontinuity $[\tau]$. In this case the displacement is written:

$$u_y(\mathbf{x}) = \int_S G_{yy}(\mathbf{x}, \xi) [\tau]_{yj}(\xi) dS_j(\xi) \quad (2a)$$

By construction of this representation, the displacement field is continuous across S and its expression is valid for \mathbf{x} located on S or inside or outside V . The stress field representation however is discontinuous across S , $\tau_{out} - \tau_{in} = [\tau]$, and its value on S must be evaluated with a limiting process (see e.g. Sanchez-Sesma and Campillo, 1991). The stress field representation is:

$$\tau_{yj}(\mathbf{x}) = \zeta \frac{[\tau]_{yj}(\mathbf{x})}{2} + \int_S T_{yyj}(\mathbf{x}, \xi) [\tau]_{yj}(\xi) dS_k(\xi) \quad (3a)$$

where ζ is 1 when \mathbf{x} is on S , 0 otherwise. The discretization of integral representations (2a) and (3a) is achieved by approximating the surface S by N planar segments ΔS_i with normal \mathbf{n}_i and by assuming the force density per surface unit $\sigma = [\tau]_{yj} n_j$ to be constant on each segment. The representation then becomes:

$$u_y(\mathbf{x}) = \sum_{i=1}^N \sigma_i \int_{\Delta S_i} G_{yy}(\mathbf{x}, \xi) dS(\xi) \quad (4a)$$

and

$$\tau_{yj}(\mathbf{x}) = \zeta \frac{[\tau]_{yj}(\mathbf{x})}{2} + \sum_{i=1}^N \sigma_i \int_{\Delta S_i} T_{yy}(\mathbf{x}, \xi) dS(\xi) \quad (5a)$$

In order to solve the boundary conditions problem, we need to compute the stress and displacement on the boundary S at the N segment collocation points \mathbf{x}_i . The following auto-influence terms have to be evaluated:

$$u_y(\mathbf{x}_i) = \sigma_i \int_{\Delta S_i} G_{yy}(\mathbf{x}_i, \xi) dS(\xi) \quad (6a)$$

and

$$\tau_y(\mathbf{x}_i) = \frac{\sigma(\mathbf{x}_i)}{2} + \sigma_i \int_{\Delta S_i} T_{yy}(\mathbf{x}_i, \xi) dS(\xi) \quad (7a)$$

The two integrals contain respectively a weakly and a strongly singular kernel and can be integrated in the space domain (e.g. Sanchez-Sesma and Campillo, 1991) or using the discrete wavenumber (DW) decomposition of the Green's function. Performing the integral in the DW domain requires however a minor correction to

the expression of the stress field as a function of the horizontal wavenumber. The SH displacement Green's function for an infinite space may be expressed in its wavenumber representation form as:

$$G_{yy}(\mathbf{x}) = \frac{1}{4\pi i \rho \beta^2} \int_{-\infty}^{\infty} \frac{e^{-i\gamma|z-z_0|} e^{-ik(z-z_0)}}{\gamma} dk \quad (8a)$$

The stress tensor T_{yyj} horizontal wavenumber representation can be directly obtained from (8a) by derivation with one exception, when the source and "receiver" are located at the same vertical position, ie for $z=z_0$. In this case the component T_{yyz} is undefined and the stress can only be computed for a vertically oriented ($n_x=1, n_z=0$) segment. Since the integral is independent of the segment orientation, we evaluate (7a) by performing the calculation for a vertical orientation, that is:

$$\int_{\Delta S_i} T_{yy}(\mathbf{x}_i, \xi) dS(\xi) = \int_{\Delta S_i} T_{yyz}(\mathbf{x}_i, \xi) dS(\xi) = \frac{1}{4\pi i \rho \beta^2} \int_{\Delta S_i} \int_{-\infty}^{\infty} -ik \frac{e^{-i\gamma|z-z_0|}}{\gamma} dk dz = 0 \quad (9a)$$

This result is similar to the one obtained by integration in the space domain, and we finally get:

$$\tau_y(\mathbf{x}_i) = \frac{\sigma(\mathbf{x}_i)}{2} \quad (10a)$$

References

- Aki, K., and K.L. Larner (1970). Surface motion of a layered medium having an irregular interface due to incident plane SH waves, *J. Geophys. Res.* 75, 933-954.
- Aki, K., and P.G. Richards (1980). *Quantitative seismology*, W.H. Freeman and Co, San Francisco.
- Bard, P.Y., and M. Bouchon (1980a). The seismic response of sediment-filled valleys. Part 1. The case of incident SH waves, *Bull. Seism. Soc. Am.* 70, 1263-1286.
- Bard, P.Y., and M. Bouchon (1980b). The seismic response of sediment-filled valleys. Part 2. The case of incident P and SV waves, *Bull. Seism. Soc. Am.* 70, 1921-1941.
- Bard, P.Y., and M. Bouchon (1985). The two-dimensional resonance of sediment-filled valleys, *Bull. Seism. Soc. Am.* 75, 519-542.
- Bard, P.Y., and J.C. Gariel (1986). The seismic response of two-dimensional sedimentary deposits with large velocity gradients, *Bull. Seism. Soc. Am.* 76, 343-366.
- Benz, H.M., and R.B. Smith (1988). Elastic-wave propagation and site amplification in the Salt Lake Valley, Utah, from simulated normal faulting earthquakes, *Bull. Seism. Soc. Am.* 78, 1851-1874.
- Ben-Zion, Y., and K. Aki (1990). Seismic radiation from an SH line source in a laterally heterogeneous planar fault zone, *Bull. Seism. Soc. Am.* 80, 971-994.
- Beydoun, W.B., and T.H. Kebo (1987). The paraxial ray method, *Geophysics* 52, 1639-1653.
- Boore, D.M. (1970). Love waves in nonuniform wave guides: finite difference calculations, *J. Geophys. Res.* 75, 1512-1527.
- Boore, D.M. (1972). Finite difference methods for seismic wave propagation in heterogeneous materials, in *Methods in Computational Physics* 11, B.A. Bolt ed., Academic Press, New York, 1-37.
- Bouchon, M., and K. Aki (1977a). Near-field of a seismic source in a layered medium with irregular interfaces, *Geophys. J. Roy. Astr. Soc.* 50, 669-684.
- Bouchon, M., and K. Aki (1977b). Discrete wavenumber representation of seismic source wave fields, *Bull. Seism. Soc. Am.* 67, 259-277.
- Bouchon, M., M. Campillo, and S. Gaffet (1989). A boundary integral equation - discrete wavenumber representation method to study wave propagation in multilayered media having irregular interfaces, *Geophysics* 54, 1134-1140.
- Bravo, M.A., F.J. Sanchez-Sesma, and F.J. Chavez-Garcia (1988). Ground motion on stratified alluvial deposits for incident SH waves, *Bull. Seism. Soc. Am.* 78, 436-450.
- Campillo, M. (1987a). Modeling of SH-wave propagation in an irregularly layered medium - Application to seismic profiles near a dome, *Geophys. Prosp.* 35, 236-249.
- Campillo, M. (1987b). Lg wave propagation in a laterally varying crust and the distribution of the apparent quality factor in central France, *J. Geophys. Res.* 92, 12604-12614.
- Campillo, M., P.Y. Bard, F. Nicollin, and F. Sanchez-Sesma (1988). The Mexico earthquake of September 19, 1985 - The incident wavefield in Mexico City during the great Michoacan earthquake and its interaction with the deep basin,

- Earthq. Spectra 4, 591-608.
- Campillo, M., B. Feignier, M. Bouchon, and N. Béthoux (1993). Attenuation of crustal waves across the Alpine range, *J. Geophys. Res.* 98, 1987-1996.
- Carcione, J.M. (1993). Seismic modeling in viscoelastic media, *Geophysics* 58, 110-120.
- Cerveny, V., I.A. Molotkov, and I. Psencik (1977). Ray method in Seismology, Universita Karlova, Praha.
- Cerveny, V., and I. Psencik (1983). Gaussian beams in two-dimensional elastic inhomogeneous media, *Geophys. J. Roy. Astr. Soc.* 72, 417-433.
- Cerveny, V., and I. Psencik (1984). Gaussian beams in elastic 2-D laterally varying structures, *Geophys. J. Roy. Astr. Soc.* 78, 65-91.
- Cerveny, V., L. Klimes, and I. Psencik (1984). Paraxial ray approximation in the computation of seismic wavefields in inhomogeneous media, *Geophys. J. Roy. Astr. Soc.* 79, 89-104.
- Chapman, C.H., and R. Drummond (1982). Body-wave seismograms in inhomogeneous media using Maslov asymptotic theory, *Bull. Seism. Soc. Am.* 72, S277-S317.
- Chavez-Garcia, F.J., and P.Y. Bard (1989). Effect of random thickness variations on the seismic response of a soft soil layer: Applications to Mexico City, in *Engineering Seismology and Site Response*, A.S. Cakmak and I. Herrera (Editors), Computational Mechanics Publications, Southampton, 247-261.
- Cormier, V.F., and P. Spudich (1984). Amplification of ground motion and waveform complexity in fault zones: examples from the San Andreas and Calaveras Faults, *Geophys. J. Roy. Astr. Soc.* 79, 135-152.
- Cormier, V.F., and G.C. Beroza (1987). Calculation of strong ground motion due to an extended earthquake source in a laterally varying structure, *Bull. Seism. Soc. Am.* 77, 1-13.
- Coutant, O. (1989). Numerical study of the diffraction of elastic waves by fluid-filled cracks, *J. Geophys. Res.* 94, 17805-17818.
- Dablain, M.A. (1986). The application of higher-order differencing to the scalar wave equation, *Geophysics* 51, 54-66.
- Daudt, C.R., L.W. Braille, R.L. Nowack, and C.S. Chiang (1989). A comparison of finite-difference and Fourier method calculations of synthetic seismograms, *Bull. Seism. Soc. Am.* 79, 1210-1230.
- Drake, L. (1980). Love and Rayleigh waves in an irregular soil layer, *Bull. Seism. Soc. Am.* 70, 571-582.
- Dravinski, M. (1983). Scattering of plane harmonic SH wave by dipping layers of arbitrary shape, *Bull. Seism. Soc. Am.* 73, 1303-1319.
- Emmerich, H. (1989). 2-D wave propagation by a hybrid method, *Geophys. J. Int.* 99, 307-319.
- Emmerich, H. (1992). PSV-wave propagation in a medium with local heterogeneities: a hybrid formulation and its applications, *Geophys. J. Int.* 109, 54-64.
- Frankel, A. (1993). Three-dimensional simulations of ground motions in the San Bernardino Valley, California, for hypothetical earthquakes on the San Andreas fault, *Bull. Seism. Soc. Am.* 83, 1020-1041.
- Frankel, A., and J. Vidale (1992). A three-dimensional simulation of seismic waves in the Santa Clara Valley, California, from a Loma Prieta aftershock, *Bull. Seism. Soc. Am.*, 82, 2045-2074.
- Gaffet, S., and M. Bouchon (1991). Source location and valley shape effects on the P-SV displacement field using a boundary integral equation - discrete

- wavenumber representation method, *Geophys. J. Int.* 106, 341-355.
- Gariel, J.C., P.Y. Bard, and K. Pitilakis (1991). A theoretical investigation of source, path and site effects during the 1986 Kalamata earthquake (Greece), *Geophys. J. Int.* 104, 165-177.
- Géli, L., P.Y. Bard, and D.P. Schmitt (1987). Seismic wave propagation in a very permeable water-saturated surface layer, *J. Geophys. Res.* 92, 7931-7944.
- George, T., J. Virieux, and R. Madariaga (1987). Seismic wave synthesis by Gaussian beam summation: A comparison with finite differences, *Geophysics* 52, 1065-1073.
- Gibson, R.L., M. N. Toksöz, and F. Batini (1993). Ray-Born modelling of fracture-zone reflections in the Larderello geothermal field, *Geophys. J. Int.* 114, 81-90.
- Graves, R.W., and R.W. Clayton (1992). Modeling path effects in three-dimensional basin structures, *Bull. Seism. Soc. Am.*, 82, 81-103.
- Gregersen, S., and F. Vaccari (1993). Lg-wave modelling for the North Sea, *Geophys. J. Int.* 114, 76-80.
- Harmsen, S., and S. Harding (1981). Surface motions over a sedimentary boundary for incident plane P and SV waves, *Bull. Seism. Soc. Am.* 71, 655-670.
- HelMBERGER, D.V., G. Engen, and S. Grand (1985a). Notes on wave propagation in laterally varying structure, *J. Geophys.* 58, 82-91.
- HelMBERGER, D.V., G. Engen, and S. Grant (1985b). Upper-mantle cross-section from California to Greenland, *J. Geophys.* 58, 92-100.
- Hill, J., H. Benz, M. Murphy, and G. Schuster (1990). Propagation and resonance of SH waves in the Salt Lake Valley, Utah, *Bull. Seism. Soc. Am.* 80, 23-42.
- Hill, N.R., and A.R. Levander (1984). Resonances of low-velocity layers with lateral variations, *Bull. Seism. Soc. Am.* 74, 521-537.
- Ho-Liu, P., and D.V. HelMBERGER (1989). Modeling regional Love waves: Imperial Valley to Pasadena, *Bull. Seism. Soc. Am.* 79, 1194-1209.
- Hong, H.L., and D.V. HelMBERGER (1978). Glorified optics and wave propagation in non-planar structure, *Bull. Seism. Soc. Am.* 68, 1313-1330.
- Horike, M., H. Uebayashi, and Y. Takeuchi (1990). Seismic response in three-dimensional sedimentary basin due to plane S wave incidence, *J. Phys. Earth* 38, 261-284.
- Hu, L.Z., G.A. McMechan, and J.M. Harris (1988). Elastic finite-difference modeling of cross-hole seismic data, *Bull. Seism. Soc. Am.* 78, 1796-1806.
- Jongmans, D., and M. Campillo (1993). The response of the Ubaye Valley (France) for incident SH and SV waves: Comparison between measurements and modeling, *Bull. Seism. Soc. Am.* 83, 907-924.
- Kagawa, T., S. Sawada, and Y. Iwasaki (1992). On the relationship between azimuth dependency of earthquake ground motion and deep basin structure beneath the Osaka Plain, *J. Phys. Earth* 40, 73-83.
- Kang, I.B., and G.A. McMechan (1993). Effects of viscoelasticity on seismic wave propagation in fault zones, near-surface sediments, and inclusions, *Bull. Seism. Soc. Am.* 83, 890-906.
- Kawase, H. (1988). Time-domain response of a semicircular canyon for incident SV, P, and Rayleigh waves calculated by the discrete wavenumber boundary element method, *Bull. Seism. Soc. Am.* 78, 1415-1437.
- Kawase, H., and K. Aki (1989). A study of the response of a soft basin for incident S, P, and Rayleigh waves with special reference to the long duration observed

- in Mexico City, *Bull. Seism. Soc. Am.* 79, 1361-1382.
- Kawase, H., and K. Aki (1990). Topography effect at the critical SV incidence: possible explanation of damage pattern by the Whittier Narrows, California, earthquake of 1 October 1987, *Bull. Seism. Soc. Am.* 80, 1-22.
- Kawase, H., and T. Sato (1992). Simulation analysis of strong motions in the Ashigara Valley considering one- and two-dimensional geologic structures, *J. Phys. Earth* 40, 27-56.
- Kelly, K.R., R.W. Ward, S. Treitel, and R.M. Alford (1976). Synthetic seismograms: A finite-difference approach, *Geophysics* 41, 2-27.
- Kennett, B.L.N. (1974). Reflections, rays and reverberations, *Bull. Seism. Soc. Am.* 65, 1643-1651.
- Koketsu, K. (1987). 2-D reflectivity method and synthetic seismograms for irregularly layered structures - 1. SH-wave generation, *Geophys. J. Roy. Astr. Soc.* 89, 821-838.
- Koketsu, K., B.L.N. Kennett, and T. Takenaka (1991). 2-D reflectivity method and synthetic seismograms for irregularly layered structures - 2. Invariant embedding approach, *Geophys. J. Int.* 105, 119-130.
- Lee, J.J., and C.A. Langston (1983). Wave propagation in a three-dimensional circular basin, *Bull. Seism. Soc. Am.* 73, 1637-1653.
- Levander, A.R., and N.R. Hill (1985). P-SV resonances in irregular low-velocity surface layers, *Bull. Seism. Soc. Am.* 75, 847-864.
- Liu, S.W., S.K. Datta, M. Bouden, and A.H. Shah (1991). Scattering of obliquely incident seismic waves by a cylindrical valley in a layered half-space, *Earthq. Eng. and Struct. Dyn.* 20, 859-870.
- Mateos, J.L., J. Flores, O. Novaro, T.H. Seligman, and J.M. Alvarez-Tostado (1993). Resonant response models for the Valley of Mexico - 2; the trapping of horizontal P waves, *Geophys. J. Int.* 113, 449-462.
- Maupin, V. (1989). Numerical modelling of Lg wave propagation across the North Sea Central Graben, *Geophys. J. Int.* 99, 273-283.
- McLaughlin, K.L., L.M. Anderson, and A.C. Lees (1987). Effects of local geological structure on Yucca Flats, Nevada Test Site, explosion waveforms: two-dimensional linear finite-difference simulations, *Bull. Seism. Soc. Am.* 77, 1211-1222.
- McMechan, G.A., and W.D. Mooney (1980). Asymptotic ray theory and synthetic seismograms for laterally varying structures: Theory and application to the Imperial Valley, California, *Bull. Seism. Soc. Am.* 70, 2021-2035.
- Mikhailenko, B.G. (1984). Synthetic seismograms for complex three-dimensional geometries using an analytical-numerical algorithm, *Geophys. J. Roy. Astr. Soc.* 79, 963-986.
- Mikhailenko, B.G. (1985). Numerical experiment in seismic investigations, *J. Geophys.* 58, 101-124.
- Moczo, P., P.Y. Bard, and I. Pscencik (1987). Seismic response of two-dimensional absorbing structures by the ray method, *J. Geophys.* 62, 38-49.
- Moczo, P., and P.Y. Bard (1993). Wave diffraction, amplification and differential motion near strong lateral discontinuities, *Bull. Seism. Soc. Am.* 83, 85-106.
- Mossessian, T.K., and M. Dravinski (1987). Application of a hybrid method for scattering of P, SV, and Rayleigh waves by near-surface irregularities, *Bull. Seism. Soc. Am.* 77, 1784-1803.
- Mossessian, T.K., and M. Dravinski (1992). A hybrid approach for scattering of elastic waves by three-dimensional irregularities of arbitrary shape, *J. Phys.*

- Earth 40, 241-261.
- Müller, G. (1984). Efficient calculation of Gaussian-beam seismograms for two-dimensional inhomogeneous media, *Geophys. J. Roy. Astr. Soc.* 79, 153-166.
- Müller, G. (1985). The reflectivity method: a tutorial: *J. Geophys.*, 58, 153-174.
- Nicoletis, L. (1981). Simulation numérique de la propagation d'ondes sismiques dans les milieux stratifiés à deux et trois dimensions: contribution à la construction et à l'interprétation des sismogrammes synthétiques, Thèse, Univ. Pierre et Marie Curie, Paris.
- Novaro, O., T.H. Seligman, J.M. Alvarez-Tostado, J.L. Mateos, and J. Flores (1990). Two-dimensional model for site-effect studies of microtremors in the San Fernando Valley, *Bull. Seism. Soc. Am.* 80, 239-251.
- Nowack, R., and K. Aki (1984). The two-dimensional gaussian beam synthetic method: testing and applications, *J. Geophys. Res.* 89, 7797-7819.
- Ohori, M., K. Koketsu, and T. Minami (1992). Seismic responses of three-dimensionally sediment-filled valleys due to incident plane waves, *J. Phys. Earth* 40, 209-222.
- Papageorgiou, A.S., and J. Kim (1991). Study of the propagation and amplification of seismic waves in Caracas Valley with reference to the 29 July 1967 earthquake: SH waves, *Bull. Seism. Soc. Am.* 81, 2214-2233.
- Paul, A., and M. Campillo (1988). Diffraction and conversion of elastic waves at a corrugated interface, *Geophysics* 53, 1415-1424.
- Pšencik, I. (1979). Ray amplitudes of compressional, shear, and converted seismic body waves in 3D laterally inhomogeneous media with curved interfaces, *J. Geophys.* 45, 381-390.
- Regan, J. (1991). Seismic representation theorem coupling: synthetic P-SV mode sum seismograms for non-homogeneous paths, *Geophys. J. Int.* 106, 587-609.
- Regan, J., and D.G. Harkrider (1989a). Numerical modelling of SH Lg waves in and near continental margins, *Geophys. J. Int.* 98, 107-130.
- Regan, J., and D.G. Harkrider (1989b). Seismic representation theorem coupling: synthetic SH mode sum seismograms for non-homogeneous paths, *Geophys. J. Int.* 98, 429-446.
- Reshet, M., and D. Kosloff (1985). Applications of elastic forward modeling to seismic interpretation, *Geophysics* 50, 1266-1272.
- Reshet, M., D. Kosloff, M. Edwards, and C. Hsiung (1988). Three-dimensional elastic modeling by the Fourier method, *Geophysics* 53, 1184-1193.
- Rial, J.A. (1989). Seismic wave resonances in 3-D sedimentary basins, *Geophys. J. Int.* 99, 81-90.
- Sanchez-Sesma, F.J. (1983). Diffraction of elastic waves by three-dimensional surface irregularities, *Bull. Seism. Soc. Am.* 73, 1621-1636.
- Sanchez-Sesma, F.J., and J. Esquivel (1979). Ground motion on alluvial valleys under incident plane SH waves, *Bull. Seism. Soc. Am.* 69, 1107-1120.
- Sanchez-Sesma, F.J., F.J. Chavez-Garcia, and M.A. Bravo (1988). Seismic response of a class of alluvial valleys for incident SH waves, *Bull. Seism. Soc. Am.* 78, 83-95.
- Sanchez-Sesma, F.J., and M. Campillo (1991). Diffraction of P, SV, and Raileigh waves by topographic features: a boundary integral formulation, *Bull. Seism. Soc. Am.* 81, 2234-2253.
- Schultz, C.A., and M.N. Toksöz (1993). Enhanced backscattering of seismic waves from a highly irregular, random interface: SH case, *Geophys. J. Int.* 114, 91-

- Seligman, T.H., J.M. Alvarez-Tostaco, J.L. Mateos, J. Flores, and O. Novaro (1989). Resonant response models for the Valley of Mexico - 1; the elastic inclusion approach, *Geophys. J. Int.* 99, 789-799.
- Smith, W.D. (1975). The application of finite element analysis to body wave propagation problems, *Geophys. J. Roy. Astr. Soc.* 42, 747-768.
- Stephen, R.A. (1984). Finite difference seismograms for laterally varying marine models, *Geophys. J. Roy. Astr. Soc.* 79, 185-198.
- Toshinawa, T., and T. Ohmachi (1992). Love-wave propagation in a three-dimensional sedimentary basin. *Bull. Seism. Soc. Am.* 82, 1661-1677.
- Trifunac, M.D. (1971). Surface motion of a semi-cylindrical alluvial valley for incident plane SH waves, *Bull. Seism. Soc. Am.* 61, 1755-1770.
- Uebayashi, H., M. Horike, and Y. Takeuchi (1992). Seismic motion in a three-dimensional arbitrary-shaped sedimentary basin, due to a rectangular dislocation source, *J. Phys. Earth* 40, 223-240.
- Vaccari, F., S. Gregersen, M. Furla, and G.F. Panza (1989). Synthetic seismograms in laterally heterogeneous, anelastic media by modal summation of P-SV waves, *Geophys. J. Int.* 99, 285-295.
- Vidale, J.E., D.V. Helmberger, and R.W. Clayton (1985). Finite-difference seismograms for SH waves, *Bull. Seism. Soc. Am.* 75, 1765-1782.
- Vidale, J.E., and D.V. Helmberger (1988). Elastic finite-difference modeling of the 1971 San Fernando, California earthquake, *Bull. Seism. Soc. Am.* 78, 122-141.
- Virieux, J. (1984). SH-wave propagation in heterogeneous media: velocity-stress finite-difference method, *Geophysics* 49, 1933-1957.
- Virieux, J. (1986). P-SV wave propagation in heterogeneous media: velocity-stress finite-difference method, *Geophysics* 51, 889-901.
- Yamanaka, H., K. Seo, and T. Samano (1989). Effects of sedimentary layers on surface wave propagation, *Bull. Seism. Soc. Am.* 79, 631-644.
- Zahradnik, J., P. Moczo, and F. Hron (1993). Testing four elastic finite-difference schemes for behavior at discontinuities, *Bull. Seism. Soc. Am.* 83, 107-129.

Figure legends

Figure 1

Illustration of the method

Figure 2

Comparison of the surface displacement traces obtained using boundary elements with the flat layer solution. The configuration used is displayed in (a). The star indicates the source location. Receivers are located at epicentral distances between 100 and 300km, at 10km interval. The two superposed sets of seismograms are presented in (b). A reduced time equal to the epicentral distance divided by the mantle shear wave velocity has been applied to the traces.

Figure 3

Effect of the presence of a vertical fault. The crustal model and source-receivers configuration are depicted in (a). The surface displacement traces are presented in (b). A reduced time equal to the epicentral distance divided by the mantle shear wave velocity has been applied to the seismograms.

Figure 4

Comparison of the seismograms obtained at an epicentral distance of 300km in presence of a fault (model of Figure 3a) with those obtained for the two flat layered structures situated on the left hand side (crust1) and on the right hand side (crust 2) of the fault.

Figure 5

Effect of a change in crustal thickness. The crustal model and source-receivers

configuration are depicted in (a). The surface displacement seismograms are displayed in (b) with a reduced time based on the mantle shear wave velocity.

Figure 6

Comparison of the seismograms obtained at an epicentral distance of 300km for the laterally-varying crustal model of Figure 5a (Moho) with those calculated for the crustal model with constant 35km thickness (crust 3) and the one with 25km thickness (crust 4).

Figure 7

Snapshots showing the propagation of the seismic wave field for the configuration depicted in Figure 5a. Each frame represents a cross-section of the medium between depths of 0 and 45km and between epicentral distances of 150 and 250km. The first snapshot is taken 39s after the source emission, and the subsequent ones are displayed at 3.5s intervals.

FIGURE 1

A



$$V(P) = V_o(P) + \int_S \sigma(Q) G(P, Q) dQ$$

+ P



+ P'

$$V(P') = \int_S \sigma'(Q) G'(P', Q) dQ$$

B



$$V(P) = V_o(P) + \sum_{i=1}^N \sigma_i \int_{\Delta S_i} G(P, Q) dQ$$

+ P



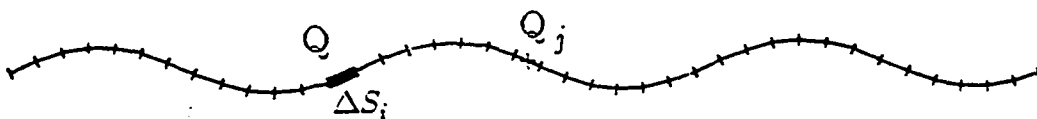
+ P'

$$V(P') = \sum_{i=1}^N \sigma_i' \int_{\Delta S_i} G'(P', Q) dQ$$

C

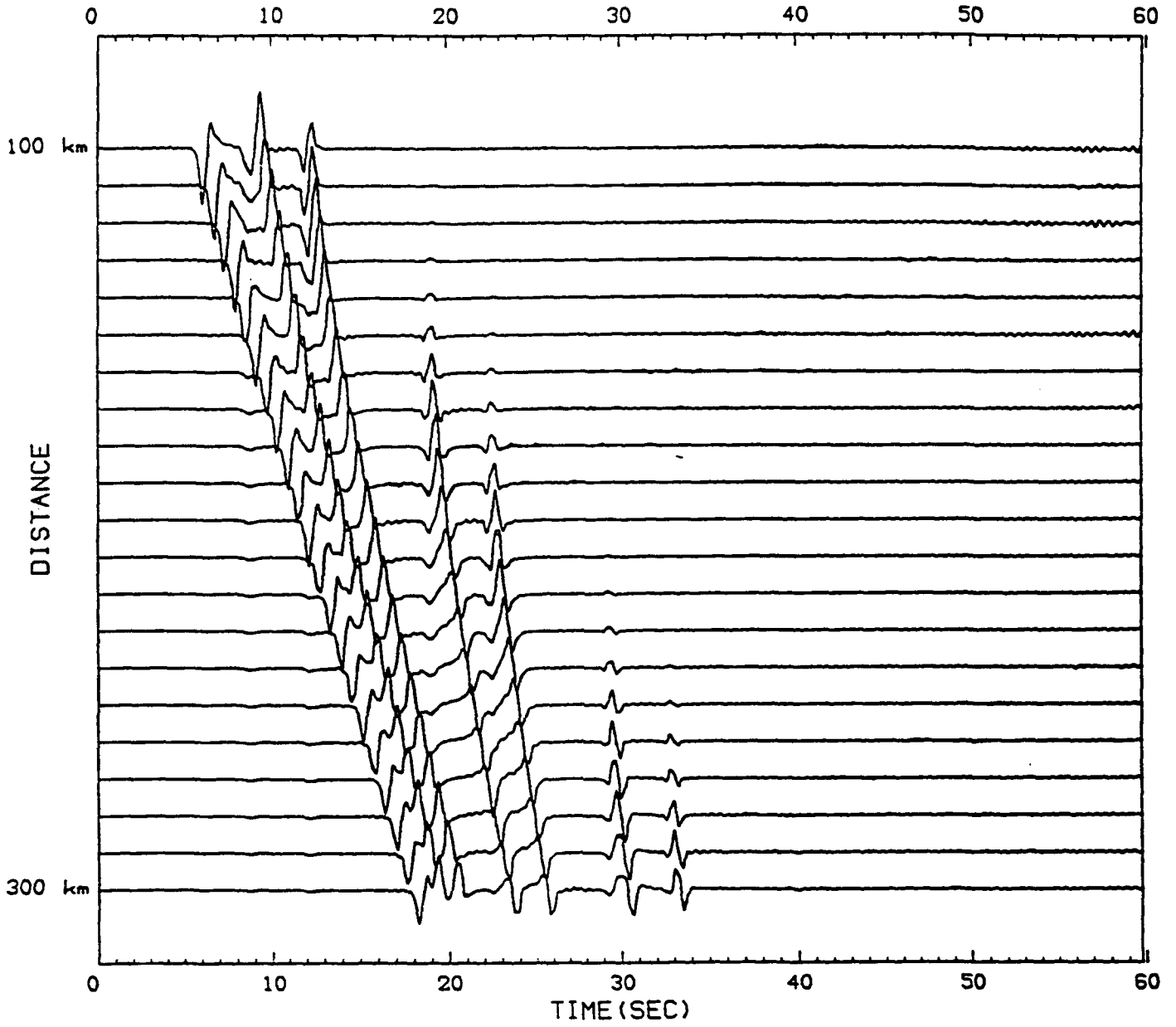


$$V(Q_j) = V_o(Q_j) + \sum_{i=1}^N \sigma_i \int_{\Delta S_i} G(Q_j, Q) dQ$$

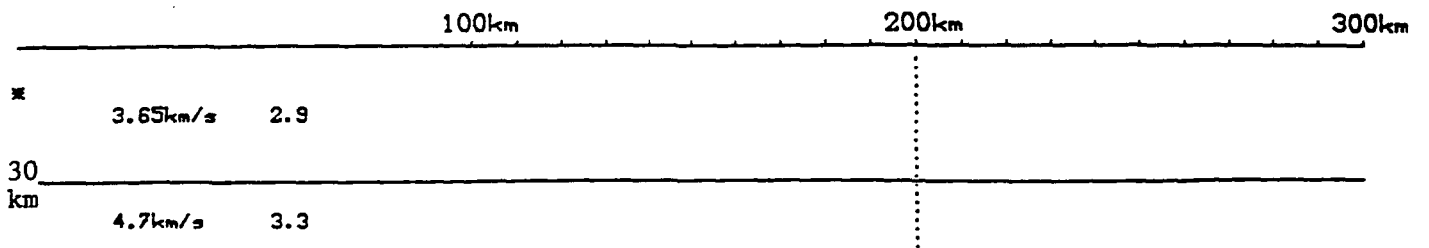


$$V(Q_j) = \sum_{i=1}^N \sigma_i' \int_{\Delta S_i} G'(Q_j, Q) dQ$$

FIGURE 2

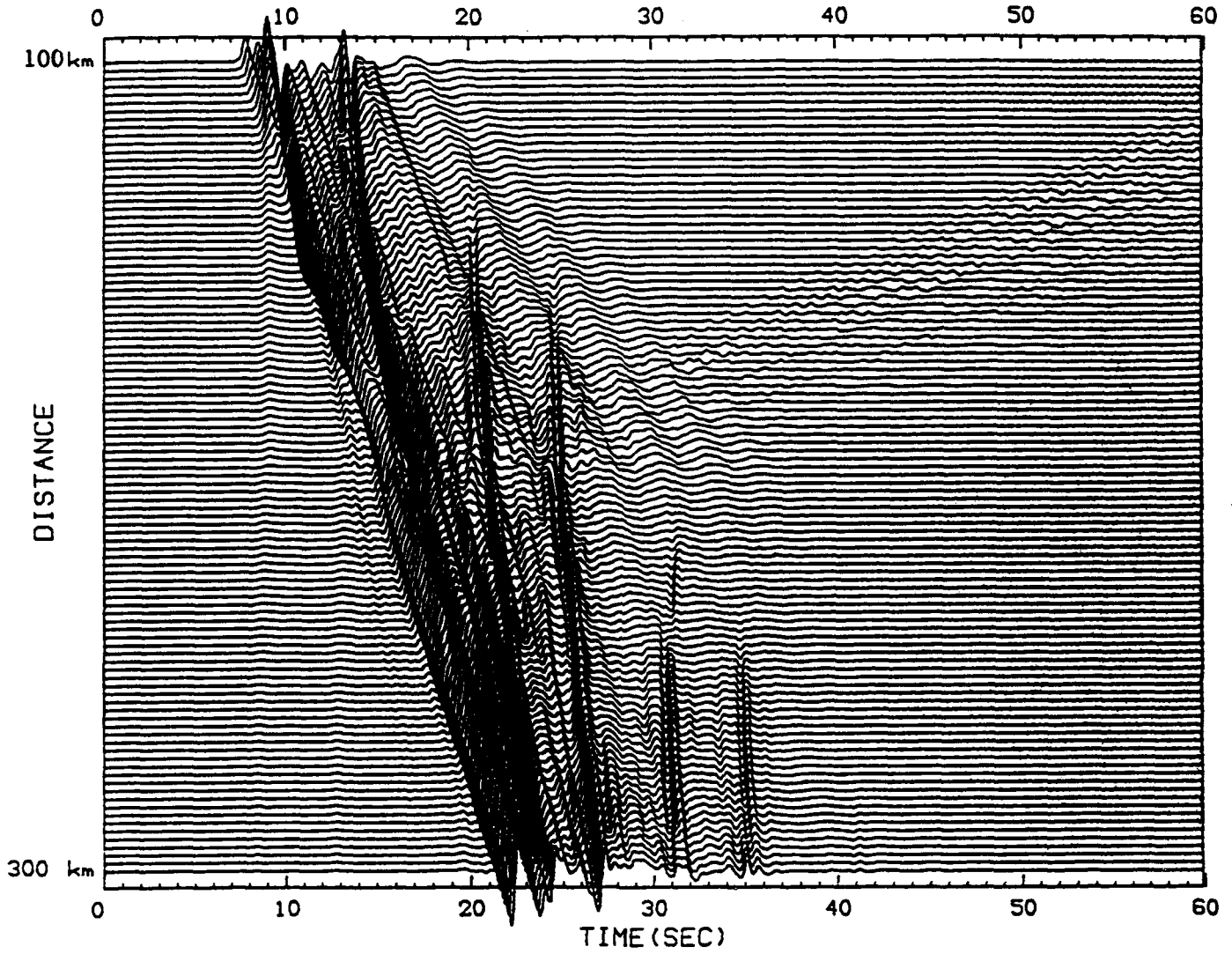


B



A

FIGURE 3



B

	100km	200km	300km
x	3.5km/s	2.8	
	3.65km/s	2.9	
30	3.9km/s	3.1	
km	4.7km/s	3.3	

A

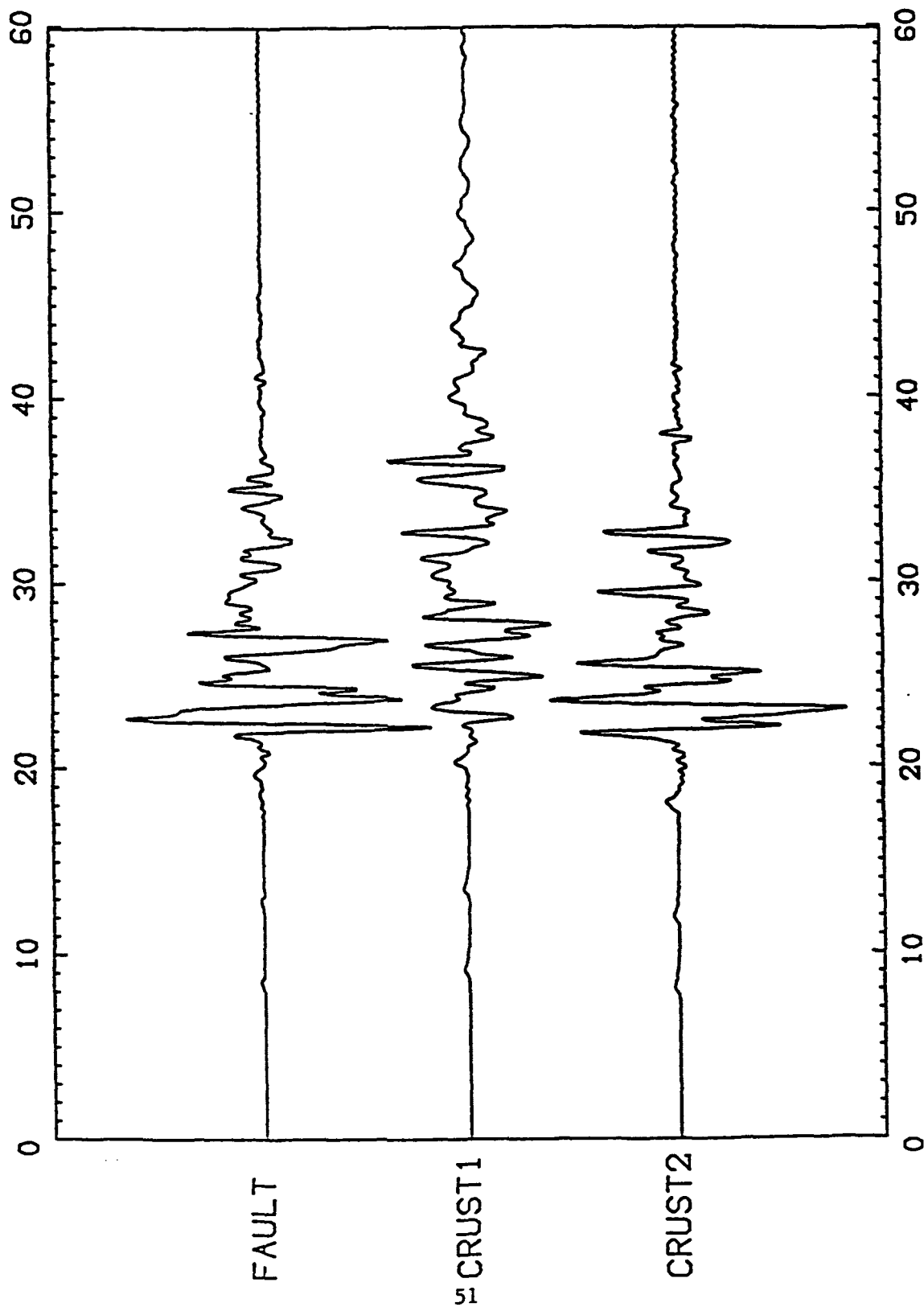
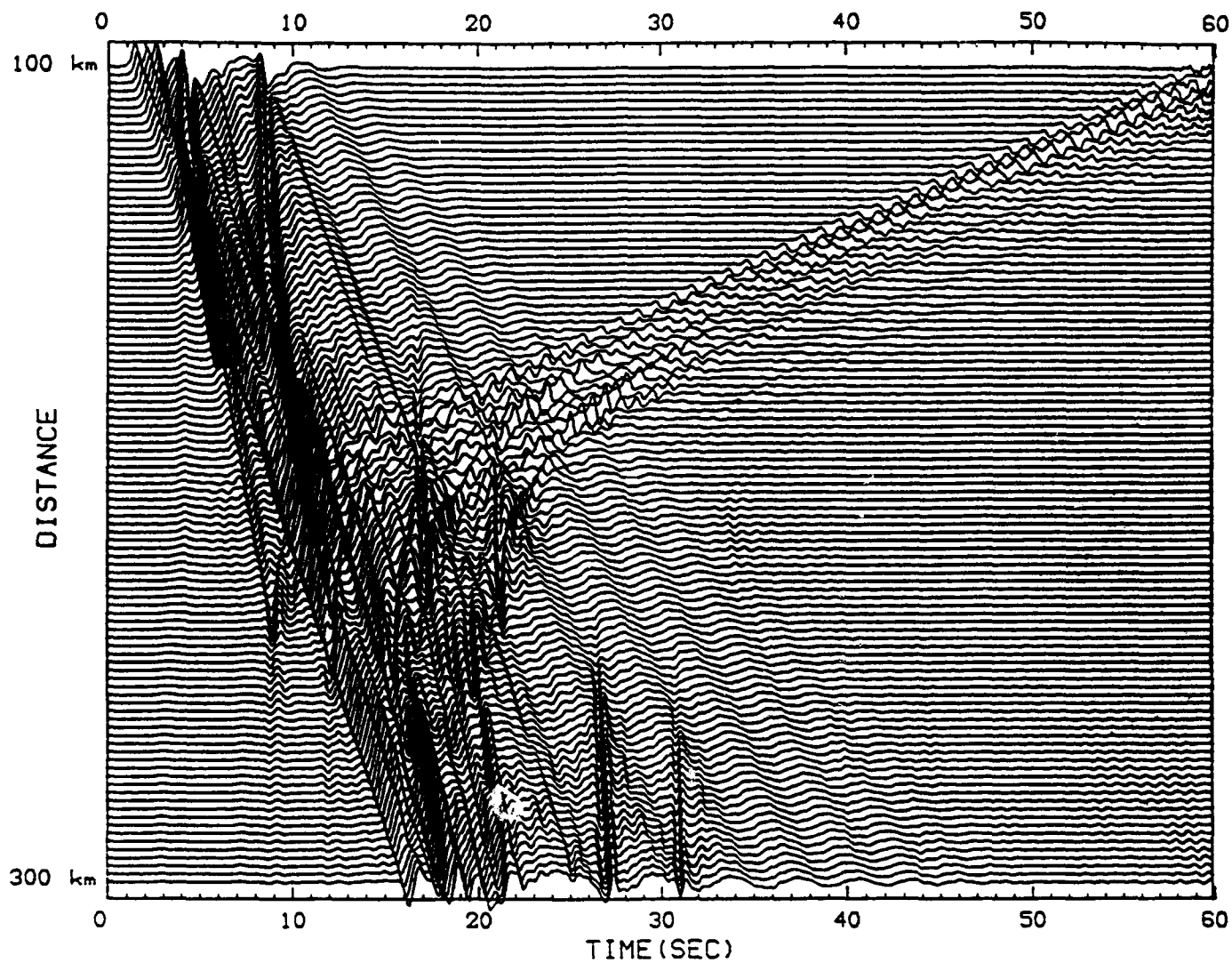
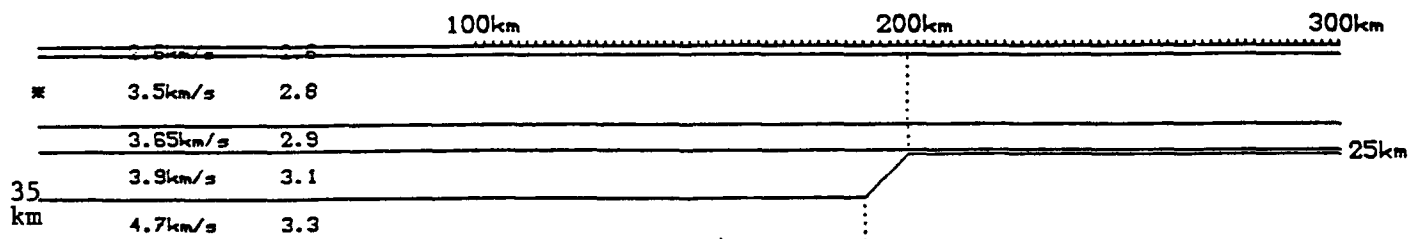


FIGURE 4

FIGURE 5



B



A

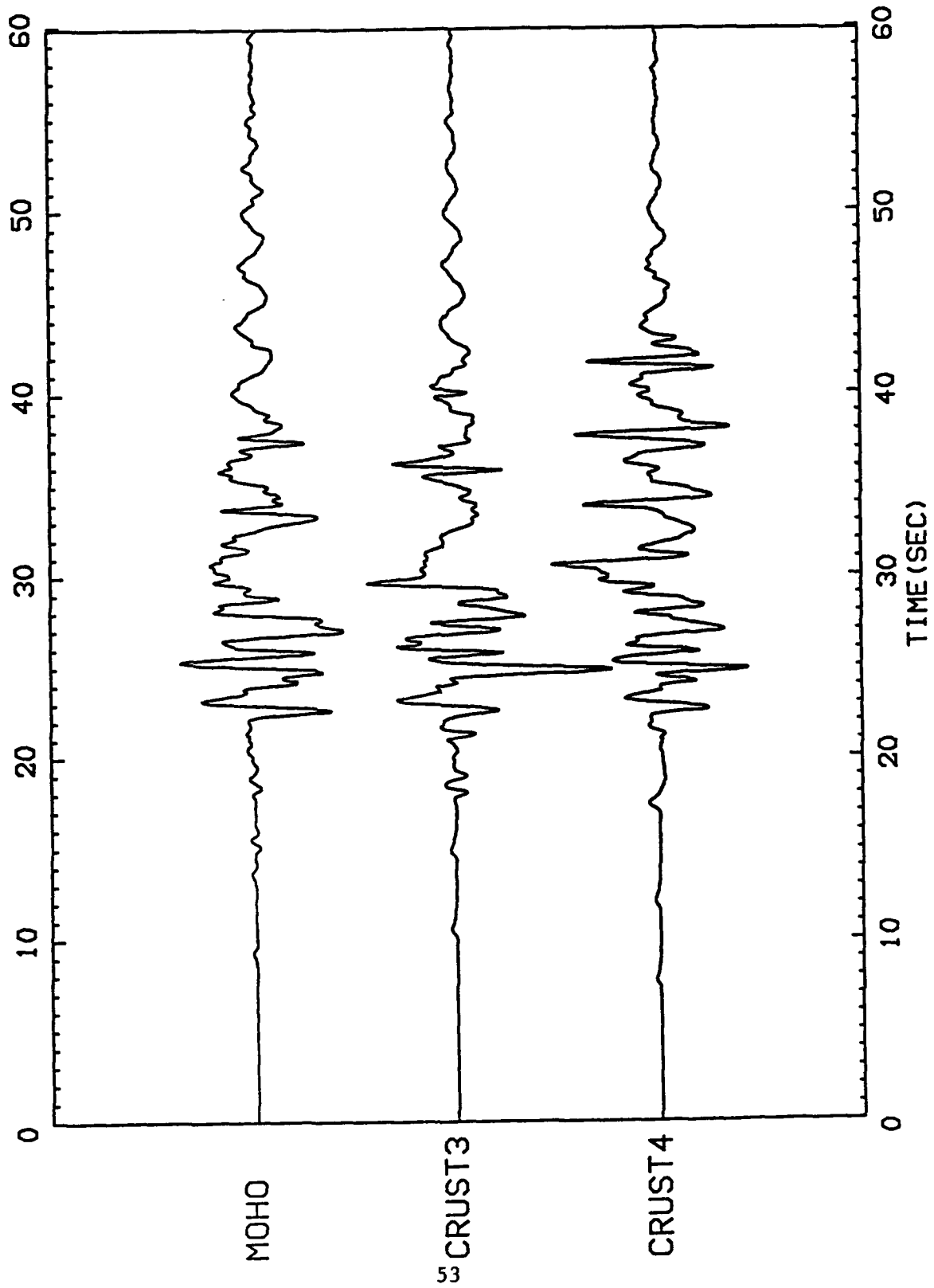
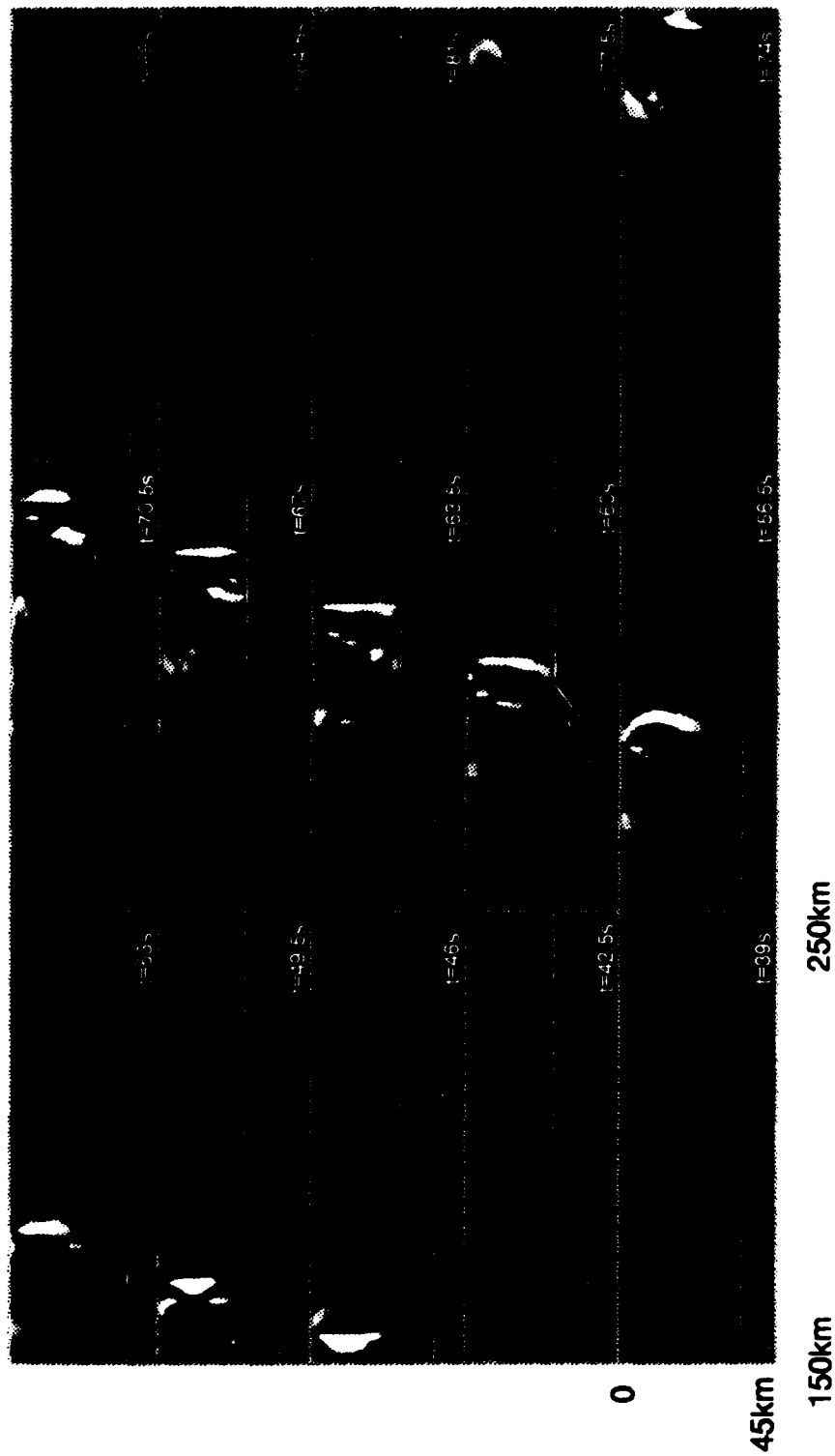


FIGURE 6

PROPAGATION OF LG WAVES IN A CRUST WITH VARYING THICKNESS



II - Modeling of seismic waves generated by nuclear tests in the NTS and Taourirt Tan Afella, Hoggar :

II - 1 Teleseismic wave form modeling including geometrical effects of superficial geological structures near the seismic sources at the NTS:

We analyse observed seismograms of 21 events recorded at teleseismic distances in France from nuclear explosions detonated at Nevada Test Site (NTS). Variations of the displacement waveform, duration, and amplitude are studied in terms of influence of the explosion's medium of burial and location in the laterally heterogeneous Yucca Flat basin. The analysis is made using numerical modelings of data which simulate the modifications of the original source signal by the geometry of the geological surrounding structure. Spalling and non-linear effects are not included in computations. The numerical simulations of the variations are processed using a mixed symbolic and numerical algorithm developed to simulate the ground motions that may be recorded in any kind of two dimensional heterogeneous non-vertical structures. This algorithm is linked (i) to the discrete wavenumber - boundary integral equation method and to the reciprocity theorem to simulate the displacement field radiated to farfield distances by the source site geological structure, and (ii) to ray propagation to propagate the displacement field across the mantle from the source region to the receiver. Variations of the computed displacement amplitudes are as large as twice from one detonation point to another. The shapes of the observed seismograms are modelled with a good reliability for most of the 21 events in the frequency band studied, *i.e.* 0.2Hz - 2.5Hz. A set of 21 relative yield estimates are derived, which include the source site response and thus the amplitude variations induced by the heterogeneous structure of the source region.

II - 2 Modeling of french nuclear tests in Taourirt Tan Afella Massif, Hoggar, Sahara :

The French nuclear test site for underground explosions was located in the Hoggar Massif at the beginning of the 1960's, 4 km west from In Eker, and 150 km north from Tamanrasset in the South of Algeria. The test site is located in a granitic massif, the Taourirt tan Afella (5°2' E; 24°3' N), which is intruded in two gneiss series. The massif is intrusive in the west side of a 1 km thick mylonitic corridor. This corridor approximately oriented north-south separates the In eker gneiss serie (west side) and the Tefedest gneiss serie (east side). Both series present a north-south schistosity.

Teleseismic waveform modeling including geometrical effects of superficial geological structures near to seismic sources

Stéphane Gaffet

Institut de Géodynamique - 250, rue Albert Einstein - Sophia-Antipolis 1 - 06560 Valbonne - France

Abstract

We analyse observed seismograms of 21 events recorded at teleseismic distances in France from nuclear explosions detonated at Nevada Test Site (NTS). Variations of the displacement waveform, duration, and amplitude are studied in terms of influence of the explosion's medium of burial and location in the laterally heterogeneous Yucca Flat basin. The analysis is made using numerical modelings of data which simulate the modifications of the original source signal by the geometry of the geological surrounding structure. Spalling and non-linear effects are not included in computations. The numerical simulations of the variations are processed using a mixed symbolic and numerical algorithm developed to simulate the ground motions that may be recorded in any kind of two dimensional heterogeneous non-vertical structures. This algorithm is linked (i) to the discrete wavenumber - boundary integral equation method and to the reciprocity theorem to simulate the displacement field radiated to farfield distances by the source site geological structure, and (ii) to ray propagation to propagate the displacement field across the mantle from the source region to the receiver. Variations of the computed displacement amplitudes are as large as twice from one detonation point to another. The shapes of the observed seismograms are modelled with a good reliability for most of the 21 events in the frequency band studied, *i.e.* 0.2Hz - 2.5Hz. A set of 21 relative yield estimates are derived, which include the source site response and thus the amplitude variations induced by the heterogeneous structure of the source region.

INTRODUCTION

It has long been recognized that the analysis of seismic waveforms induced by underground nuclear tests could provide valuable information for the understanding of source surrounding site effects. Conversely, these source site effects must be taken into account to obtain reliable source information from seismograms.

Neither the influence of physical properties of the source medium (*e.g.* density, porosity, water saturation) that must be taken into account in source function modeling of underground nuclear tests (Werth and Herbst, 1963; Boardman *et al.*, 1964; Hasegawa, 1971, 1972; Mueller and Murphy, 1971, 1972; Power, 1974), nor non-linear reflections or spalling effects are studied in this paper, *i.e.* we focus our analysis to displacement waveform variations observed at teleseismic distances that can be ascribed to scattering by structure heterogeneities in the vicinity of the source region (Cleary *et al.*, 1975; Bouchon, 1976; McLaughlin *et al.*, 1987; Ferguson, 1988; McLaughlin and Jih, 1988; Stead and Helmberger, 1988).

Figure 1 displays the seismograms recorded by the French Laboratoire de Détection et de Géophysique (LDG) network for detonations in the central region of Yucca Flat, Nevada. These seismograms were constructed by delay and sum of 5 vertical recordings from the central part of France. The epicentral distance is $79^{\circ} - 81^{\circ}$ and the azimuth from North is $39^{\circ} - 41^{\circ}$. The epicentral distance corresponds to an angle of incidence from the source region of 16.95° (Pho and Behe, 1972).

Waveforms differ significantly from one explosion to another. For instance, *Breton* (top in Figure 1) and *Texarkana* (bottom) display short duration signals (2 seconds) while *Jornada* or *Dalhart* show much longer durations (more than 6 seconds). Since the propagation paths from the source region to the receivers are identical, and since the receiver response remains constant for all these explosions, the perturbation and the

duration lengthening of the observed waveforms can be related to reflected paths and to scattering from geological structures located near to the sources. We then limit our study to the farfield influence of the medium structure surrounding the source and therefore ignore the receiver structures in this paper.

In a first part, we describe a new mixed symbolic and numerical procedure developed to compute teleseismic synthetic waveforms for sources located in heterogeneous media. The numerical procedure is an extension of the discrete wavenumber boundary integral equation method (Bouchon and Aki, 1977). For this extension, any kind of non-vertical subsurface or topographic structures can be introduced in the model. In a second part, we study variations of the amplitudes and the waveform perturbations induced by the heterogeneous structure of Yucca Flat as seen at the LDG network. We show that our synthetic seismograms actually reproduce the observed variations in amplitude as well as the anomalous durations of the observed seismograms and that the source medium description used might be accurate enough to describe the global waveforms recorded.

NEAR SOURCE SITE EFFECTS EXPECTED AT YUCCA FLAT

The map of Paleozoic basement depths at Yucca Flat (Figure 2 from Ferguson, 1988) shows a North-South elongated basin with large depth variations in the East-West azimuth. The locations of the 21 studied explosions are depicted by circles. A geological cross section, AA', normal to the main axis of the basin and roughly turned toward the France, is shown in Figure 3. At this cross section, the width of the valley is approximately 12.5km and the maximum depth to Paleozoic basement is 1 km. The water table, *wt*, is from Doty and Thordarson (1983). It separates the dry, *DT*, and the wet, *WT*, tuff levels. Above these volcanic rocks are superficial deposits, *SD*, whose base depth, *sd*, is interpolated from drill hole data given by Fernald *et al.* (1968). Following Bouchon (1976), a superficial layer made up of fan alluvium, *FA*, is introduced. Finally, the Tertiary-Paleozoic contact depth, *tp*, is derived from the works of Taylor (1983), Ferguson *et al.* (1988) and Ferguson (1988). The cross section shows the complexity of the geological units in the central region of Yucca Flat. The aim of this paper is to investigate whether these near source structure heterogeneities could account for the observed waveforms recorded in France.

A basic effect of near source heterogeneities is a non-isotropic radiation pattern of the energy. As a result the source site effect influences on m_b , can be cancelled by averaging records from stations well distributed (in azimuths and distances) around the source. But by contrast, if only records from narrow aperture network are available, such as from the LDG network, it is of critical importance to take the near source site effects into account (McLaughlin *et al.*, 1987, McLaughlin and Jih, 1988).

MODELING: METHOD OF COMPUTATION

The farfield *P*-wave displacement, DIS_{far} , is assumed to result from the convolution of the source function, *SOU*, with the source site response SIT_{sou} , with the propagation path response, *PRO*, with the receiver site response, SIT_{rec} , and with the recording system response, *INS*. Thus

$$DIS_{far} = SOU * PRO * INS * SIT_{rec} * SIT_{sou} \quad (1)$$

Different formulations of the source function *SOU* have been proposed in terms of reduced displacement potential, (see for example the Haskell model (1967) and two modified forms by von Seggern and Blandford (1972) and by Helmberger and Hadley (1981)). The source formulation used in this paper is the one given by Mueller and Murphy (1971), which takes into account both the yield and the detonation depth. This model involves scaling factors that depend on the source medium and which have been empirically determined for different source environments (Viecelli, 1973; Aki *et al.*, 1974; Murphy, 1977; Denny and Johnson, 1991).

The first few seconds of the teleseismic observations at distances of interest (*i.e.* 80°) essentially consist of paths that propagated across the mantle. Assuming ray propagation in the mantle, the attenuation along these paths can be described by the Futterman (1962) anelastic attenuation formulation, which in the frequency domain, is given by

$$PRO = \exp\left(-\pi ft^* \left(1 - \exp\left(-\frac{f}{f_0}\right)\right)\right) \exp\left(-2i\pi ft^* \left(Q - \frac{1}{\pi} \text{Log}_e \frac{\epsilon}{f_0}\right)\right) \exp\left(2i ft^* \text{Log}_e f\right) \quad (2)$$

where f is frequency, $t^* = \int_{path} \frac{Q^{-1}}{v} ds$ represents the ray path-integrated effect of the mantle quality factor Q , f_0 is the frequency above which dispersion occurs in the mantle ($f_0 > 0$), ϵ is the Euler constant. In the 0.2Hz - 2.5Hz frequency band the t^* value can vary between 0.1 and 0.8 (Frasier and Filson, 1972; Cormier, 1982; Der and Lees, 1985). In (2) the first exponential scales the amplitude according to the factor t^* , the second term introduces a phase delay, and the last term represents the frequency dispersion function with a phase advance for $f > 1\text{Hz}$ and a phase delay for $f < 1\text{Hz}$. This description of the ray attenuation in the mantle implies that the geometrical spreading remains constant for all the explosions studied, which is the case in the source-receiver configuration studied.

The response of the LDG network short period recording system, *INS*, is dominated by the seismometer response function with a characteristic frequency of 1Hz and a damping factor of $1/\sqrt{2}$.

The receiver response, *SIT_{rec}*, remains constant for all the explosions studied and is assumed to be flat over all the frequency band for the next computations. The term *SIT_{ou}*, computed using the discrete wavenumber - boundary integral equation method, contains the response of the site geological structure surrounding the source.

Numerical method for source site effects modeling

Different numerical methods have been investigated to study the influences of the near source heterogeneities on the teleseismic *P*-wave seismograms. Hasegawa (1971 and 1972) developed a method and correlated the recorded seismogram shape to the geological complexity of the source environments. Bouchon (1976) proposed an alternative method which is related to the Thomson-Haskell method (Thomson, 1950; Haskell, 1953) and to the reciprocity theorem. He demonstrated the great influence of the source depth and of the burying medium on the m_b estimates. The main limitation of these methods is that the medium must be made up of flat layers. Such a simplification does not apply, even approximately, to the Yucca Flat basin (Figure 2).

Another method proposed by Aki and Larner (1970) has been used by Ferguson (1988) for Yucca Flats explosion modelings, and other empirical or data analysis methods (Taylor, 1983; Lay and Welc. 1987; Lay 1987a and 1987b) emphasize the effect of near source heterogeneous structures on the farfield displacement records. These methods only use a few frequencies to estimate the displacement spectrum, and hence to estimate the yield.

The algorithm developed below removes the restrictions of the previous methods which assume flat-layered media or are limited to a few amplitude samples computed in the frequency domain. This algorithm, in association with the discrete wavenumber - boundary integral equation method and with the reciprocity theorem, is able to compute the complete waveform in the time domain for events located in any kind of topography and subsurface structure.

Continuity of the stress-displacement field across the interfaces

We assume that the structure of the medium studied is entirely described by a set of interfaces as shown in Figure 3. An interface is defined as the boundary that separates two given media (one of the two media may be the vacuum, *i.e.* the boundary is a free surface). Each medium is thus generally bounded by more than one interface. We use the

matrix formulation to describe the problem and do not make explicit the content of these matrices. The reader may refer to Gaffet and Bouchon (1989), Bouchon *et al.* (1989) and Gaffet and Bouchon (1991) for the complete mathematical formulation.

In the discrete wavenumber - boundary integral equation method, each side of an interface i , is associated with a distribution of regularly spaced horizontal and vertical forces (see Figure 4). The notation Q_i^I , is used to represent the vectorial forces located on each side of the interface i in contact with the media I . The potentials radiated by these forces are used to compute the field diffracted by all of the interfaces. The field diffracted from an interface j by its forces located in the medium J and received by the side of an interface i in contact with the medium I is given by the product $A_{ji}^I Q_j^J$. At this first step of the description, the interface i can receive the diffracted field in medium I from the interface j if and only if (*iff*) $I = J$. The dimension of the matrix A_{ji}^I , equals $4M_i \times 2M_j$ in the $P - SV$ problem and $2M_i \times M_j$ in the SH problem, M_i and M_j being the number of points used to define the interfaces i and j .

We introduce, now, a term written S_i^I that describes a seismic source located within the medium I , that acts on the interface i . Using the notations previously defined, we can write the equation which represents the interactions between the interface i and all the interfaces that describe the model.

$$S_i^I + A_{ii}^I Q_i^I + \sum_{j \neq i} A_{ji}^I Q_j^{J=I} = S_i^{I'} + A_{ii}^{I'} Q_i^{I'} + \sum_{j \neq i} A_{ji}^{I'} Q_j^{J=I'}, \text{ if } i \text{ separates 2 media:} \quad (4)$$

$$S_i^I + A_{ii}^I Q_i^I + \sum_{j \neq i} A_{ji}^I Q_j^{J=I} = 0, \text{ if } I' \text{ in (4) is vacuum} \quad (5)$$

Initiation of the algorithm: first step of elimination procedure

The equations (4) and (5) are repeated for each interface i and each product of type $A_{ji}^I Q_j^J$ is computed *iff* $I = J$. (4) and (5) are rewritten below to describe the system of matrix that initiate the first step of the algorithm, *i.e.* level $l = 0$. The following series of matrices and vectors is obtained for each interface i

$${}^0 a_i = [A_{ii}^I \mid -A_{ii}^{I'}], \quad {}^0 \beta_i = {}^0 a_i^{-1} (S_i^{I'} - S_i^I) \quad (6)$$

${}^0 a_i$ is a $4M_i \times 4M_i$ matrix (*i.e.* $P-SV$ case) or a $2M_i \times 2M_i$ matrix (*i.e.* SH case) that is constructed by concatenation, as indicated by the vertical bar, of the two rectangular matrices A_{ii}^I and $-A_{ii}^{I'}$. Then, for each interface j acting on the interface i , we have to compute

$${}^0 b_{ji}^{J'I} = {}^0 a_i^{-1} [A_{ji}^{I'} \mid -A_{ji}^I] \quad (7)$$

The terms A_{ji}^I exist *iff* it has been computed in (4) and (5), *i.e.*, *iff* at least one, non *vacuum*, of the two media J or J' in contact with interface j is also in contact with i . Thus for each interface i , we obtain

$$Q_i = {}^0 \beta_i + \sum_{j, j \neq i} {}^0 b_{ji}^{J'I} Q_j \quad (8)$$

In (8), the vectors Q_i and Q_j correspond to the forces applied on each sides of the interfaces i and j .

$$Q_i = \begin{pmatrix} Q_i^I \\ Q_i^{I'} \end{pmatrix} \text{ and } Q_j = \begin{pmatrix} Q_j^J \\ Q_j^{J'} \end{pmatrix} \quad (9)$$

Symbolic elimination

We solve the linear system of matrices described in (8) using symbolic Gauss Jordan elimination. The unknowns are the vectors Q_i and the elements of the system are the rectangular matrices $b_{ji}^{JJ'}$. The system may be sparse depending on interaction between interfaces i and j , i.e. depending on the topology of the structure. Using (8), at step l of elimination, we obtain

$$Q_i = {}^{l-1}\beta_i + {}^{l-1}b_{ii}^{LI} Q_l + \sum_{j>l, j \neq i} {}^{l-1}b_{ji}^{JJ'} Q_j, \text{ for } i > l \quad (10)$$

The main difficulty is to avoid multiplication between null terms at step l , i.e. the terms corresponding to non interactive interfaces. An automatic symbolic procedure is adopted which considers that the product ${}^{l-1}b_{ii}^{LI} Q_l$ must be taken into account *iff* there exists a fictive path, called C_1 , that may cross the interfaces 1 to l to connect the interfaces l and i , allowing the diffracted field emitted by the interface l in the medium L or L' to reach the interface i in the medium I or I' . The same condition is applied to take into account the product ${}^{l-1}b_{ji}^{JJ'}$ Q_j . A path, called C_2 , must cross the interfaces 1 to l to allow to the field diffracted by the interface j in the medium J or J' to be received by the interface i in the medium I or I' .

This mixing of simultaneously numerical calculation and symbolic determination whether a computation has to be made is the crux of the proposed method.

In a similar way we also express Q_l as

$$Q_l = {}^{l-1}\beta_l + {}^{l-1}b_{il}^{IL} Q_i + \sum_{j>l, j \neq i} {}^{l-1}b_{jl}^{JL} Q_j \quad (11)$$

The product ${}^{l-1}b_{il}^{IL} Q_i$ must now be taken into account *iff* a path, called C_1' , exists and crosses the interfaces 1 to l which permits at step l to the field diffracted by the interface i in the medium I or I' to be received by the interface l in the medium L or L' . Finally, to take into account the product ${}^{l-1}b_{jl}^{JL} Q_j$, a path, called C_3 , must exist across the interfaces 1 to l which allows the field diffracted by the interface j in the medium J or J' to be received by the interface l in medium L or L' .

Then if we replace Q_l in (8) by its expression given in (9) we get

$$Q_i = ({}^{l-1}\beta_i + {}^{l-1}b_{ii}^{LI} {}^{l-1}\beta_l) + {}^{l-1}b_{ii}^{LI} {}^{l-1}b_{il}^{IL} Q_i + \sum_{j>l, j \neq i} ({}^{l-1}b_{ji}^{JJ'} + {}^{l-1}b_{ii}^{LI} {}^{l-1}b_{jl}^{JL}) Q_j \quad (12)$$

and thus

$$Q_i = \left[I - {}^{l-1}b_{ii}^{LI} {}^{l-1}b_{il}^{IL} \right]^{-1} ({}^{l-1}\beta_i + {}^{l-1}b_{ii}^{LI} {}^{l-1}\beta_l) + \sum_{j>l, j \neq i} \left[I - {}^{l-1}b_{ii}^{LI} {}^{l-1}b_{il}^{IL} \right]^{-1} ({}^{l-1}b_{ji}^{JJ'} + {}^{l-1}b_{ii}^{LI} {}^{l-1}b_{jl}^{JL}) Q_j \quad (13)$$

We then obtain

$$Q_i = {}^l\beta_i + \sum_{j>l, j \neq i} {}^l b_{ji}^{JJ'} Q_j \quad (14)$$

The different products in (13) that define the matrices $'b_{ij}'$ and the vectors $'Q_i$ in (14) are computed *iff* the corresponding paths $C_1, C_1', C_2,$ or C_3 can be found, *i.e.*, we determine symbolically whether or not the products of matrices in (13) have to be numerically calculated. We have described the iteration $l-1$ to l of the matrix linear system reduction process that has now to be repeated for $l = 1$ onto the N^{th} interface to complete the resolution of (8).

Backpropagation of the forces

At the end of this elimination process, *i.e.* (10), ..., (14), we obtain an upper triangular system of matrices. Its resolution is straightforward that we call backpropagation of the forces. The last iteration in (14) gives directly the force vector $Q_{N^{th}}$. This vector is then introduced in the $N^{th} - 1$ expression to compute $Q_{N^{th}-1}$, and so on to back compute all the forces that must be applied on both sides of each interface in order to insure the continuity of the stress-displacement field across the interfaces considered.

Note that this method described here may actually be applied to solve any kind of linear band system with the minimum need of computer memory (each matrix may be saved on mass storage until it is needed), and with the maximum of numerical stability.

NUMERICAL MODELING OF YUCCA FLAT DATA

The map given in Figure 2 displays the distribution of the 21 studied detonations. Figure 3 shows the corresponding cross section AA' used for this study. The elastic parameters of each medium summarized in Table 1 are those from Ferguson (1988). α, β, ρ and ν denote the P and SV velocities, the density and Poisson's ratio.

The focal parameters of the explosions are listed in Table 2 (from USGS bulletin). The locations of the 21 explosions are projected onto the vertical cross section AA' in Figure 5. We assume that the 21 locations have accurate depths and therefore determine the medium of burial. Under this assumption 4 explosions are detonated above the water table in tuff (*e.g. Draughts, Tajo, Strake, and Tezarkana*). Most of them are below the water table. *Breton* is assumed to be buried in the sediment deposit level (SD , Figure 1) and appears to be very near the closing area (CA) of all the media near the horst Paleozoic structure.

Influence of the source location

We compute the seismograms that should be recorded in France for a line of explosions buried at a depth of 650m in the wet tuff layer, and for yields of 1kt, 10kt, and 100kt. The Mueller and Murphy (1971) source function is used with the parameters corresponding to the wet tuff-rhyolite medium (Murphy, 1977). The t^* value is taken to be 0.7 (Cormier, 1982). The maximum amplitudes and the location of the corresponding explosions are presented in Figure 6. We obtain a strong variation by a factor of 2 of the maximum 0 to peak amplitude with the location of the detonations (Figure 6 bottom), which appears to be insensitive to the energy of the explosions (*i.e.* for 1kt, 10kt, and 100kt plotted respectively as black losanges, plus signs, and crosses).

The amplification is maximum for detonations located in the western zone (WZ Figure 6). In this area, the amplitude variation is very sensitive to the location of the detonations: amplification can vary by as much as 40% for a horizontal shift of only a few hundred meters of the detonation point. The minimum amplification is observed for explosions located in the eastern saturated (EZ) tuff zone. This minimum is not only related to the shape of the Paleozoic basement but rather appears to integrate the geometry of all the surrounding heterogeneous structures. The maximum attenuation occurred for shots detonated in the western part of this zone. We obtain at this point a relative attenuation larger than 50% if compared to the absolute basin maximum amplification, and 40% when compared to the eastern zone maximum amplitude.

These preliminary results confirm the conclusion of previous investigation regarding the necessity to take into account the heterogeneous structures that may exist in the vicinity of seismic sources to accurately analyse seismogram amplitudes obtained from a narrow aperture network.

Waveform fitting - Yield inversion

Synthetic seismograms have been computed using the Mueller and Murphy (1971) source function and compared to our records. The constraint used to construct the synthetic waveforms is simply to best fit the relative amplitudes of the observed seismograms by only adjusting the yield. These best fitting seismograms are shown in Figure 7. *Rummy* ($m_b = 5.7$), which has the maximum amplitude observed was chosen as the reference event. We therefore arbitrarily fix its yield to be 150kt. This calibration then allows us to estimate the yields of the other explosions. The two last columns of Table 3 summarize the yields obtained using this calibration and the observed relative amplitudes. These two columns illustrate the yield variations that may occur between explosions such as *Hermosa* and *Lowball* or *Rummy* and *Jornada* (detonated in wet tuff), or *Tajo* and *Tezarkana* (detonated in dry tuff), having the same seismogram amplitudes.

The quality of the fits is quantified using the correlation coefficient computed over the first 5 seconds of signal (see last column in Figure 7). Most part of the seismograms have synthetic waveforms which closely follow the observed ones. The longer duration of the ground motion observed for events in the central region (*i.e.* around *Tahoka*) is correctly reproduced, as well as the relative amplitudes of the two first troughs corresponding to the *P* and *pP* wave arrivals. The fourth peak which induces duration lengthening, arrives approximately 4 seconds after the first arrival. Such a delay is observed on the real seismograms.

There are different ways to explain the slight discrepancy between synthetic *pP-P* and observed *pP-P*, *e.g.* a too shallow depth of burial, too large wave velocities or lateral velocity variations as reported by Johnson and McEvelly (1990). We however prefer other explanations which concern the representation of the source radiation for an explosion that takes place near an interface (*i.e.* at distances smaller than the elastic radius).

(i) For numerical modeling assuming linear elasticity, the source used to represent the nuclear explosion must not be considered as a point source because the elastic zone size becomes important in comparison with the heterogeneity dimensions. Likewise, the spherical elastic zone shape in a homogeneous space should be modified in presence of different media having different compaction properties (Murphy, 1980). Therefore, we must take into account the elastic zone shape and the size of an explosion in heterogeneous medium to explain variations in the frequency content and in the amount of seismic energy radiated outside of the basin. (ii) Another reason for waveform discrepancy is that secondary sources such as spall and non linear reflection at free surface are not included in this work which addresses only the geometrical influence of the structure surrounding the source.

Thus if the shot location in a heterogeneous medium plays a great role in shaping the seismograms, it appears necessary to take care in the explosion source model to have the best possible source as input into the diffracting heterogeneous media system.

CONCLUSIONS

We have implemented in a new numerical algorithm, the discrete wavenumber - boundary integral equation method to simulate source site effects which could account for the farfield radial ground motions. The computation uses the reciprocity theorem to simulate 21 underground explosions from the central region of Yucca Flat valley, Nevada, and recorded in France. This study confirms that teleseismic seismogram waveforms and amplitudes are very sensitive to the shot location for explosions located in a heterogeneous sedimentary-filled basin. We have obtained a good correlation between both shape and duration of

synthetic seismograms and the observed ones. This indicates that the location of the explosions is accurately taken into account in our calculations and that the heterogeneities in the source region must be taken into account for waveform analysis and for yield estimates. Source site effects such as these are of great importance in calibrating a receiver response in relation to a specified site, as well as in calibrating the site of a single explosion. We show that if the near source heterogeneities can be reliably accounted for, the uncertainty on the yield estimate of a nuclear test by a narrow aperture network would be significantly reduced.

REFERENCES

- Aki, K., M. Bouchon, and P. Reasenber, 1974. Seismic source for an underground nuclear explosion. *Bull. Seism. Soc. Am.* **64** , 131-148
- Aki, K. and K. L. Larner, 1970. Surface motion of a layered medium having an irregular interface due to incident plane *SH* waves. *J. Geophys. Res.* **75** , 933-954
- Bard, P.-Y., 1982. Diffracted waves and displacement field over two dimensional elevated topography. *Geophys. J. R. Astr. Soc.* **71** , 731-760
- Bard, P.-Y. and M. Bouchon, 1980. The seismic response of sediment-filled valleys. Part 1. The case of incident *P* and *SV* waves. *Bull. Seism. Soc. Am.* **70** , 1921-1941
- Bard, P.-Y. and M. Bouchon, 1985. The two-dimensional resonance of sediment-filled valleys. *Bull. Seism. Soc. Am.* **75** , 519-541
- Boardman, C. R., D. D. Rabb, and R. D. McArthur, 1964. Responses of four rock mediums to contained nuclear explosions. *J. Geophys. Res.* **69** , 3457-3469
- Bouchon, M., 1973. Effect of topography on surface motion. *Bull. Seism. Soc. Am.* **63** , 615-632
- Bouchon, M., 1976. Teleseismic body wave radiation from a seismic source in a layered medium. *Geophys. J. R. astr. Soc.* **47** , 515-530
- Bouchon, M. and K. Aki, 1977. Discrete wave-number representation of seismic source wave fields. *Bull. Seism. Soc. Am.* **67** , 259-277
- Bouchon, M., M. Campillo, and S. Gaffet, 1989. A boundary integral equation-discrete wavenumber representation method to study wave propagation in multilayered media having irregular interfaces. *Geophysics* **54** , 1134-1140
- Cleary, J. R., D. W. Wing, and R. A. W. Haddon, 1975. *P*-wave in the earth's crust and upper mantle. *Geophys. J.* **43** , 861-872
- Cormier, V. F., 1982. The effect of attenuation on seismic body waves. *Bull. Seism. Soc. Am.* **72** , S169-S200
- Denny, M. D. and L. R. Johnson, 1991. The explosion seismic source function: models and scaling laws reviewed. *Submitted to American Geophysical Union*
- Der, Z. A. and A. C. Lees, 1985. Methodologies for estimating $t^*(f)$ from short period body waves and regional variations of $t^*(f)$ in the United States. *Geophys. J. R. astr. Soc.* **82** , 125-140
- Doty, G. C. and W. Thordarson, 1983. Water table in rocks of cenozoic and paleozoic age, 1980, Yucca Flat, Nevada test site, Nevada. *Department of the Interior - United States Geological Survey*
- Ferguson, J. F., R. N. Felch, C. L. V. Aiken, J. S. Oldow, and H. Dockery, 1988. Models of the Bouguer gravity and geologic structure at Yucca Flat, Nevada. *Geophysics* **53** , 231-244
- Ferguson, J. F., 1988. Body waves magnitude variation at Yucca Flat, Nevada. *Bull. Seism. Soc. Am.* **78** , 863-872
- Fernald, A. T., G. S. Corchary, and W. P. Williams, 1968. Surficial geologic map of Yucca Flat, Nye and Lincoln counties, Nevada. *Department of the Interior - United States Geological Survey*
- Frasier, C. W. and J. Filson, 1972. A direct measurement of earth's short-period attenuation along a teleseismic ray path. *J. Geophys. Res.* **77** , 3782-3787
- Futterman, W. I., 1962. Dispersive body waves. *J. Geophys. Res.* **67** , 5279-5291
- Gaffet, S. and M. Bouchon, 1989. Effects of two-dimensional topographies using the discrete wavenumber - boundary integral equation method in *P-SV* cases. *J. Acoust. Soc. Am.* **85** , 2277-2283

- Gaffet, S. and M. Bouchon, 1991. Source location and boundary shape effects on the P - SV near displacement field using a boundary integral equation - discrete wavenumber representation method. *Geophys. J. Int.* **106** , 341-355
- Hasegawa, H. S., 1971. Analysis of teleseismic signals from underground nuclear explosions originating in four geological environments. *Geophys. J. R. astr. Soc.* **24** , 365-381
- Hasegawa, H. S., 1972. Analysis of amplitudes spectra of P waves earthquakes and underground explosions. *J. Geophys. Res.* **77** , 3081-3096
- Haskell, N. A., 1953. The dispersion of surface waves in multilayered media. *Bull. Seism. Soc. Am.* **43** , 17-34
- Haskell, N. A., 1967. Analytic approximation for the elastic radiation from a contained underground explosion. *J. Geophys. Res.* **72** , 2583-2587
- Helmberger, D. V. and D. M. Hadley, 1981. Seismic source functions and attenuation from local and teleseismic observations of the NTS events JORUM and HANDLEY. *Bull. Seism. Soc. Am.* **71** , 51-67
- Johnson, L. R. and T. V. McEvelly, 1990. OSSY source characterization - Summary report. *Master, LBL, University of California*, 33pp
- Kawase, H. and K. Aki, 1988. Time-domain response of a cylindrical canyon for incident SV , P , and Rayleigh waves calculated by the discrete wavenumber boundary element method. *Bull. Seism. Soc. Am.* **78** , 1415-1437
- Kawase, H. and K. Aki, 1989. A study on the response of a soft basin for incident S , P , and Rayleigh waves with special reference to the long duration observed in Mexico city. *Bull. Seism. Soc. Am.* **79** , 1361-1382
- Kawase, H. and K. Aki, 1990. Topography effect at the critical SV -wave incidence: possible explanation of damage pattern by the Whittier Narrows, California, earthquake of 1 October 1987. *Bull. Seism. Soc. Am.* **80** , 1-22
- Key, F. A., 1967. Signal generated noise recorded at the Eskdalemuir seismometer array station. *Bull. Seism. Soc. Am.* **57** , 27-37.
- Lay, T. (1987a). Analysis of near-source contributions to early P -wave coda for underground explosions. II. Frequency dependence. *Bull. Seism. Soc. Am.* **77** , 1252-1273
- Lay, T. (1987b). Analysis of near-source contributions to early P -wave coda for underground explosions. III. Inversion for isotropic scatterers. *Bull. Seism. Soc. Am.* **77** , 1767-1783
- Lay, T. and J. L. Welc, 1987. Analysis of near-source contributions to early P -wave coda for underground explosions. I. waveform complexity. *Bull. Seism. Soc. Am.* **77** , 1017-1040
- McLaughlin, K. L., L. M. Anderson, and A. C. Lees, 1987. Effects of local geologic structures on Yucca flats, Nevada Test Site, explosion waveforms: two dimensional linear finite difference simulations. *Bull. Seism. Soc. Am.* **77** , 1211-1222
- McLaughlin, K. L. and R.-S. Jih, 1988. Scattering from near source topography: teleseismic observations and numerical simulations. *Bull. Seism. Soc. Am.* **78** , 1399-1414
- Mueller, R. A. and J. R. Murphy, 1971. Seismic characteristics of underground nuclear detonations. Part I: seismic spectrum scaling. *Bull. Seism. Soc. Am.* **61** , 1675-1692
- Murphy, J. R., 1972. Calculated compressional-wave arrivals from underground nuclear detonations. *Bull. Seism. Soc. Am.* **62** , 991-1016
- Murphy, J. R., 1977. Seismic source functions and magnitude determinations for underground detonations. *Bull. Seism. Soc. Am.* **67** , 135-158
- Murphy, J. R., 1980. P wave coupling of underground explosions in various geologic data. Presented at the *Nato Advanced Study Institute on the Identification of Seismic Sources - Oslo, Norway* , 30pp

- Murphy, J. R. and R. A. Mueller, 1971. Seismic characteristics of underground nuclear detonations. Part II: elastic energy and magnitude determinations. *Bull. Seism. Soc. Am.* **61** , 1693-1704
- Pho, H.-T. and L. Behe, 1972. Extended distances and angles of incidence of *P* waves. *Bull. Seism. Soc. Am.* **62** , 885-902
- Power, F.W., 1974. Inelastic calculations in tuff and spectrum scaling considerations. *Env. Res. Corp report NVO-1163-241* , 49pp
- Sánchez-Sesma, F. J. and E. Rosenblueth, 1979. Ground motion at canyons of arbitrary shape under incident *SH* waves. *Int. J. Earthquake Eng. Struct. Dyn.* **7** , 441-450
- Stead, R. J. and D. V. Helmberger, 1988. Numerical-analytical interfacing in two dimensions with applications to modeling N.T.S. seismograms. *Pageoph* **128** , 157-193
- Taylor, S. R., 1983. Three-dimensional crust and upper mantle structure at the Nevada Test Site. *J. Geophys. Res.* **88** , 2220-2232
- Thomson, W. T., 1950. Transmission of elastic waves through the stratified solid medium. *J. Appl. Phys.* **21** , 89-93
- Viecelli, J. A., 1973. Spallation and the generation of surface waves by an underground explosion. *J. Geophys. Res.* **78** , 2475-2487
- von Seggern, D. H. and R. Blandford, 1972. Source time functions and spectra for underground nuclear explosions. *Geophys. J.* **31** , 83-98
- Werth, G. C. and R. F. Herbst, 1963. Comparisons of amplitudes of seismic waves from nuclear explosions in four medium. *J. Geophys. Res.* **68** , 1463-1475

FIGURE CAPTIONS

Figure 1 - Seismograms recorded in France by the French L. D. G. network. The time window is 20 seconds long. Dates, names, and relative amplitudes of all events are given above each seismogram.

Figure 2 - Map of Paleozoic basement at Yucca Flat test site, Nevada. The circles show epicenters of the explosions used in the study. The two first letters of the explosion names are also given (Table 1). The cross section AA' is depicted by the thick bold line. This map is adapted from the map given by Ferguson (1988).

Figure 3 - Cross section AA' (see Figure 2 for location). Lower case letters refer to interfaces (*i.e.* *sd* as basement of sedimentary deposits, *wt* as water table, and *tp* as tertiary-Paleozoic contact depth). Upper case letters refer to geological units (*i.e.* *FA* : fan alluvium, *SD* : sedimentary deposits, *DT* : dry tuff, *WT* : wet tuff, and *PZ* : paleozoic basement). The display vertical exaggeration is 5:1 .

Figure 4 - Description of the interfaces and media notations used in text. We show here three parts of three interfaces *i* , *j* , and *l* . The couples of orthogonal arrows represent the couples of horizontal and vertical forces applied at the sampling points on each side of all interfaces. The name of the media separated by the three interfaces are *I* , *I'* , *J* , *J'* , *L* , and *L'* . The notations used in text to represent the forces applied (*i.e.* Q_i , Q_j , and Q_l) are illustrated in this Figure.

Figure 5 - Locations of the 21 explosions studied in relation to the cross section given in Figure 3. The depths and locations are those given by the USGS bulletin.

Figure 6 - Estimated maximum displacement amplitudes that would be received by the French LDG network for a set of 18 fictitious explosions at Yucca Flat test site, Nevada.

Figure 7 - Comparison of synthetic seismograms (thick bold line) with the observed data (thin bold line) for the 21 explosions studied. The synthetics are 10 seconds long and include the LDG short period seismometer response. Dates of each event are noted to the left. The bold numbers are relative amplitudes recorded in France. The explosion names are followed in the last column by the correlation coefficient between synthetic and observed seismograms.

TABLE 1 - Elastic parameters of media

Medium	$\alpha(m/s)$	$\beta(m/s)$	$\rho(kg/m^3)$	ν
FA	700	330	1500	0.35
SD	1340	640	1770	0.35
DT	2140	1140	1790	0.30
WT	3000	1600	1790	0.30
PZ	4570	2640	2500	0.25

TABLE 2 - Event locations and magnitudes

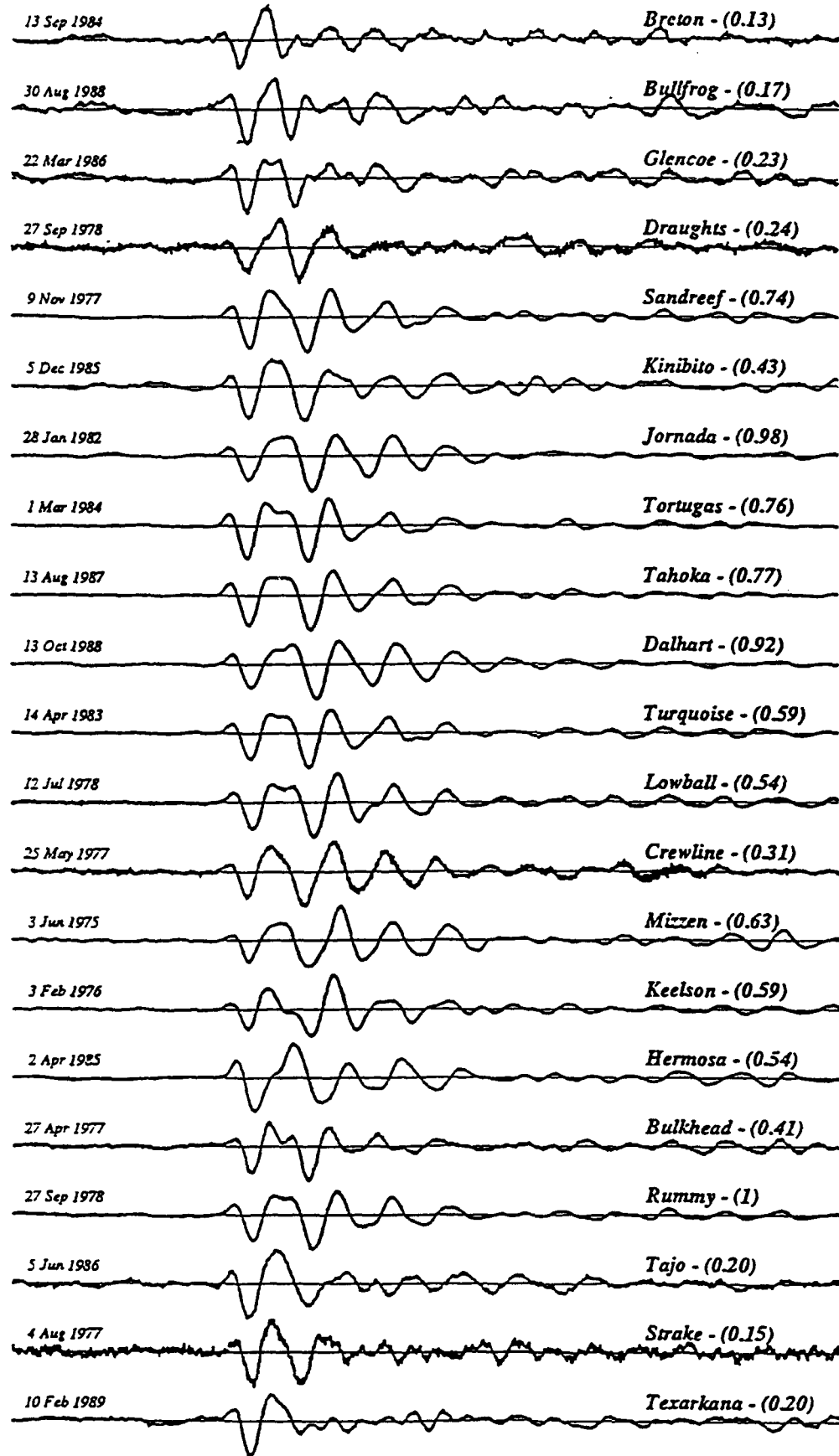
No	Latitude	Longitude	depth (m)	Date	m_b	Event name
1	37.0867	-116.0711	483	13 Sep 1984	5.0	Breton
2	37.0858	-116.0686	500	30 Aug 1988	5.0	Bullfrog
3	37.0831	-116.0661	600	22 Mar 1986	5.1	Glencoe
4	37.0797	-116.0514	442	27 Sep 1978	5.0	Draughts
5	37.0722	-116.0500	701	09 Nov 1977	5.7	Sandreef
6	37.0533	-116.0453	600	05 Dec 1985	5.7	Kinibito
7	37.0914	-116.0511	640	28 Jan 1982	5.9	Jornada
8	37.0658	-116.0464	639	01 Mar 1984	5.9	Tortugas
9	37.0608	-116.0453	600	13 Aug 1987	5.9	Tahoka
10	37.0889	-116.0492	600	13 Oct 1988	5.9	Dalhart
11	37.0728	-116.0458	533	14 Apr 1983	5.7	Turquoise
12	37.0786	-116.0439	564	12 Jul 1978	5.5	Lowball
13	37.0944	-116.0447	564	-25 May 1977	5.3	Crewline
14	37.0947	-116.0361	637	03 Jun 1975	5.7	Mizzen
15	37.0692	-116.0303	640	04 Feb 1976	5.8	Keelson
16	37.0947	-116.0322	640	02 Apr 1985	5.7	Hermosa
17	37.0947	-116.0278	594	27 Apr 1977	5.4	Bulkhead
18	37.0739	-116.0197	640	27 Sep 1978	5.7	Rummy
19	37.0983	-116.0156	500	05 Jun 1986	5.3	Tajo
20	37.0867	-116.0069	518	04 Aug 1977	5.0	Strake
21	37.0767	-116.0006	500	10 Feb 1989	5.2	Texarkana

TABLE 3 - Yields estimated

No	depth (m)	m_b	Event name	buried in	Y_0 (kt)	A / A_0
1	483	5.0	Breton	SD	57	0.13
2	500	5.0	Bullfrog	WT	28	0.17
3	600	5.1	Glencoe	WT	35	0.23
4	442	5.0	Draughts	DT	124	0.24
5	701	5.7	Sandreef	WT	139	0.74
6	600	5.7	Kinibito	WT	79	0.43
7	640	5.9	Jornada	WT	178	0.98
8	639	5.9	Tortugas	WT	135	0.76
9	600	5.9	Tahoka	WT	143	0.77
10	600	5.9	Dalhart	WT	170	0.92
11	533	5.7	Turquoise	WT	108	0.59
12	564	5.5	Lowball	WT	99	0.54
13	564	5.3	Crewline	WT	56	0.31
14	637	5.7	Mizzen	WT	93	0.63
15	640	5.8	Keelson	WT	87	0.59
16	640	5.7	Hermosa	WT	76	0.54
17	594	5.4	Bulkhead	WT	58	0.41
18	640	5.7	Rummy	WT	150	1
19	500	5.3	Tajo	DT	72	0.20
20	518	5.0	Strake	DT	48	0.15
21	500	5.2	Texarkana	DT	52	0.20

FIGURE 1

0 1 2 3 4 5 6 7 8 9 10 11 12 13 14 15 16 17 18 19 20

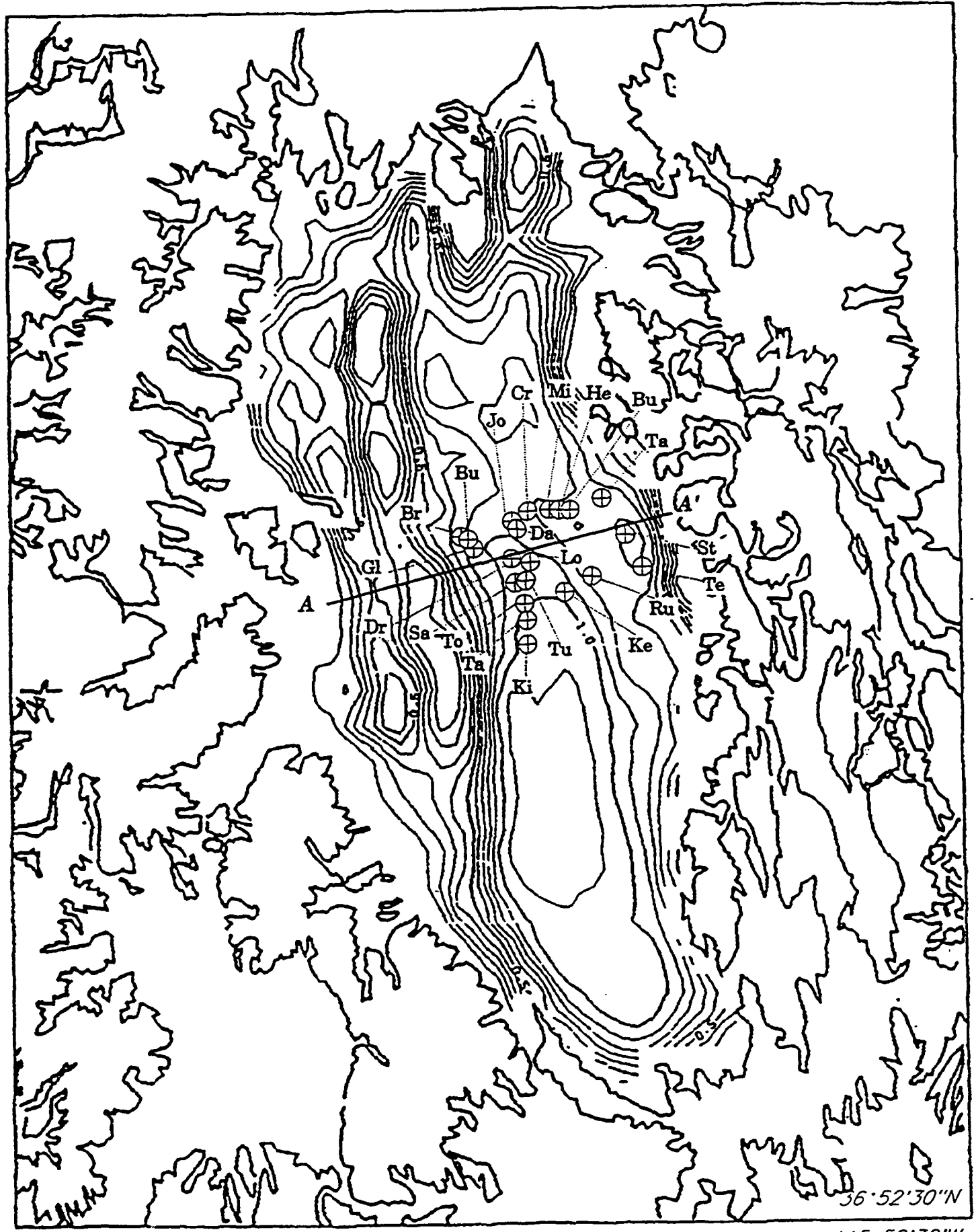


West

0 1 2 3 4 5 6 7 8 9 10 11 12 13 14 15 16 17 18 19 20

East

Figure 2
37°15'N



116°15'W

36°52'30"N

115°52'30"W

Yucca Flat cross-section

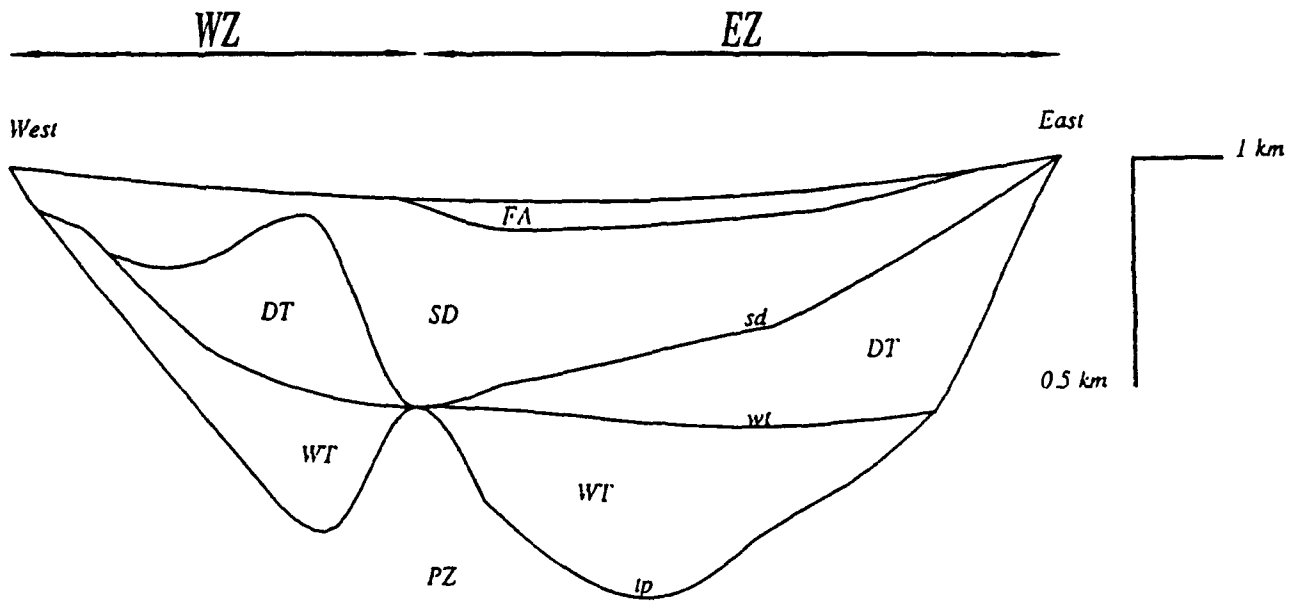


FIGURE 3

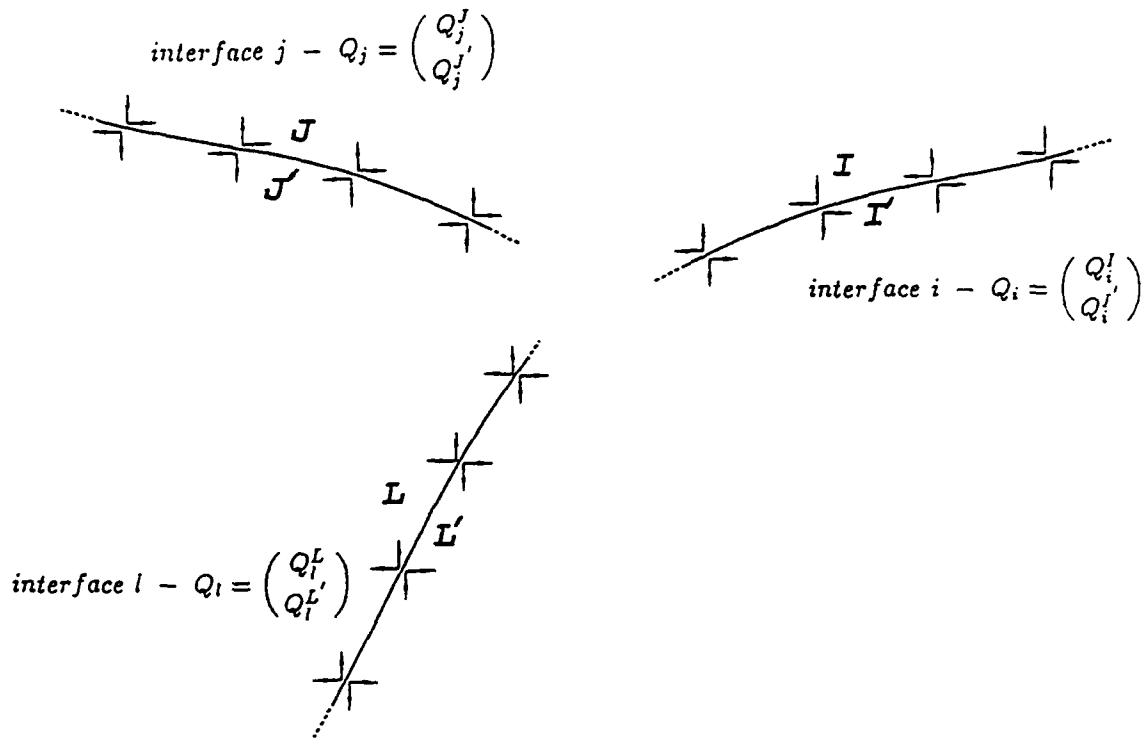


FIGURE 4

Yucca Flat cross-section and events selected

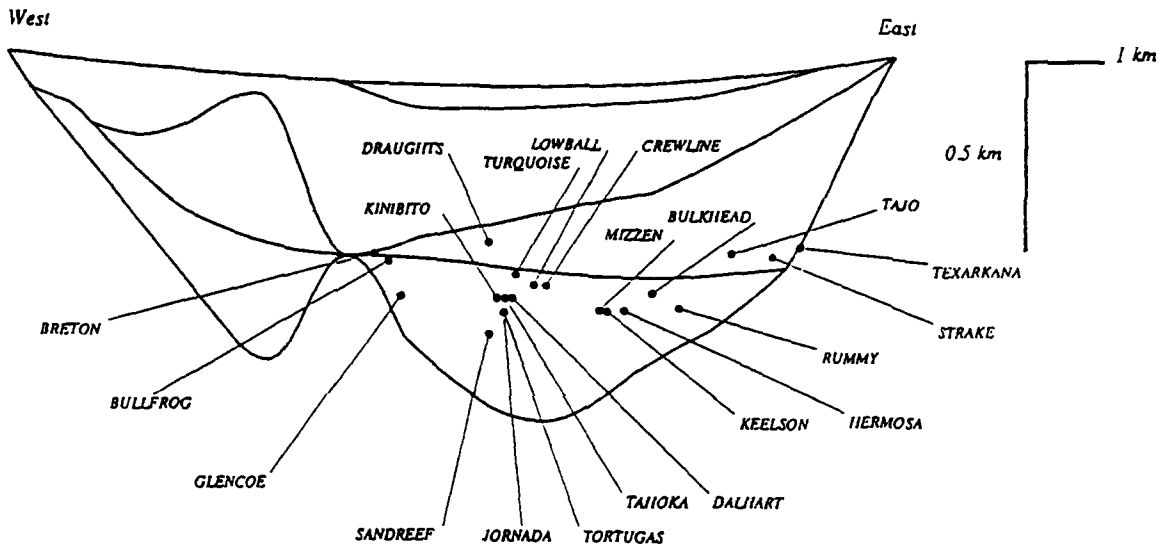


FIGURE 5

Yucca Flat amplitude anomalies

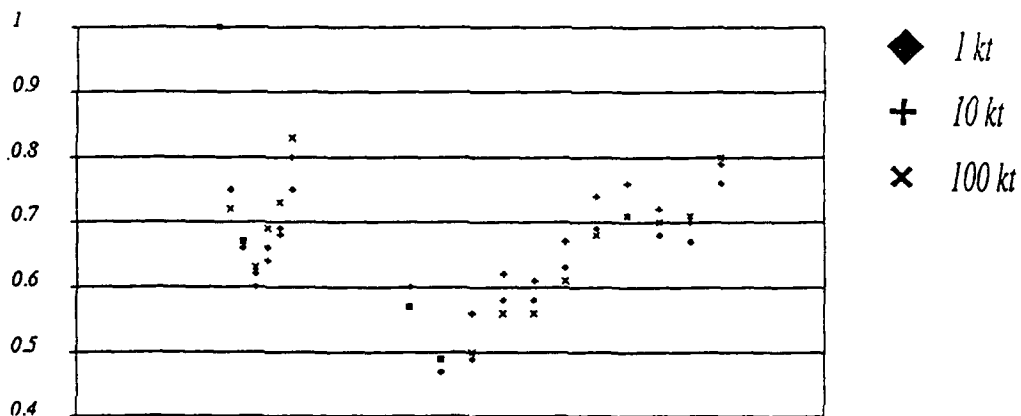
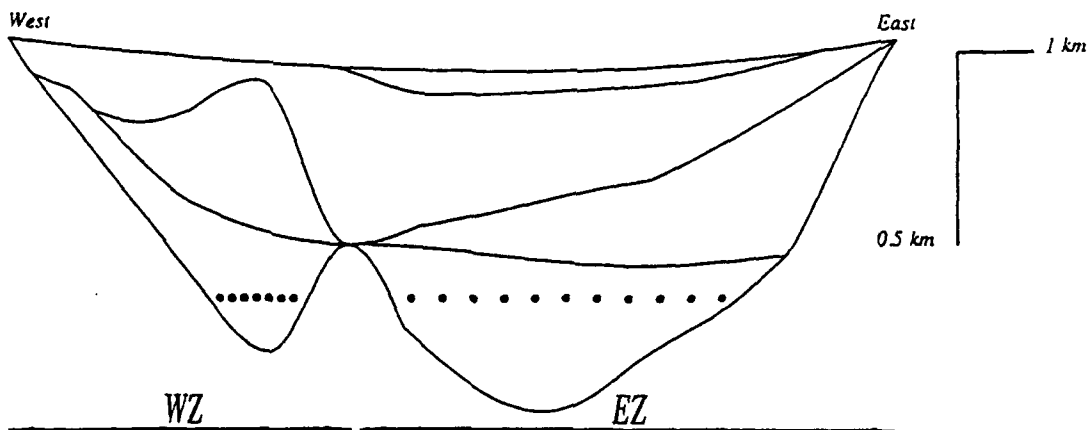
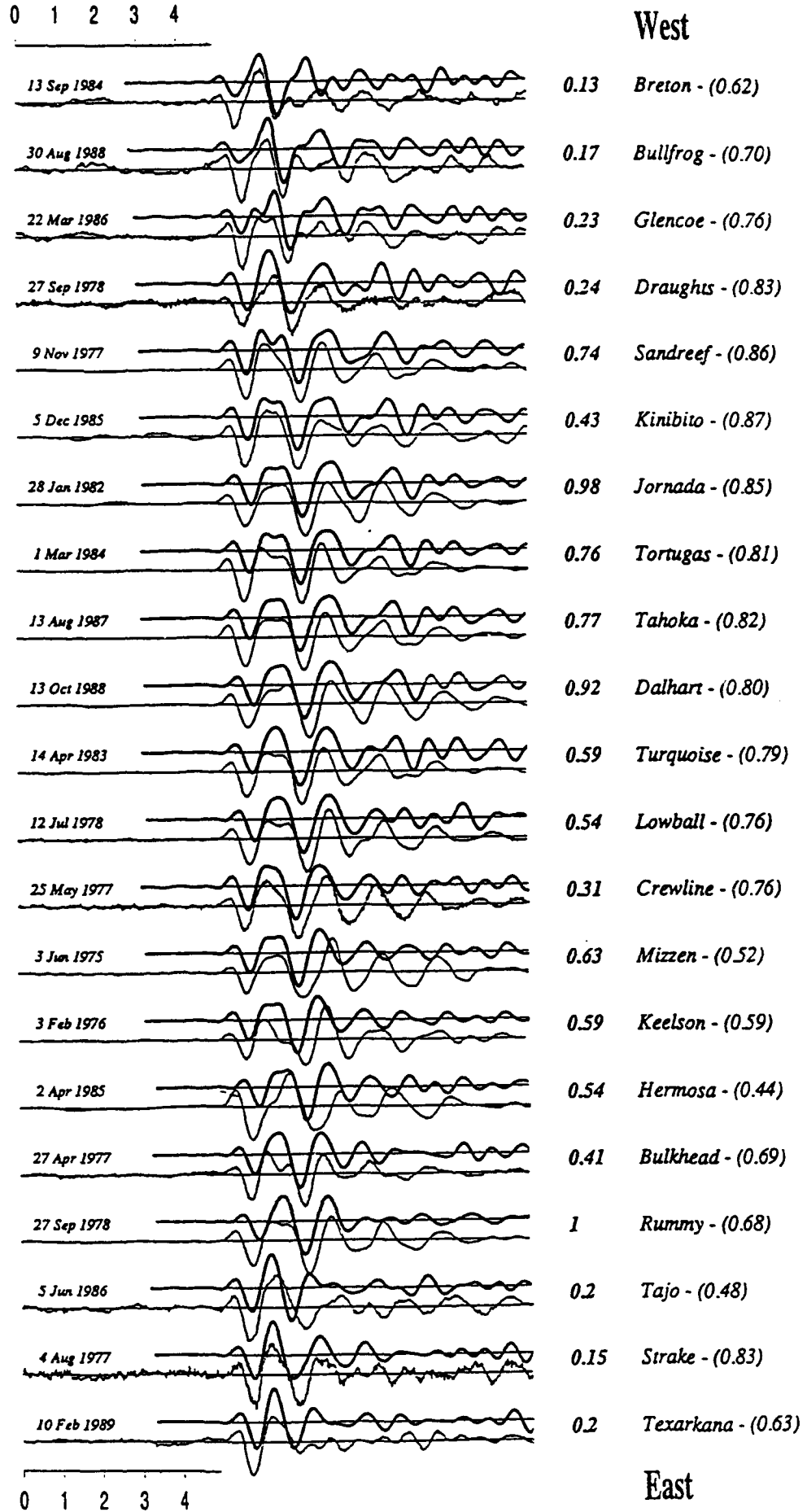


FIGURE 6

FIGURE 7

Radial component



Modeling of French nuclear tests in Taourirt Tan Afella massif, Hoggar , Sahara

S. Gaffet ¹, B. Massinon ², J.L. Plantet ², and Y. Cansi ²

¹ Institut de Géodynamique - 250, rue Albert Einstein - Sophia-Antipolis 1 - 06560 Valbonne - France

² Laboratoire de Détection et de Géophysique - B.P. 12 - 91680 Bruyères-le-Châtel - France

SUMMARY

The influence of the topography on the shape and amplitude of seismograms recorded at short distances is investigated for a set of nuclear explosions detonated in the Taourirt tan Afella mountain, Hoggar, Sahara, mountain where was located the French nuclear test site during 1960's. The wavefield observed in one side in comparison to the other side of mountain show a phase generated with a strong amplitude by reflection of the direct field inside of the mountain. This phase is back-diffracted and can be seen in North azimuth and not in South azimuth. The existence of such a phase is correlated to the source location inside of the mountain. The amplitudes are also modified by the topography with a variation of 25% between observations made in the North and in the South azimuths.

Key words: nuclear explosion, numerical modeling, site effect

1 INTRODUCTION

The French nuclear test site used at the beginning of 1960's was located in the Hoggar massif (Figure 1), 4 km west from In Eker, and 150 km North from Tamanrasset in South of Algeria. The test site is located in a granitic massif, the Taourirt tan Afella (5°2'E; 24°3'N), which is intruded in two gneiss series. (Fauré, 1972; Boullier and Bertrand, 1981). The massif is intrusive in the west side of a 1km thick mylonitic corridor (Figure 2, from Faure, 1972). This corridor, approximately oriented North-South separates the In Eker gneiss serie (west side) and the Tefedest gneiss serie (east side). Both series present a North-South schistosity. The massif is embedded in a thin level of sand (Figure 3, from Faure, 1972). It presents an ellipsoidal shape, 8km long in the North-South direction and 5.6km large in the east-west direction and culminates at 2000m high over a region with 1000m mean elevation.

The study presented here, corresponds to the first step realized in waveform analysis of the French explosions detonated in 1960's in the Taourirt tan Afella massif, Hoggar, Sahara. This study concerns the influence of the topography onto the ground motions at local distances (*i.e.* from 1km to 30km) in the aim to understand the waveforms observed in the NS and EW azimuths at *BRI* (approximately 2km southwest from the explosions studied), *BRIII* (15km west), *INA* (*i.e.* In Amguel, 30km South), and by the French LDG network (2000km in the North).

2 DATA COLLECTED

13 underground explosions have been detonated inside of the massif between november 1961 and february 1966 (see table below). Three sets of the ground velocities recorded, are displayed figures 4, 5, and 6, which correspond to the explosions *Rubis*, *Opale*, and *Jade* respectively. Only *Rubis* has been recorded at short distance (1.73km) from the source at *BRI*. All explosions have been recorded at distances of around 15km at *BRIII* and 30km at *INA*.

Place for Table 1

The shape of the ground velocity differs greatly between these three explosions. The recordings at *BRIII* and *INA* for *Rubis* show pure *P*-wave and Rayleigh wave. The recordings of *Opale* show a long surface wavetrain onto the horizontal component. The

greatest difference is found for recordings of explosion *Jade*. It presents a very long and strong coda associated to the surface wave at *BR111* and *IN4*. These differences may be explained by different causes, *i.e.* explosion working (spalling, coupling), water saturation in source region (and its evolution between each experiment), surrounding geological structures and topography which induce multipathing and amplification effects.

3 STUDY

Our interest is to understand the ground displacement waveforms at local distances, lower than 30km, in both NS and EW azimuths, and at teleseismic distances at 20°, in relation with the location of the shot inside of the Taourirt tan Afella massif, and with the azimuth of recording. In the aim to realize this objective, the Taourirt tan Afella structure is considered as to be superposition of (i) the topography and (ii) the crustal underground structure as defined by Munier (1982). Assuming linear superposition of both effects, this decomposition is useful to separate effects induced by surficial and by underground heterogeneities.

The results presented below, are relative to topographical effects of Touarirt tan Afella for the NS azimuth. They discuss about the ground displacement modifications induced (i) by the topography and (ii) by the detonation location inside of the mountain. The numerical method used for computation is the discrete wavenumber - boundary integral equation method (Bouchon and Aki, 1977; Gaffet and Bouchon, 1989). The wave propagation velocities are $\alpha = 6\text{km/s}$ and $\beta = \alpha/\sqrt{3}$, and the source time function is a Ricker pulse.

Figure 7 is shown as reference, the ground velocities obtained for an explosion buried at 300m depth under a flat surface. The only waves generated are the direct *P*-wave followed by the Rayleigh wave with a shorter amplitude.

Figure 8, displays the ground velocities obtained when the explosion is at the same depth (*i.e.* 300m), straight under the top of Taourirt tan Afella mountain (configuration is given figure 9). The source pulse is centered at 3Hz. The time duration is 13s and the observations ranges from 21km in South (+ signs) to 30km in North (- signs) directions. Distances and relatives amplitudes are written for each H and Z velocity components. Besides the direct field (line P, Figure 8) which is followed by a Rayleigh wave (R1) with a strong amplitude on both side of the mountain, two other branches appear which propagate with a delay of 1.7s in the North direction. These two phases are (i) reflexion inside of the massif of the direct *P*-wave (RD) and (ii) a second Rayleigh wavetrain (R2) generated by the interaction between the reflected *P*-wave inside of the irregular topography. In South azimuth a phase (S) propagates with the *S*-wave velocity. It is vertically polarized and is observed at the front of the Rayleigh wave branche (R1). This phase is a *S* surface wave generated in the flat zone of the massif. The maximum amplitudes computed in North direction are 60% the one obtained in the South.

Figure 10 shows a comparison between horizontal (H) and vertical (Z) ground velocities obtained at 20km North and South from the source in the configuration shown figure 9. Three observations can be made using this explosion location configuration. (i) The amplitude of the vertical component is significantly modified by the topography while the horizontal one is not, (ii) the shape and amplitude of the direct *P*-wave are not affected by the topography, and (iii) the amplitude and shape of the diffracted field (*i.e.* Rayleigh wave and secondary phases) of both horizontal and vertical components are different.

We now study the influence of the location onto the ground velocity when an explosion is detonated in South (explosion A, figure 11) and in North (explosion B, figure 12) inside of the mountain. Explosions A and B are supposed to be buried 300m depth normal to surface topography. The distances of observation is approximately 15km South and North from the source. The pulse source is centered at 4Hz, and the seismograms are computed

for a time window of 7.8s (Figure 13). The relative amplitude and the horizontal offset is written in the right side of each component. The diffracted field, i.e. mainly composed by the phases noted (S), (R1), (R2), has a higher frequency content for explosion A than for explosion B. This is observed for all ground velocity components on both sides of the massif. This observation may be related to the lower elevation of the mountain in the explosion A zone. The phase (R2) is well observed for the two explosions on the AzS and BzN components while the surface S -wave appears on the AzN and BzS components. This behaviour is coherent with the observation previously made, figure 8. We notice the phase delay of the (R1) phase on BhS component.

Thus, the different phases are symmetrically observed for explosions A and B. But as for it, the frequency contents of the diffracted fields are significantly different, between explosion A and B, as well as the relative amplitude of the different components.

4 CONCLUSION

We realize here the first step of a global seismological study of Saharian explosions. The preliminary results show the great influence of the topography onto the ground velocity recorded in the frequency band between 1 to 4Hz, at distances from 1 to 30km far from explosions detonated inside of the granitic massif of the Taourirt tan Afella, Hoggar, Sahara.

The general result is that, alone the topography strongly shapes the ground velocities and their amplitudes. This result encourages us to enter the second step of the study concerning the underground basaltic and mohorovicic structures, associated to the lateral variations of the medium, such as the NS mylonitic corridor, in the aim to get a complete explanation of the waveform recorded.

Yet, the main results are the following ones. The back scattered wave shapes very strongly the seismograms. The surface wave appears to be generated after reflexion of the direct field onto the opposit side of the massif. The back scattered field is made up of both P -surface wave and Rayleigh wave which simply duplicate the direct corresponding fields. We show that for a receiver located at the same epicentral distance, the amplitude of the vertical ground velocity may vary with a factor of 2, from one side to the other side of the massif. We show that the duration of the surface wavetrain is strongly enlarged depending on the side (the azimuth) of observation.

REFERENCES

- Bouchon, M. and K. Aki 1977. Discrete wavenumber representation of seismic source wave fields. *Bull. Seism. Soc. Am.*, **67** , 259-277
- Duclaux, F. and L. Michaud 1970. Conditions expérimentales des tirs nucléaires souterrains français, 1961-1966. *C. R. Acad. Sc. Paris*, **270** , 189-192
- Boullier, A.-M. and J.-M. Bertrand 1981. Tectonique tangentielle profonde et couloirs mylonitiques dans le Hoggar central polycyclique (Algérie). *Bull. Soc. géol. France*, **XXXIII** , 17-22
- Faure, J. 1972. Recherche sur les effets géologiques d'explosions nucléaires souterraines dans un massif de granite Saharien. *Report CEA-R-4257* , 273pp
- Gaffet S. and M. Bouchon 1989. Effects of two-dimensional topographies using the discrete wavenumber - boundary integral equation method in \bar{P} - \bar{SV} cases. *J. Acoust. Soc. Am.*, **85** , 2277-2283
- Munier, G. 1982. Construction d'un modèle de croûte sous le Hoggar Central. *Report CEA/LDG 53-82*
- Rocard, Y. 1964. Formation du signal séismique lors d'une explosion souterraine. *C. R. Acad. Sc. Paris*, **258** , 2373-2375

FIGURE CAPTIONS

Figure 1 : Map of North Africa. The gray filled circle indicates the location of the French nuclear test site in Algeria, during 1960's.

Figure 2 : This map, from Faure (1972), illustrates the geological formation located around the Taourirt tan Afella test site.

Figure 3 : Topographical section in North-South azimuth across Taourirt tan Afella massif, from Faure (1972).

Figure 4 : Seismograms recorded during *Rubis* experiment, at *BRI*, *BRIII*, and *INA*. The time scale is repeated with different shape for each trace.

Figure 5 : Seismograms recorded during *Opale* experiment, at *BRIII* and *INA*.

Figure 6 : Seismograms recorded during *Jade* experiment, at *BRIII* and *INA*.

Figure 7 : Horizontal (H) and vertical (Z) components of the ground velocity computed for an explosion buried 300 m depth under a flat surface in a homogeneous space. The source is a Ricker pulse centered at 3.5 Hz. The time window is 7.8 s. Receivers are identified by their epicentral distances (from -18 km to +18 km).

Figure 8 : Horizontal (H) and vertical (Z) seismograms computed in the configuration described figure 9. The time duration is 13 s. The source is an explosion with a pulse time function centered at 3 Hz. The epicentral distances of the receivers are from +21 km in the South to -30 km in the North. The relative amplitude are written above the epicentral distances. The notation used to highlight the different phases are discussed in the text.

Figure 9 : Geometrical configuration used to compute the seismograms presented figure 8. The *P* and *S* wavelength are illustrated above the topography.

Figure 10 : Comparison of ground velocity computed at an epicentral distance of 20 km for each side of the mountain. See text for explanation.

Figure 11 : Geometrical configuration used for the explosion A.

Figure 12 : Geometrical configuration used for the explosion B.

Figure 13 : Comparison of the horizontal and vertical components of the ground velocity for the explosion A (left side) and for explosion B (right side). For explosion A, the two receivers are 14.9 km far in the South and in the North from explosion location. For explosion B, the two receivers have an offset of 15.5 km in the North and in the South azimuths from explosion. The different components are noted as follow in the text, *AB hz NS*. The first letter refers to the explosion (A or B), the second letter refers to the component (H or Z), and the third letter refers to the azimuth of observation (South or North).

TABLE 1 - French explosions characteristics

Explosion	Date	Time	TU	Lon E	Lat N	m_b
Agate	11/7/1961	11h 29mn	59.931s	5° 3' 7.6"	24° 3' 25.5"	
Beryl	5/1/1962	10h 00mn	0.458s	5° 2' 30.8"	24° 3' 46.8"	
Emeraude	3/18/1963	10h 02mn	0.351s	5° 3' 7.9"	24° 2' 28.9"	
Amethyste	3/30/1963	9h 59mn	0.328s	5° 3' 25.2"	24° 2' 36.0"	
Rubis	10/20/1963	13h 00mn	0.011s	5° 2' 19.0"	24° 2' 7.8"	5.6 (USGS)
Opale	2/14/1964	11h 00mn	0.347s	5° 3' 8.6"	24° 3' 13.1"	
Topaze	6/15/1964	13h 40mn	0.367s	5° 2' 4.4"	24° 3' 59.8"	
Turquoise	11/28/1964	10h 30mn	0.035s	5° 2' 30.1"	24° 2' 30.7"	
Saphir	2/27/1965	11h 30mn	0.039s	5° 1' 52.3"	24° 3' 31.4"	5.8 (USGS)
Jade	5/30/1965	11h 00mn	0.037s	5° 3' 3.1"	24° 3' 18.0"	
Corindon	10/1/1965	10h 00mn	0.043s	5° 2' 2.6"	24° 3' 53.7"	
Tourmaline	12/1/1965	10h 30mn	0.088s	5° 2' 48.9"	24° 2' 37.4"	5.1 (USGS)
Grenat	2/16/1966	11h 00mn	0.035s	5° 2' 28.4"	24° 2' 39.0"	

Figure 1

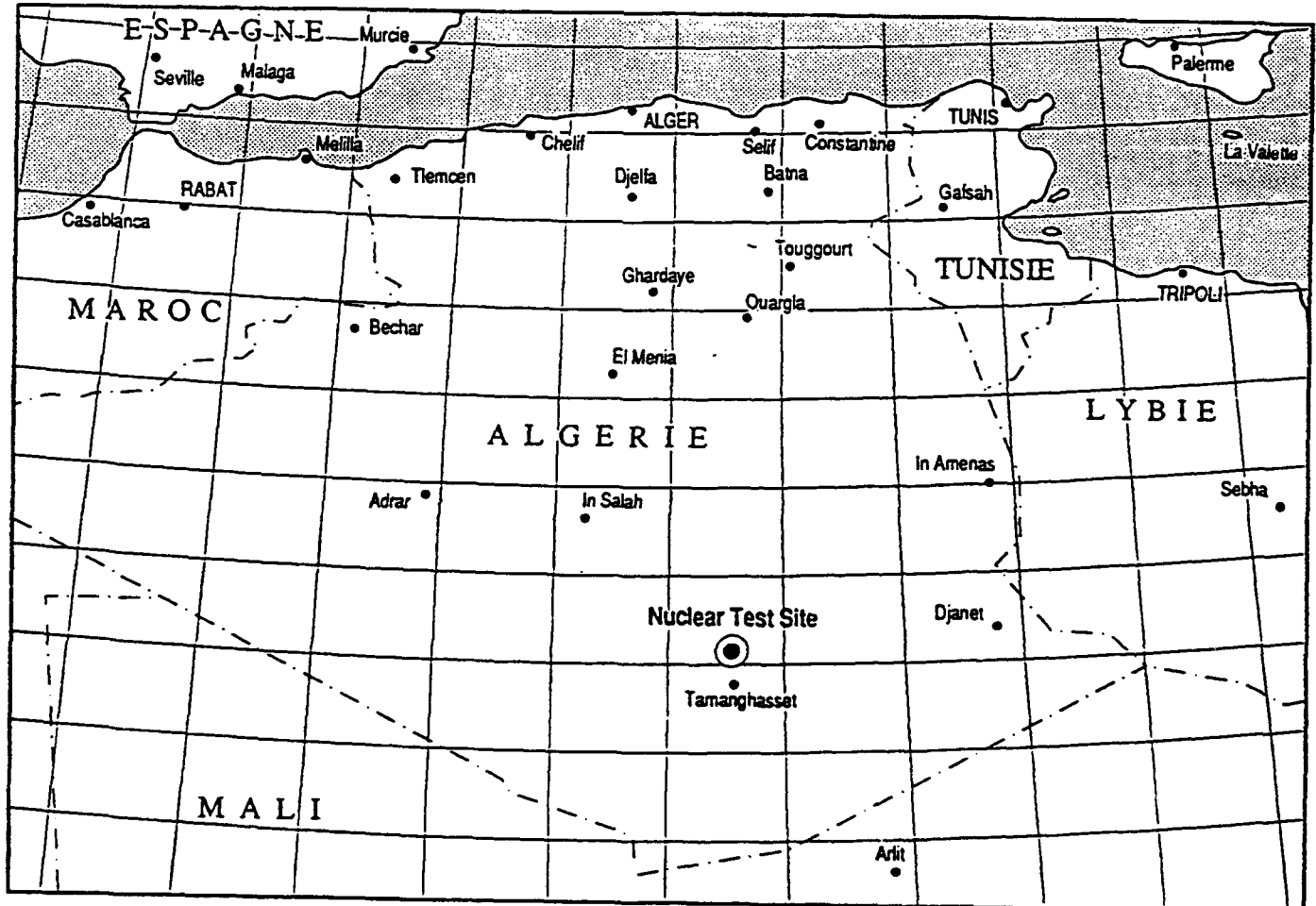


FIGURE 2

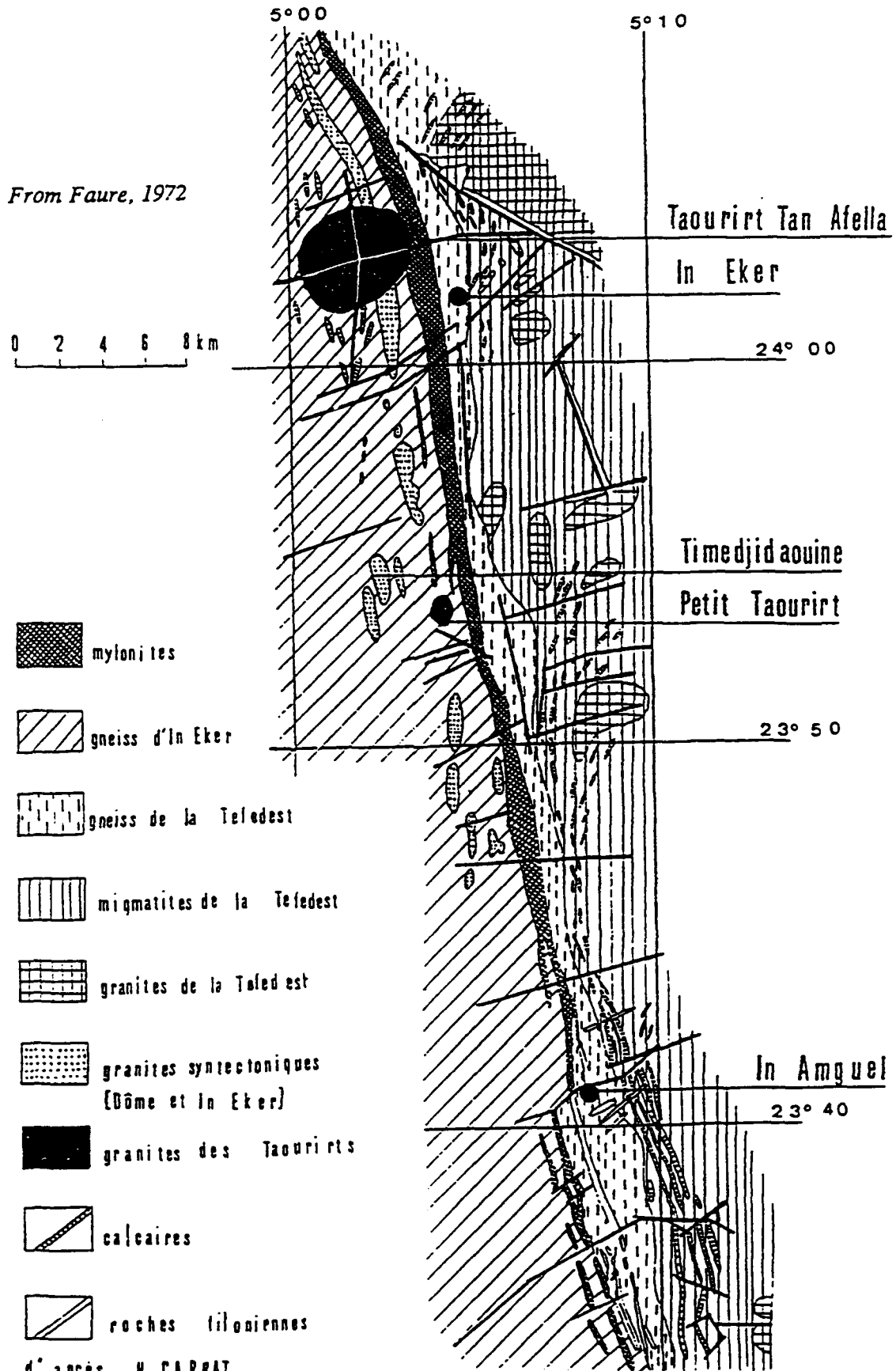
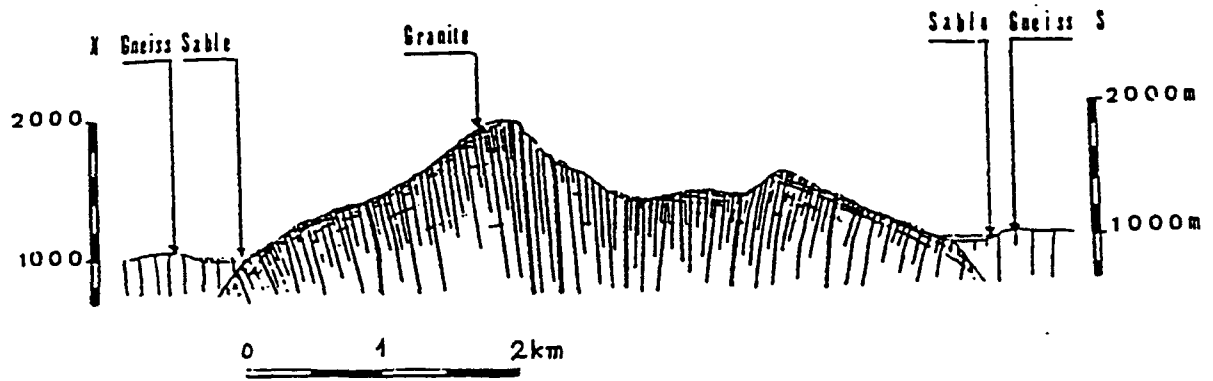


FIGURE 3



From Faure, 1972

FIGURE 4

RUBIS (10/20/1963)

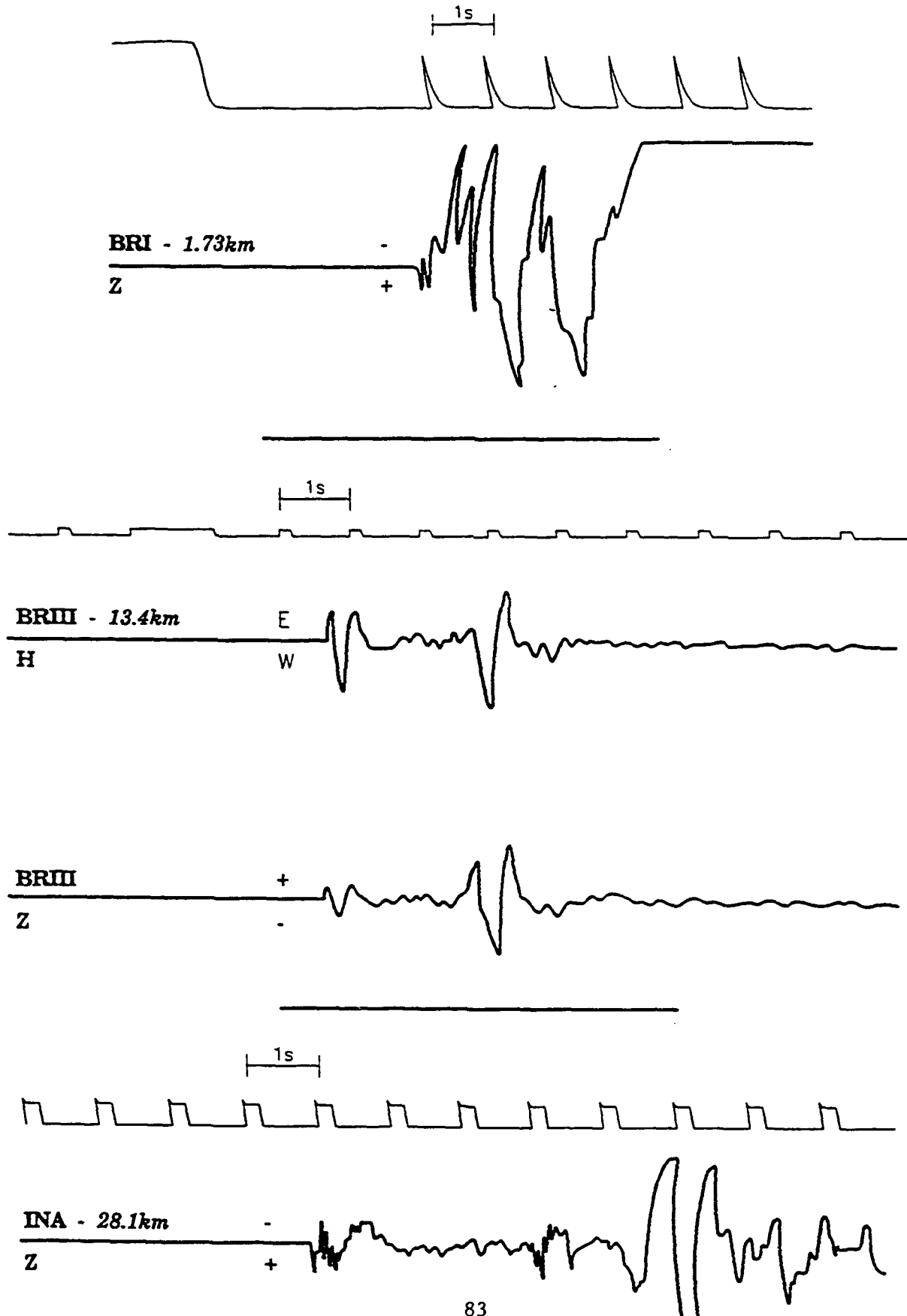
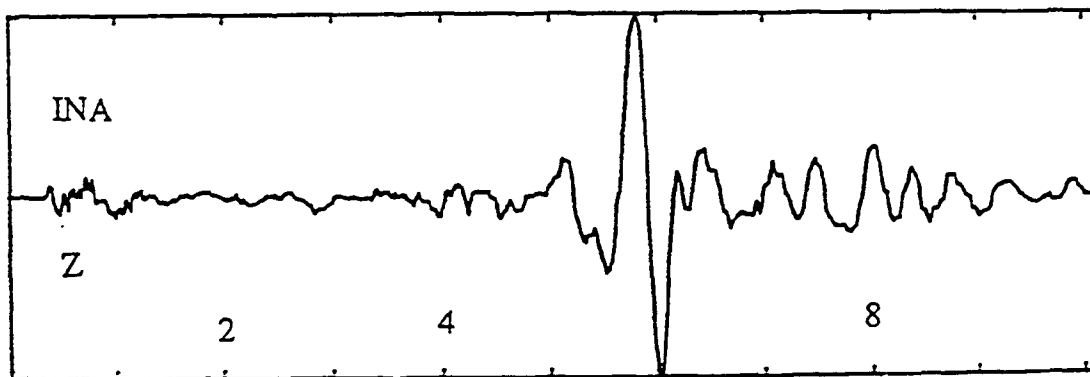
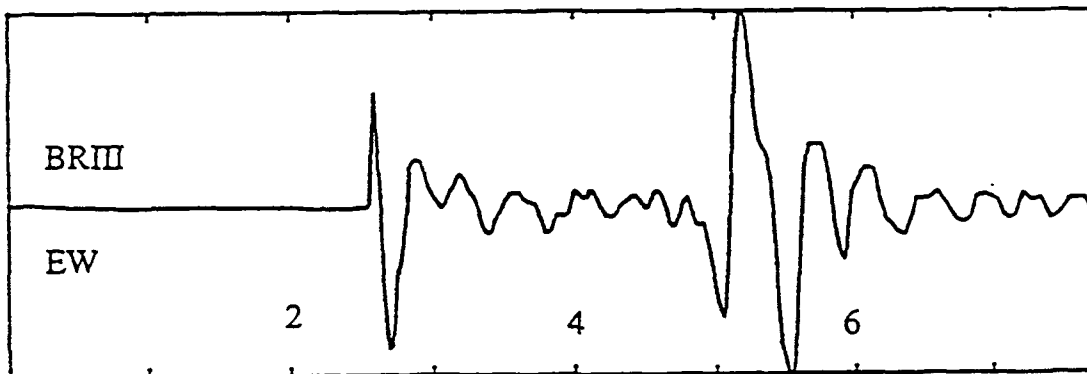
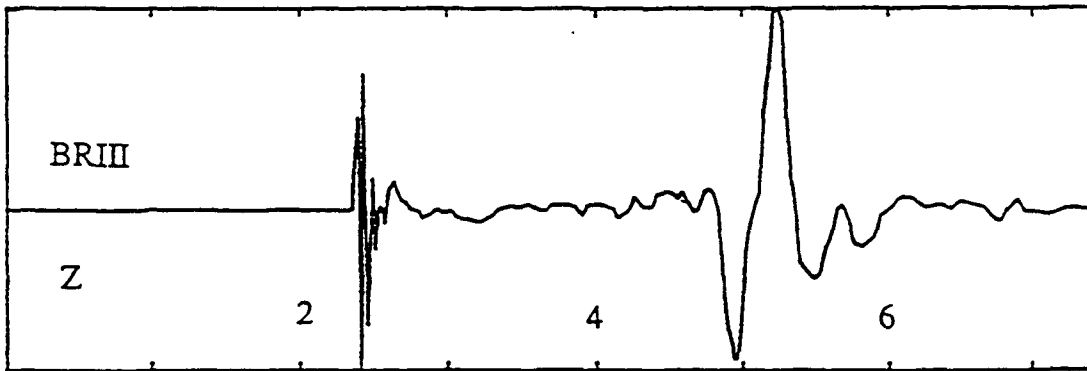


FIGURE 5

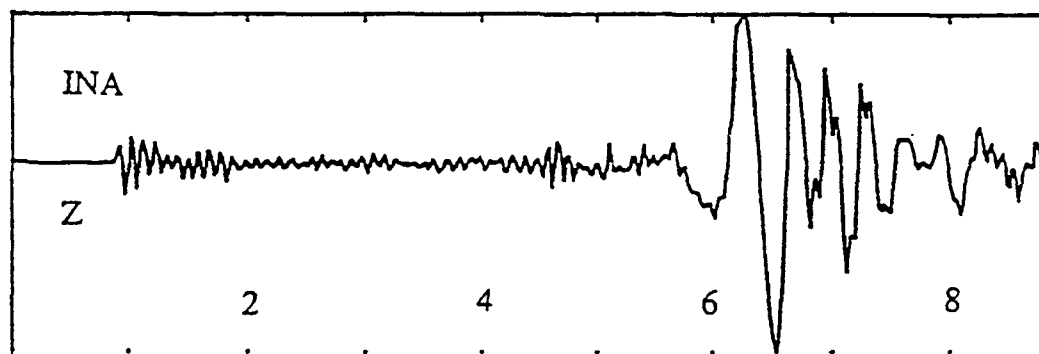
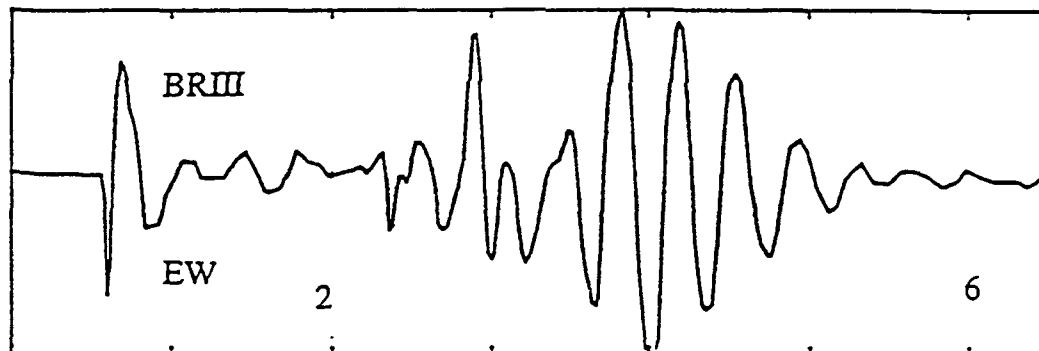
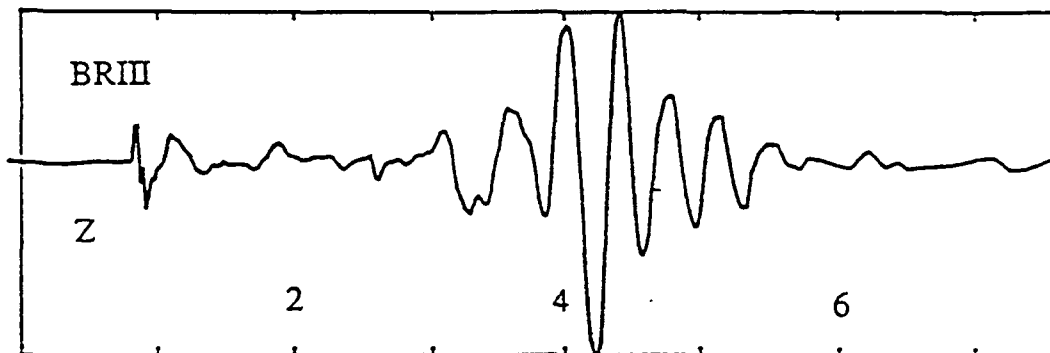
OPALE (2/14/1964)



Seconds

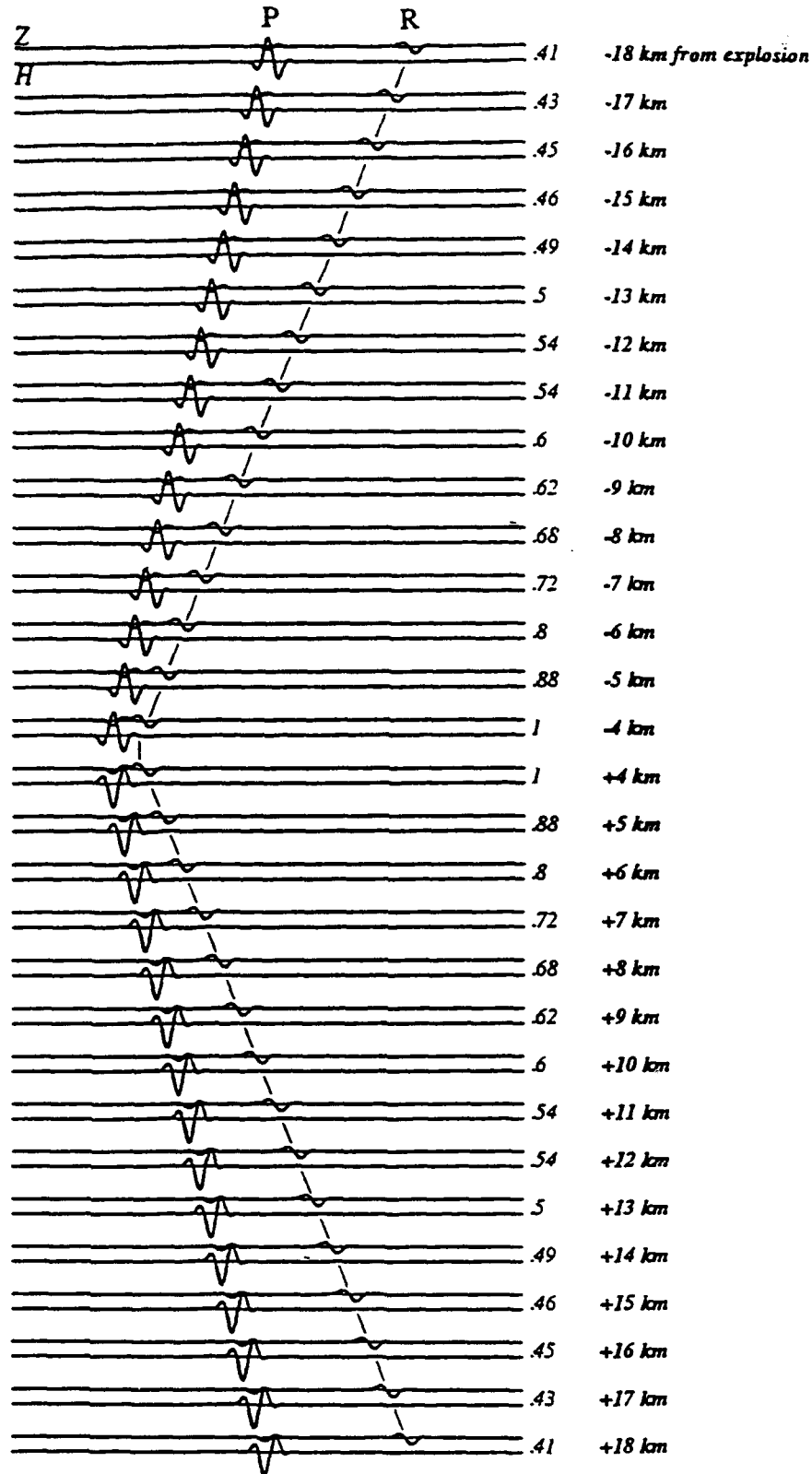
FIGURE 6

JADE (5/30/1965)



Seconds

Figure 7



$\lambda_a = 1.71 \text{ km}$

$\lambda_2 = 1 \text{ km}$



+ 300 m depth

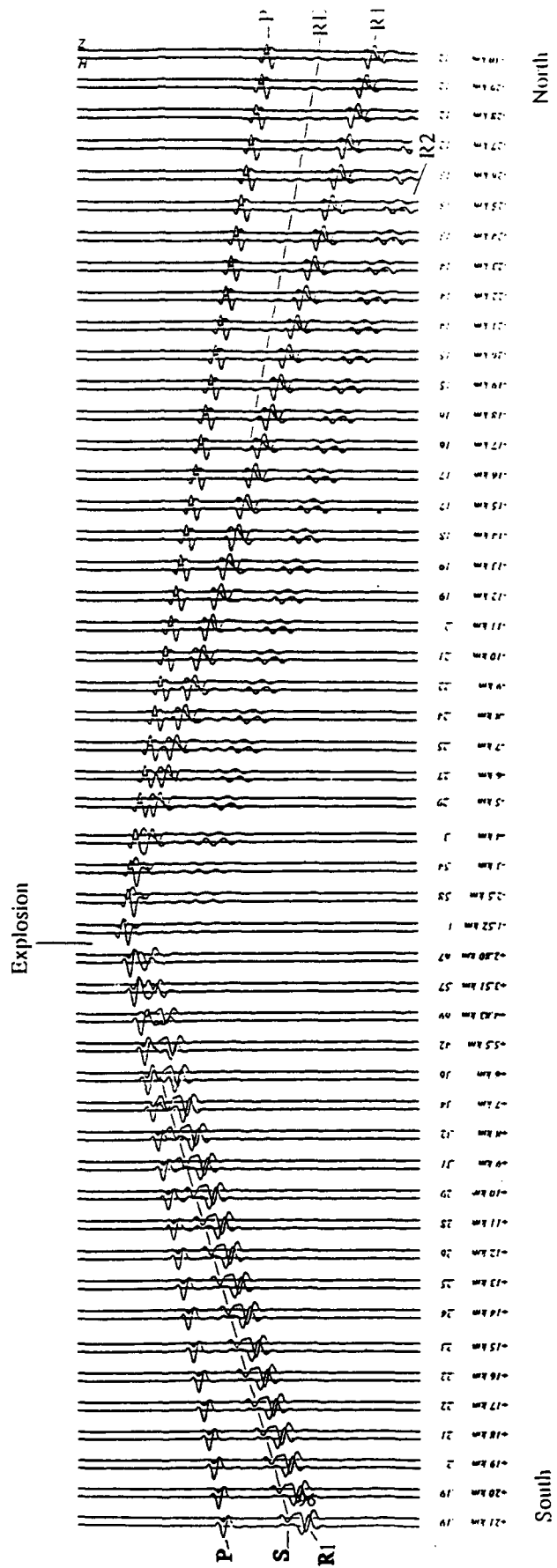
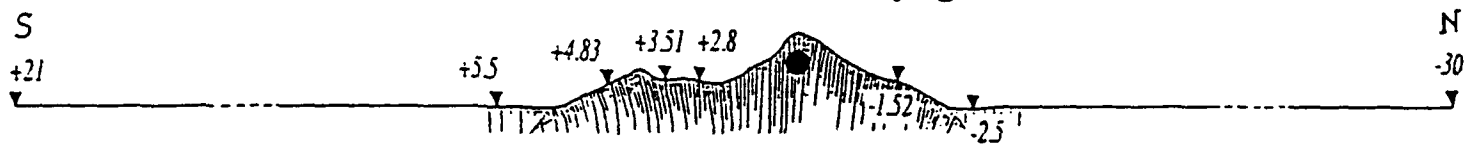
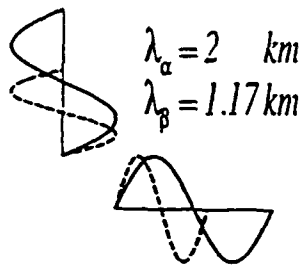


FIGURE 8

FIGURE 9

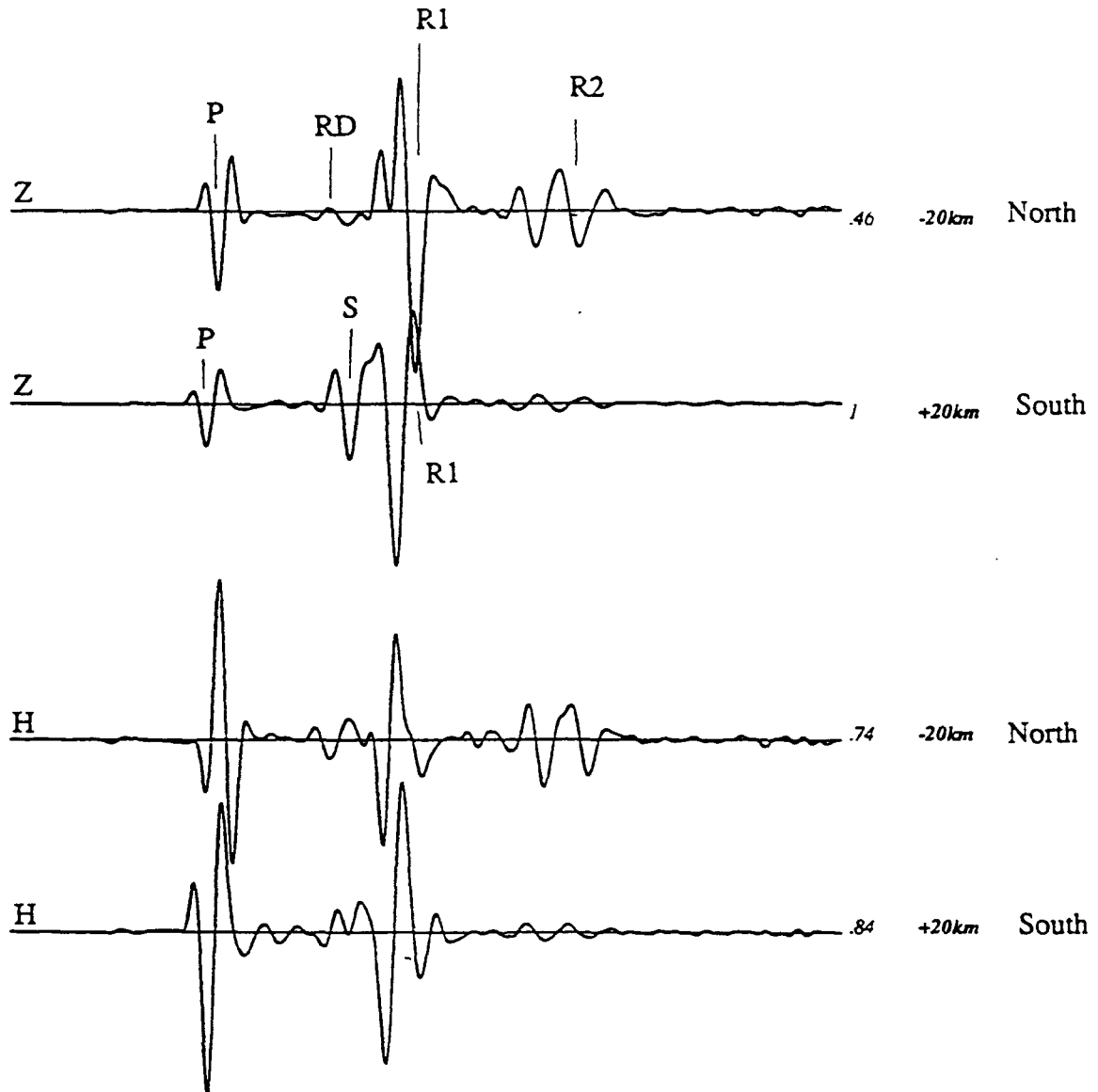
α velocity: 6.0 km/s - β velocity: 3.5 km/s.
Periodicity: 100 km
Explosion at 400 m depth under top of mountain



Ground velocity for a pulse source centered at 3 Hz - Time window: 13 s

FIGURE 10

Ground velocity for a pulse source centered at 3 Hz - Time window: 13 s



Horizontal (H) and vertical (V) components at 20 km from mountain

$$\lambda_{\alpha} = 1.5 \text{ km}$$

$$\lambda_{\beta} = .88 \text{ km}$$

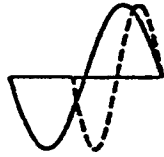
α velocity: 6.0 km/s - β velocity: 3.5 km/s.
 Periodicity: 70 km
 Explosion at 300 m depth normal to surface



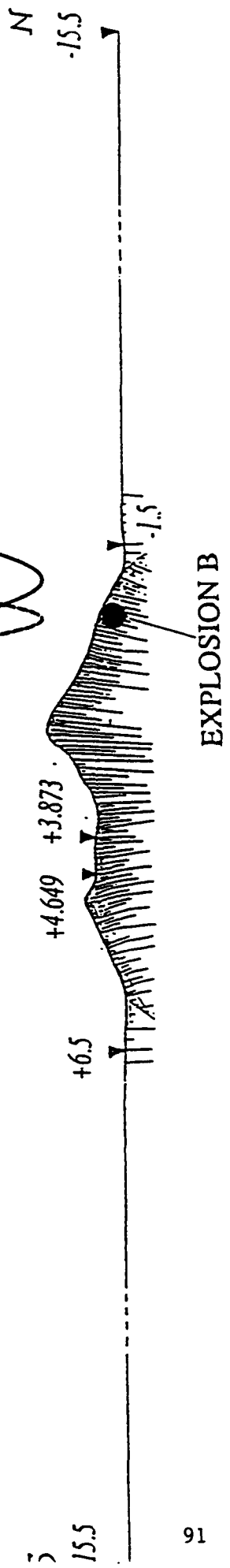
Ground velocity for a pulse source centered at 4 Hz - Time window: 7.8 s

FIGURE 11

$\lambda_\alpha = 1.5 \text{ km}$
 $\lambda_\beta = .88 \text{ km}$



α velocity: 6.0 km/s - β velocity: 3.5 km/s.
 Periodicity: 70 km
 Explosion at 300 m depth normal to surface



Ground velocity for a pulse source centered at 4 Hz - Time window: 7.8 s

FIGURE 12

Ground velocity for a pulse source centered at 4 Hz - Time window: 7.8 s

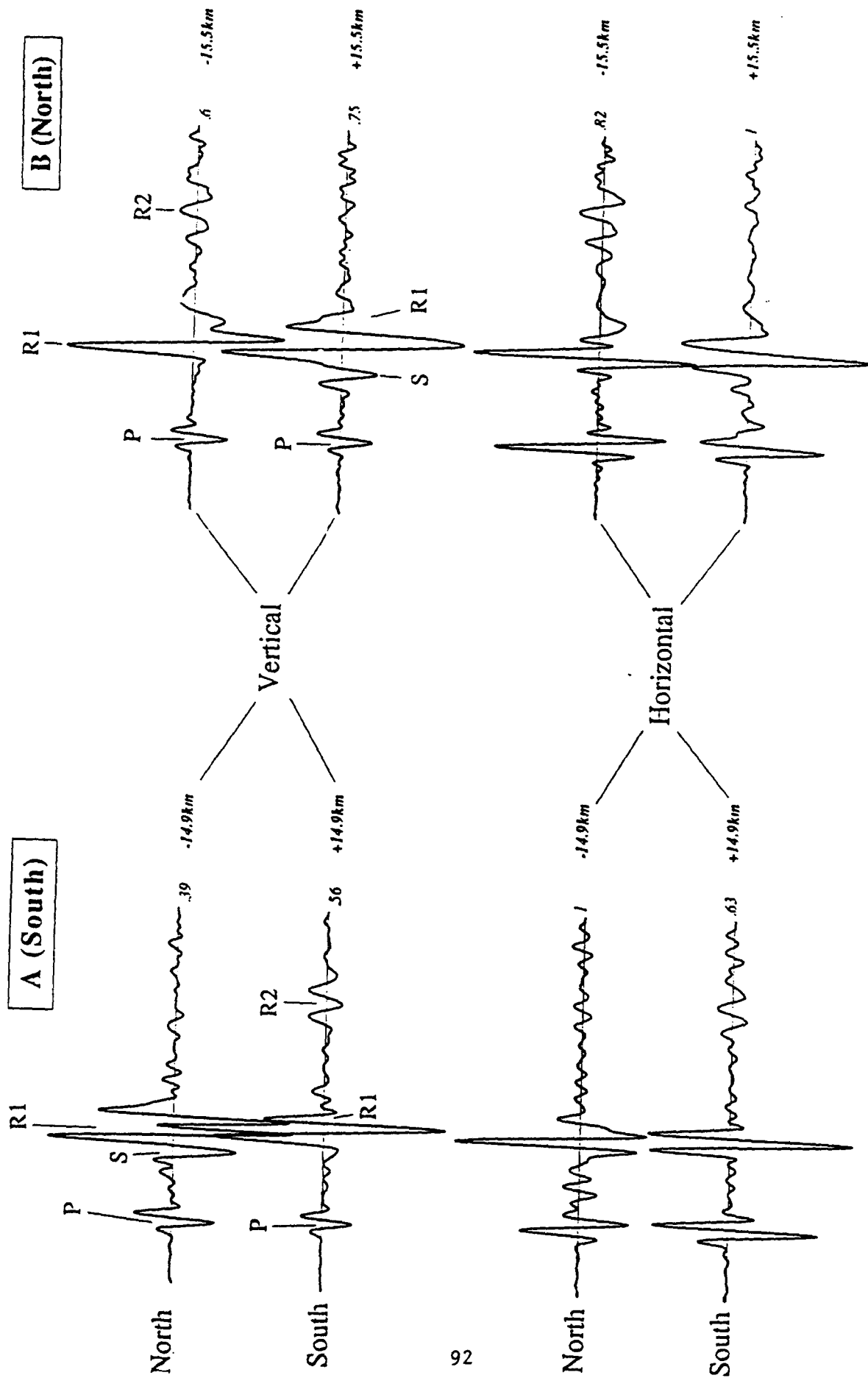


FIGURE 13

Horizontal (H) and vertical (V) components

The massif is embedded in a thin level of sand. It presents an ellipsoidal shape, 8 km long in the north-south direction and 5.6km large in the east-west direction and culminates at 2000 m high over a region with 1000 m mean elevation.

The study we have carried out corresponds to the first step in wave form analysis of the French explosions detonated in 1960's in the Taouarirt tan Afella Massif, Hoggar, Sahara.

The study is composed of two parts :

First it concerns the influence of topography onto the ground motions at local distances (i.e. from 1km to 30km) and at teleseismic distances (2000km). Second, it concerns the influence of the underground crustal structures at the same distances.

Both steps have been proceeded in the aim to understand the waveforms observed in the NS and EW azimuths at station BRI (approximately 2km Southwest from the explosions), BRIII (15 km west), INA (i.e. In Amguel, 30 km south), and by the French LDG network located 2000km to the North.

The preliminary results show the large influence of the topography onto the ground velocity which was recorded in the frequency band between 1 and 4 Hz, at distances from 1 to 30 km far from explosions detonated inside the granitic massif.

The general result is that the topography alone strongly shapes the ground velocities and their amplitudes. this results encourages us to enter the second step of the study concerning the underground basaltic and Mohorovicic structures, associated to the lateral variations of the medium, such as the NS mylonitic corridor, in the aim to get a comprehensive explanation of the recorded waveform.

The main results are the following :

- The back scattered wave shapes very strongly the seismograms. The surface wave appears to be generated after reflexion of the direct field onto the opposite side of the massif. The back scattered field is made of both P-surface wave and Rayleigh wave which simply duplicate the direct corresponding fields.

- We show that for a receiver located at the same epicentral distance, the amplitude of the vertical ground velocity may vary with a factor of 2, from one side to the other side of the massif.

III - Data processings associated with a mini-array recently built in the Center of France :

III - 1 Detection and phase identification capabilities :

During the 80's, substantial efforts have been carried out to use local mini-arrays for automatic event detection (e.g. : Mikkelveit et al., 1983). Beside these studies, some researches have also been undertaken to evaluate their capabilities of automatic azimuth and slowness determination, for location purpose.

For similar objectives, the French Laboratoire de Détection et de Géophysique (LDG) has installed in 1990 a small temporary local network in the Center of France, provisory composed of 5 vertical component short period seismometers with an aperture of 1.2 km (In the next future 10 stations would be set up). Ninety eight (98) teleseismic events have been recorded by the network during 6 months of operation. We present here the main result concerning the automatic determination of azimuth and slowness for each event of this dataset. Two different methods of data processing are tested and compared for that purpose.

1) *The methods :*

- The first method, so-called "*frequency-wavenumber (f-k) method*", has often been used by seismologists (e.g. : Capon, 1969, Gupta et al., 1990). At the opposite of the original use of this method which computes the K-spectrum using filtered signals in a narrow band, we have followed the algorithm proposed by Nawab et al., (1985), which uses the zero-delay spectrum to obtain a k-spectrum containing information integrated over the whole frequency range. Then the azimuth is evaluated by searching the maximum value of the radial energy of the K-spectrum.

- The second method is just a "*correlation method*". In a first step, the cross-correlation function of the stations taken two by two leads to the determination of arrival-time differences, with an accuracy of one sampling interval (i.e. : 0.02 s in our case). In a second step, the cross-spectrum phase allows to compute the residual arrival-time difference, less than 0.02 s. This residual arrival-time difference is determined by the slope of the phase as a frequency function in the characteristic frequency band of the signals.

Then, assuming a plane wave as a propagation model, these arrival-time differences are used to compute both azimuth and slowness of the wave.

2) *The results :*

We have processed the whole dataset of 98 teleseismic events.

Besides 12 events (given by numbers), the standard deviation of the residuals is 15 degrees, in the 1000-8500 km range. For larger distances, the incident wave being very close to the vertical axis leads to a poor azimuthal determination, as expected.

A similar study has been made with the correlation method, for the determination of azimuth using, first, arrival-time differences obtained from the cross-correlation functions, and secondly, those computed by both cross-correlation functions and cross-spectrum phases. It clearly shows the gain obtained by the use of the cross-spectrum, specially in the 1000-8500 km range. This is again demonstrated by testing the consistency of the arrival-time differences set which must verify the triangular Chasles relation is : $\Delta t_{ij} = \Delta t_{ik} + \Delta t_{kj}$ for all i; j; k. The RMS value of the residuals of the Chasles relation is 0.013 s when we only use arrival-time differences determined by cross-correlation, and 0.002 s in the second case.

Another advantage can be attributed to the "*correlation method*". At the opposite of "*(fk) method*" which assumes a plane wave and model, we can use a more refined model defined by a plane wave and a set of time delays affecting the arrival-times. Using the global dataset, we can statistically compute each station anomaly as the mean value of the residuals. This leads to time delays ranging from -0.008 s to 0.005 s producing time differences greater than half a sampling interval for some couples of stations.

The residual azimuths as a function of the true azimuths obtained from USGS, take into account the station anomalies, clearly shows a cosine dependence which might be explained by a deeping structure of the crust layers below the network. Final results taking into account this cosine dependence within the range of 1000-8500 km, show that the standard deviation becomes less than 10 degrees with only two aberrant points.

We have used a set of 98 teleseismic events recorded by a temporary 5 stations mini-array set up in the Center of France to test two methods for automatic measurement of P-wave azimuth.

The first method, or "*f-k method*", gives as expected consistent results in most of the cases (azimuth determination with an error of 15 degrees and 12 aberrant evaluations).

A second method, the "*correlation method*", derived from the doublets method (Poupinet et al., 1982, Plantet et al.; 1985), uses a step-by-step algorithm, computing first, on set time differences, then uses the cross-spectrum as a vernier to refine these differences. It also allows to introduce station anomalies to correct the propagation model before the azimuth computation. Azimuth is then determined with an error of less than 10 degrees in the 1000-8500 km range with only two aberrant determinations. Consequently, better results are obtained with this method.

Further studies will investigate the regional domain for which the higher frequency content will give a better accuracy in the arrival-time differences.

We suggest such a correlation method to be tested with seismic data recorded in other mini-arrays.

III - 2 Automatic processing of seismic events recorded on a mini-array (signal analysis combined with neural networks) :

We present a new method for automatic processing of seismic events recorded on a 5 - station mini-array located in Central France.

The first step of the process consists in the computation of accurate arrival time differences for each couple of stations using their correlation function. These arrival time differences computed for different time-windows and for different frequency bands allow us to get three time-frequency plots representing the consistency of the time-delay set, the velocity and the azimuth deduced from the location performed with these time-delays. The consistency of the time-delay set is then used as a signal detector.

For teleseismic events, the location is strictly deduced from the velocity and the azimuth and leads to an accuracy of less than 10 degrees for distances lower than 80 degrees.

For regional events, an additional step is needed to identify the different phases. This task is performed by a neural network using as inputs for each time-step the velocities computed on the current part of signal filtered in different frequency bands provided that the consistency of the time-delay set is verified. A multi-layered perceptron then computes the possibility of appearance for each phase as a function of time. The more probable azimuth is determined and used as a filter. Finally, the distance is computed by choosing in propagation tables the best solution according to the possibilities.

EARTHQUAKE LOCATION APPLIED TO A MINI-ARRAY: K-SPECTRUM VERSUS CORRELATION METHOD

Yves Cansi, Jean-Louis Plantet and Bernard Massinon

Laboratoire de Détection et de Géophysique

Abstract. Two different methods devoted to automatic location of both regional and teleseismic events recorded on a mini-array are compared in terms of location accuracy. The first method belongs to the frequency-wavenumber methods family; the second one uses signal processing to compute accurate time-delays and then derive the event parameters. In the latter method a careful study of each time-delay set is performed in order to remove ambiguity errors using Chasles relationship. It leads to an accuracy of about 10 degrees on the azimuth determination for distances smaller than 80 degrees, and 3 degrees for regional distances. Finally, a criterion derived from these relations is proposed for phase detection and identification.

Introduction

During the 80's, many attempts were made to adapt seismic arrays to automatic signal detection and event location. Besides these studies, some research has been conducted in order to evaluate their capabilities of automatic azimuth and slowness determination [e.g.: Mykkeltveit et al., 1990].

In 1989, the 'Laboratoire de Détection et de Géophysique' (LDG) temporarily installed a 5-station small aperture mini-array, which recorded more than 400 seismic events during its 4-month operation period. This dataset has been used to study an automatic location process adapted for both teleseismic and regional events. Two methods were used with a different approach: one belongs to the spectral methods family, the other analyzes directly the time series.

We present the results concerning the automatic determination of azimuth and slowness for two sub-datasets (teleseismic and regional events), using these two different methods, and compare them.

The Data

During the test, the mini-array was mainly composed of 5 short-period vertical component seismometers. Figure 1 shows a map of the mini-array centered on 45.7411°N 2.0133°E. It has an extension of 2.1 km in the north-south direction and 1.3 km in the east-west direction.

The recorded signals were transmitted to station GM5 for numerical recording after a 12-bit digitalization at a rate of 50 samples per second. This structure with a single clock provides an homogeneous digitalization, and allows

comparison of signals recorded by different stations with a high accuracy.

The 106 teleseismic events used for the study are those which have been localized by USGS. The epicentral distance range extends from 9 to 176 degrees, and twenty-eight events have propagated PKP phases. Their magnitudes range from $m_b=4.1$ (at a distance of 10 degrees) to $m_b=6.4$.

The dataset for local and regional events is composed of 30 earthquakes recorded and localized by the national permanent LDG network. Their epicentral distances range from 42 to 1540 km and their magnitude from $M_L=2.2$ to $M_L=5.3$. In this dataset, for 16 events the Pg-phase is the first arrival; for the 14 remaining events, Pn is the first arrival.

The Methods

The first method (denoted by 'k-spectrum Method') belongs to the 'frequency-wavenumber methods' family. The classical formulation of these methods has often been used by seismologists [e.g.: Capon, 1969, Ingate et al., 1985]. It assumes that the propagation of the wave through the mini-array can be modeled by a plane-wave. So it investigates the horizontal wavenumber plane (k_x, k_y) for each frequency, and determines the azimuth and the slowness of the wave from the wavenumber which gives the maximum of energy.

In order to take into account wideband signals (such as signals from local events), we have used the 'Zero-Delay Power Spectrum' as suggested by Gupta et al. [1989]. This method, proposed by Nawab et al. [1985], computes the 'Zero-Delay Covariance Matrix' from the recorded signals, then computes the wavenumber spectrum using the 'Maximum Likelihood Estimator'. For a plane wave with a given velocity, the radial k-spectrum in the wave azimuth is the spectrum of the wave. The estimation of azimuth and slowness is given by the wave number which realizes the

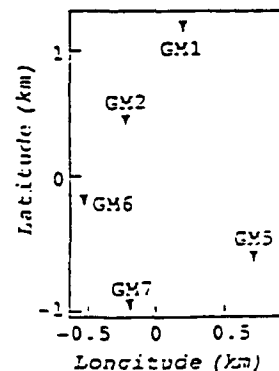


Fig. 1. Mini-array map

maximum of energy. Another estimation of the azimuth can be obtained by searching for the azimuth which gives the maximum of radial energy integrated over the radial wavenumbers. In the following, we refer to these two kinds of azimuth estimation as the 'Maximum of Amplitude' and the 'Maximum of Radial Energy' determinations respectively.

The second method is based on the correlation of the signals. In contrast to the 'k-spectrum Method' which computes the wave parameters by a straightforward process, the 'Correlation Method' acts step by step and computes sequentially the arrival-time differences for each couple of stations, then derives the wave parameters (azimuth and slowness) using a classical location method [e.g.: Husebye, 1969]. This step-by-step algorithm allows us to correct the arrival-time differences for plane wave model anomalies using for example a set of statistically determined station corrections.

The high accuracy measurement of the arrival-time differences Δt_{ij} for each couple of stations is performed in two steps. A rough estimate (step 1) is yielded by the maximum value of the cross-correlation function (maximum accuracy equal to the sampling interval), then a refined one (step 2) which takes into account the frequency content is obtained by the slope of the weighted least-squared fit of the cross-spectrum phase as a function of selected frequencies which have high signal-to-noise ratio. The coherency function is used as the weighting factor. Nevertheless, for teleseismic events, the slope of the fit cannot be determined with a good accuracy because of their narrow frequency-band. To remove this instability, we use the fact that the phase is tending to zero with frequency and solve the least-squared fit only for the slope.

For local events, seismic signals have a higher frequency content, and, consequently, in some cases (specially for small events) the cross-correlation function has not a unique well-defined maximum. Two or more delays might give correlation factors close to one another. This feature is named 'ambiguity'.

To remove the errors induced by this ambiguity, the 'consistency' of the time-delay set is tested. For each set of stations i, j, k , let us introduce the residual r_{ijk} , also denoted Chasles residual:

$$r_{ijk} = \Delta t_{ij} + \Delta t_{jk} + \Delta t_{ki}$$

and the error of each time-delay e_{ij} .

The time-delay set is considered as 'consistent' if the triangular 'Chasles relationship':

$$r_{ijk} = 0$$

holds for all stations i, j, k . If not, we have to find the e_{ij} 's for which:

$$e_{ij} + e_{jk} + e_{ki} = r_{ijk}$$

This system is strongly underdetermined; but we can translate it into an integer-number system of equations by assuming that all these numbers are multiples of the sampling (or oversampling) interval. Furthermore, we are only interested in the largest values of the errors (i.e.: large

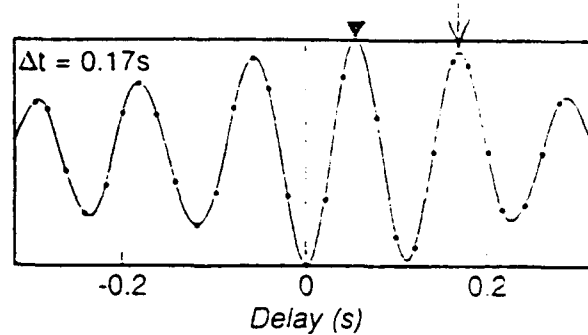


Fig. 2. Example of ambiguity error for a Pn-wave. See text for explanations.

enough to correspond to another maximum of the corresponding correlation function). Using linear programming, we can easily solve this problem, and then use the largest values of e_{ij} to look for a new consistent time-delay set.

Figure 2 shows an example which describes clearly this feature. The cross-correlation function of a Pn-wave is shown, by dots for the original digitization frequency (50 Hz), and by a solid line for an oversampling rate of 8. The triangle shows the maximum of this function, and the arrow the secondary maximum which is compatible with the maxima of the other couples of stations using Chasles relationship. For this event, table 1 shows the results ('RMS Ch': root mean squared of Chasles residuals, ' ΔV ' and ' ΔAz ': velocity and azimuth errors relative to Pn-velocity and to true azimuth respectively) in the two cases: with and without the use of Chasles relationship. It indicates clearly that valuable results are obtained when we use Chasles relationship (even without oversampling).

The Results for Teleseismic Events

The two azimuth estimation methods derived from k-spectrum analysis have been applied to each event.

Figure 3 shows the difficulty of determination of the azimuth using the 'Maximum of Amplitude' determination: the solid curve represents the radial maximum of energy versus azimuth, which is bounded by the k-spectrum value for $k=0$. The dashed one shows the variation of the radial energy versus azimuth. This last determination gives a better precision because of its greater range of amplitude.

The errors of azimuth determinations (i.e.: the differences between the k-spectrum azimuths and azimuths derived from the USGS locations) are plotted versus distance on figure 4. For both kinds of determination (i.e.: 'Maximum of Amplitude' and 'Maximum of Radial Energy'), the azimuth is not available for distances greater than 80 degrees (specially PKP-distances), but for smaller distances the determination is available and the standard deviation is 18 degrees for the 'Maximum of Amplitude'

Table 1

Use of Chales Relationship	Sampling rate (Hz)	RMS Ch (s)	ΔAz ($^{\circ}$)	ΔV (km/s)
no	400	0.062	6.2	1.74
yes	50	0.002	0.0	0.09

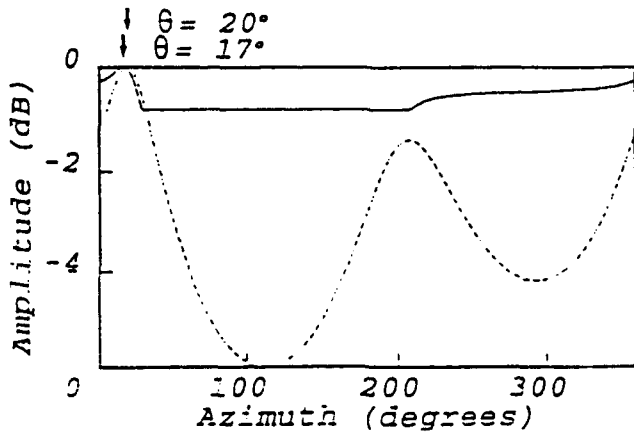


Fig. 3. Variation of radial maximum amplitude (solid line) and radial energy (dashed line) versus azimuth.

determination and 15 degrees for the 'Maximum of Radial Energy' one.

The same dataset has also been processed by the 'Correlation Method'. For each event, the RMS value of the Chasles residuals r_{ijk} is less than 0.003s, which gives an evaluation of the arrival-time differences measurements.

Using the time-delay sets of all the events, we have localized them and then computed station anomalies as the mean values of the residuals. The greatest one (GM7: 0.008s) cannot be neglected compared with the measurement accuracy: 0.003s.

Final results, taken into account the station corrections, are presented in figure 5. The azimuth errors are plotted versus USGS azimuth. It shows clearly a cosine dependence which might be explained by a dipping structure of the crust layers under the mini-array. After removal of this cosine dependence, the standard deviation is reduced to 9 degrees.

The Results for Regional Events

Concerning the regional events, we have only used the 'Correlation Method'. The high frequency content of the signals (specially for the Pn-phase) leads to wavelengths of the order of the size of the mini-array. So, the k-spectrum contains many relative maxima which have amplitudes very close to each other.

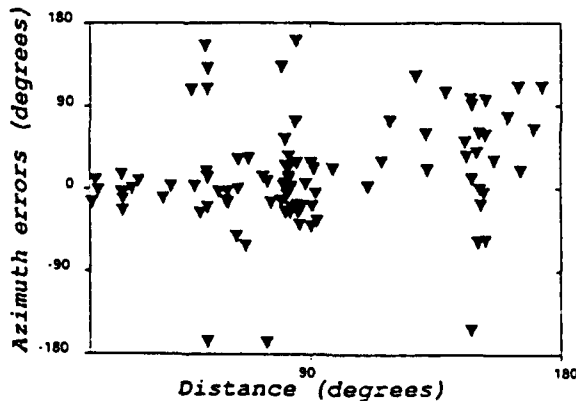


Fig. 4. Azimuth errors (relative to USGS azimuths) as a function of distance, using 'Maximum of Radial Energy'.

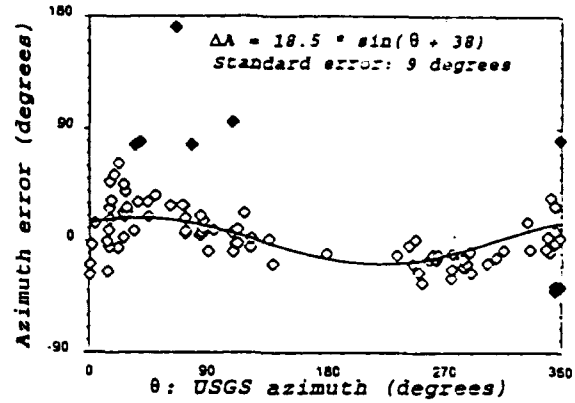


Fig. 5. Final results for teleseisms using 'Correlation Method': azimuth error is plotted versus USGS azimuth. Filled symbols are not used for the computation of cosine dependence.

The results obtained with the 'Correlation Method' are summarized on figure 6, which shows the azimuth errors versus the LDG azimuth taken as the reference. One can see again a small cosine dependence, which might not be significant. The residual standard deviation is in this case 3 degrees.

The 'Correlation Method' used as a Detector

As described above, Chasles relationship is used to test the consistency of the time-delay set. When applied to plane wave signals, the RMS of Chasles residuals is comparable to the measurement accuracy (i.e.: 0.003s).

If we apply this process to the noise recorded on the stations, RMS of Chasles residuals is about 0.01s or more, to be compared to the 0.003s obtained for seismic signals. Consequently, we can use this quantity as a discriminant between seismic signals and noise.

Figure 7 shows an example for a local event. For different frequency-bands, the signals are analysed by using a moving time-window of 2s-width. The plot on the top shows a colored map of the velocity obtained for each position of the time-window (horizontal axis) and of the

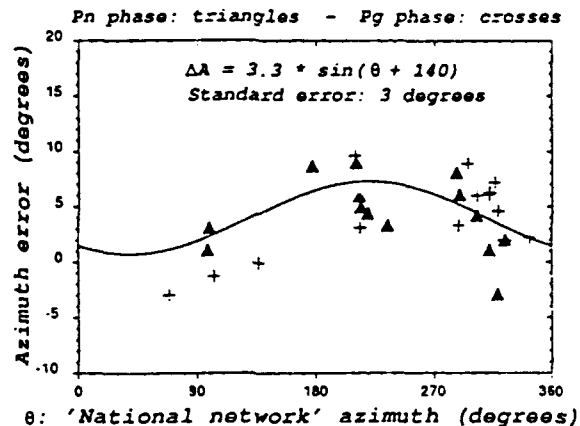


Fig. 6. Final results for regional events using 'Correlation Method': azimuth error is plotted versus LDG azimuth. Filled symbols are not used for the computation of cosine dependence.

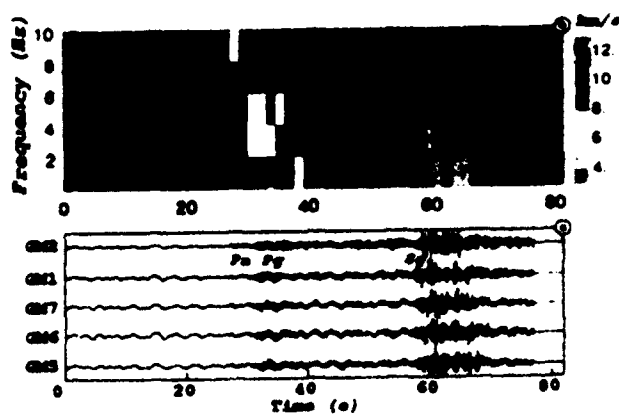


Fig. 7. Example of phase detection and identification by using time-frequency distribution of the velocity computed only for consistent parts of signals (i.e.: Chasles residuals RMS less than 0.009s).

frequency-band (vertical axis). But the velocity color is only present if the RMS of Chasles residuals is less than 0.009s.

It clearly appears that only the time-windows corresponding to the beginning of each phase match this criterion. The influence of the frequency-band is also clearly seen: the Pn-phase is consistent in the high frequency domain, but Lg-phase consistency is limited to low frequencies. Furthermore, the velocity distribution allows a phase identification without any ambiguity.

Conclusions

We have tested two methods devoted to automatic location of both teleseismic and regional events. They are based on a major assumption: the very good correlation of the different records of each event between stations. Moreover, another assumption is needed by the k-spectrum method: it assumes that a plane wave model is valid for all the data.

For teleseisms, using the azimuth determined by the 'Maximum of Radial Energy' of the k-spectrum, the azimuth standard error is about 15 degrees for distances smaller than 80 degrees. On the opposite, no a priori model is needed for the correlation method. This allows us to proceed in two steps: firstly, a rough Δt_i evaluation (correlation), and then a refined one (phase spectrum), with the possibility of introducing station anomalies before location. Nevertheless, a careful study of each time-delay set is

necessary to be sure of its consistency (Chasles relationship). Using this method, the standard error on azimuth is reduced to less than 10 degrees, after correction of an evident cosine azimuthal dependence. This dependence might be due to a dipping structure of the crustal layers under the mini-array.

Similarly, for regional events, the azimuth standard error is less than 3 degrees, for a data set including both Pn and Pg phases.

Finally, we have tested the detection possibilities of the correlation method by using a criterion based on the consistency of the Chasles residuals. It allows us to detect and to identify the later arrivals inside each signal, such as Sn and Sg waves for regional events. Further studies will investigate the potential of this method in some other cases such as a new implementation of the mini-array using 10 stations and also its application to a larger network of regional extension.

References

- Capon, J., High-resolution frequency-wavenumber spectrum analysis., *Proc. IEEE*, **57**, 8, 1969.
- Gupta, I. N., C.S. Lynnes, R. S. Jih, and R. A. Wagner, A study of teleseismic P and P coda from U.S. and Soviet nuclear explosions, paper presented at the 11th Annual ARPA/AFGL Seismic Research Symposium, San Antonio, Texas., 1989.
- Husebye, E.S., Direct measurement of $dT/d\Delta$. *Bull. Seis. Soc. Am.*, **59**, 717-727, 1969.
- Ingate, S.F., E.S. Husebye and A. Christofferson, Regional arrays and optimum data processing schemes, *Bull. Seis. Soc. Am.*, **75**, 1155-1177, 1985.
- Mykkeltveit, S., F. Ringdal, T. Kvaerna and R.W. Alewine, Application of regional arrays in seismic verification, *Bull. Seis. Soc. Am.*, **80**, 1777-1800, 1990.
- Nawab, S.H., F.U. Dowla, et R.T. Lacoss, Direction determination of wideband signals, *IEEE Transactions on acoustics speech and signal processing*, **ASSP-33**, 1985.
- Y. Cansi, J.L. Plantet and B. Massinon, Laboratoire de Détection et de Géophysique, BP12, 91680 Bruyères-le-Châtel, France.

(Received March 12, 1993;
Revised May 21, 1993;
Accepted May 24, 1993.)

**AUTOMATIC PROCESSING OF SEISMIC EVENTS RECORDED
ON A MINI-ARRAY
(SIGNAL ANALYSIS COMBINED WITH NEURAL NETWORKS)**

Y. CANSI and A. BOTTERO
Radiomana
27 Rue C. Bernard
75005 PARIS
Nc 90-0356

OBJECTIVES

Among the different methods used to automatically locate earthquakes recorded on a mini-array, the method based on the broad band F-k analysis is the most common (e.g. : Mykkeltveit et al., 1990). However, this method assumes that the propagation of the considered wave front can be modeled by a plane-wave at the scale of the array. Furthermore, in the case of local model variations (e.g. : station anomalies) the resulting precision is very low because of the large wavelength compared to the array extension. To take into account these difficulties, we have tested another method based on a high precision determination of the arrival-times, from which the event location is derived by a classical Husebye's method which computes the velocity and the azimuth of the wave. Each time-window is processed by this method in different frequency bands and activated only if the arrival-time delay set is consistent. Furthermore, this consistency is used as a signal detector and leads to three time-frequency functions, representing first the consistency, and second the velocity and azimuth when they are available. In the case of teleseismic events, the event location is strictly derived from the determinations of the velocity and the azimuth. But for regional events a phase identification is needed. This task is performed by a neural network which uses the three time-frequency functions as inputs and which leads to an estimate of each phase occurrence possibility as a function of time.

Processing of a set of 28 regional events recorded on the 5-station mini-array worked by the Laboratoire de Détection et de Géophysique of the french Commissariat à l'Energie Atomique led to the following results :

- a very precise determination of the azimuth : standard error is less than 4 degrees;
- a good phase identification capability (especially for P-waves) which leads to an estimation of the distance with a relative error lower than 20%.

RESEARCH ACCOMPLISHED

In 1992, the french Laboratoire de Détection et de Géophysique of the Commissariat à l'Energie Atomique has installed in Central France a temporary mini-array composed of 5 vertical short-period seismometers (Figure 1). Numerical signals are digitized at a rate of 50 cycles per second with a 12-bit dynamic.

This mini-array has recorded more than 100 teleseismic events and about 28 regional events during its 4-months operating period. This experience has provided a useful database for testing different automatic

location methods (Cansi et al., 1992). We have shown that better results are obtained when we use the two-step correlation-method which computes first the arrival-time differences with a high precision (less than the sampling interval 0.02s), and second the azimuth and propagation velocity corrected for statistically determined station anomalies.

1) Data Processing :

For regional events, the correlation functions which define the arrival-time differences often have several relative maxima with comparable amplitudes. This leads to an ambiguity in the arrival-time computation, which can be removed by testing the consistency of the time-delay set, using the Chasles relationship :

$$\Delta t_{ij} + \Delta t_{jk} + \Delta t_{ki} = 0$$

Furthermore, this consistency can be used as a signal detector. When the studied time-window contains a seismic signal, the Root Mean Square of the residuals of the Chasles relations is low (i.e. : less than the sampling interval : it is an estimate of the measurement accuracy). On the opposite, when it contains only noise, no consistency can be found (i.e. : the RMS of Chasles relations is high), because of its low correlation at the scale of the array.

Then, for each 4.5s-time window and for different frequency-bands, we can estimate a probability of signal occurrence, and, in the case of high probability, the corresponding velocity and azimuth. Some examples of these time-frequency functions are displayed on figures 3 and 4. For each time step and for each frequency-band, the velocity is shown (grey scale) only when the consistency is better than 0.02s.

We can see clearly that most of the seismic phases lead to consistent signals whose velocity is well defined for all the available frequency-bands. Nevertheless, some cases are more ambiguous :

- a phase cannot be precisely recognized because the velocity is not clearly defined (see Sn-phase on figure 4),
- a false detection is obtained because a part of the record contains consistent noise with a velocity compatible with the regional phases velocity (see noise on figures 3 and 4 as an example).

Since these two kinds of problems cannot be easily modeled, we have used a "learning system" approach based on a neural network to identify the different phases of each event without ambiguity.

2) Phase Identification :

For neuromimetic applications, the classical programming efforts are transposed to the determination of the various authorised degrees of freedom described as follows :

- the data structure : the first step is to extract from the database the information that are strictly necessary for phase identification. Furthermore, those data have to be invariant by translation, rotation and dilatation, which precludes the analysis on a variable period. The solution we chose is thus to present as inputs and for each time sample the signal velocity for 5 frequency bands (from 0 to 12 Hz). The data whose corresponding Chasles RMS is greater than an arbitrary threshold (i.e. : 0.02 s) are set to 0.

- the network structure : we only used multi-layered perceptrons, with a sigmoid transfer function. They are indeed capable of building complex decision hyper-volumes in the hyper-space of the input data, thus realising an accurate classifier. Several tests led to choose a 2 hidden-layer perceptron. The complexity of the system is due to the high non-linearity of the problem.

- the learning function : we chose as a learning function the "back propagation with momentum" method, which uses a gradient method to minimize the quadratic error between the expected and the observed results. Despite a long computing time, this allows a reliable and accurate learning convergence.

- the example database : it was made of all the available events, excepted 3 of them on which the tests were made. In order to avoid incoherencies, the arrival time of each phase was picked on the time-frequency diagrams ; a phase is thus declared present over the whole time-window between its arrival time and the arrival time of the following phase. Each sample is presented 50000 times in a random order.

- the network topology : the number of nodes in the hidden layers was determined empirically. Several networks were designed : in order to avoid over-training, we chose for each phase the simplest one which did not degrade the results. Finally, the Pn phase requires 24+9 units, the Pg phase 20+6, the Sn phase 16+6 and the Sn phase 20+6 (Figure 2).

All the designing, learning and testing operations were performed using the neural simulator SNNS, developed by the Stuttgart University. The middle diagrams of figures 3 and 4 show the neural outputs as a function of time for two events which were not in the learning database.

3) Distance estimation :

In order to remove the last false detections due to consistent noise, a post data processing is needed to test the consistency of the results on the whole signal, by using the azimuthal information as describe as follows :

- the first step is to compute an azimuth histogram with the possibility functions previously determined and to choose the more probable 20° wide interval. The average azimuth can then be calculated.

- the second step is to refine this approximation by determining the most probable 5° wide sub-interval for each phase. For each time sample, the probability of existence of a phase is set to 0 if the corresponding azimuth is out of those sub-intervals.

The bottom diagrams in figures 3 and 4 show the phase characterization curves after this azimuthal filtering.

At this step, in the function describing the possibility of occurrence of each phase as a function of time, all the information which do not belong to the detected event have been removed. The last step - the distance evaluation - can now be performed.

Each function is differentiated to allow an easy detection of each phase by identifying the times where the derivative is greater than an arbitrary threshold (i.e. : 0.7). When only two phases are detected, the resulting distance is computed using the two times for which the product of the corresponding possibility functions is at its maximum. When more than two phases are detected, a least-squares estimation of the distance is performed for each set of possible arrival-times. The best one is retained as the event distance.

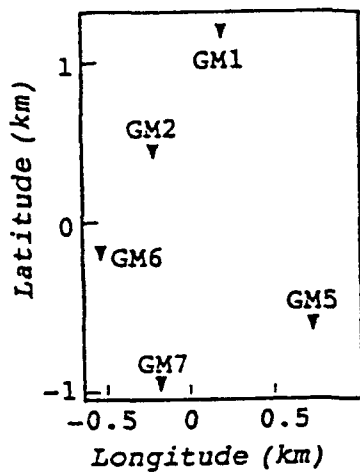
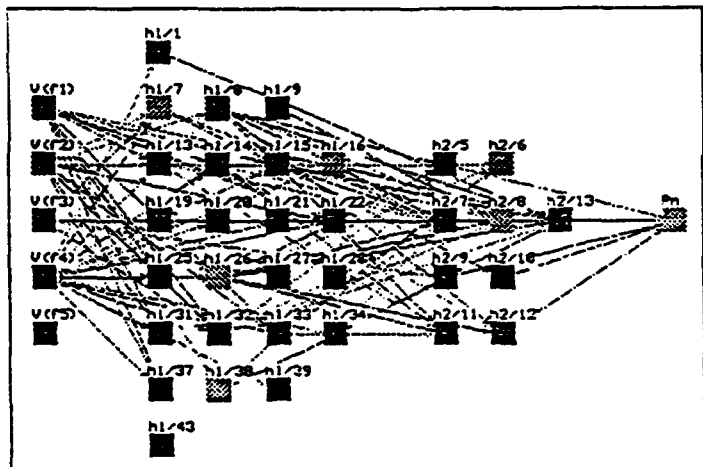
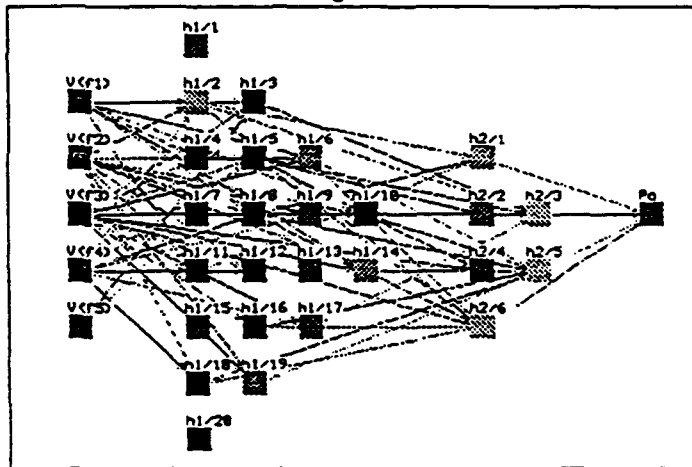


Figure 1 : Network map. It is centred on the point 45.7411N-2.0133E.

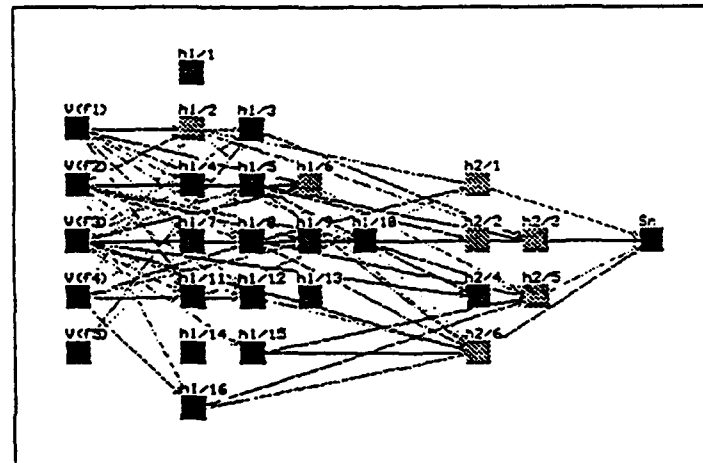
Pn Phase



Pg Phase



Sn Phase



Sg Phase

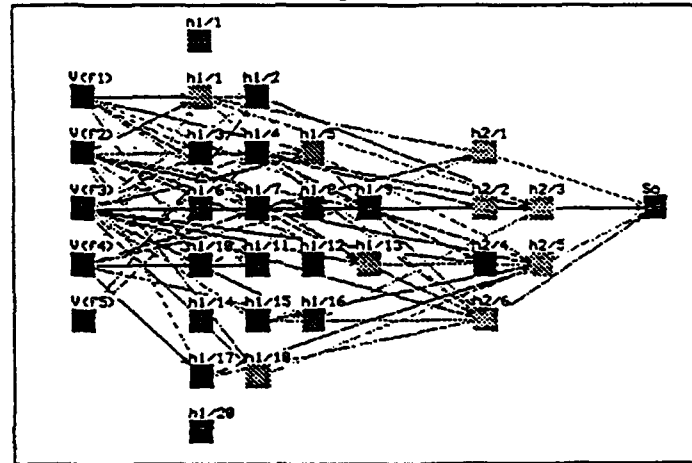


Figure 2 : Design of the neural networks.

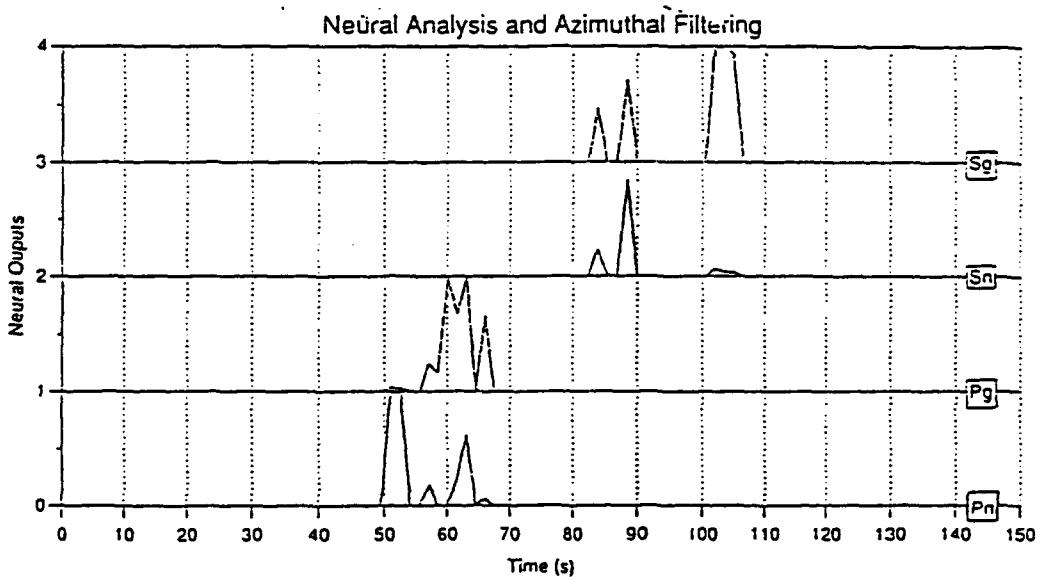
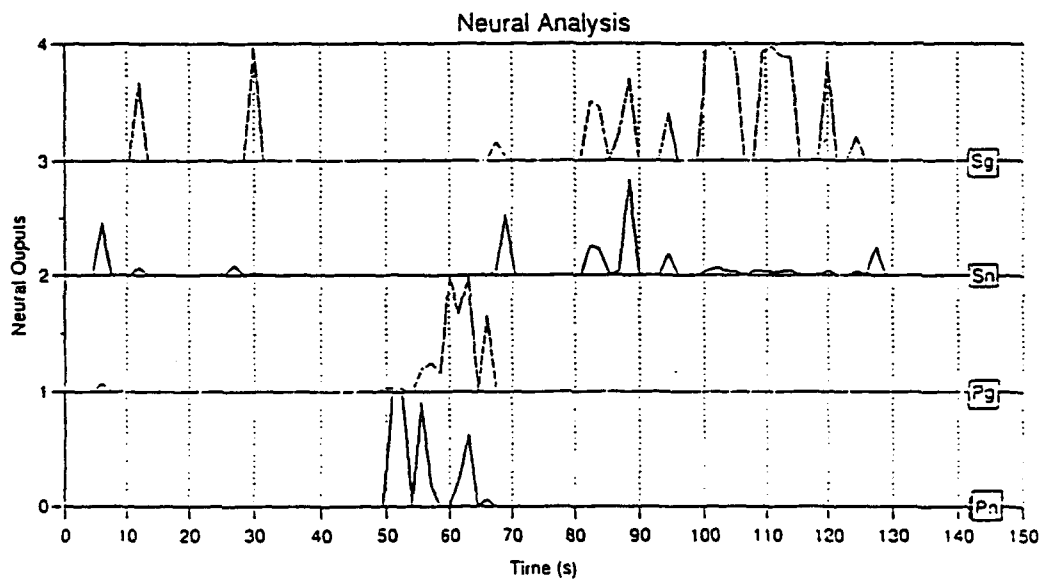
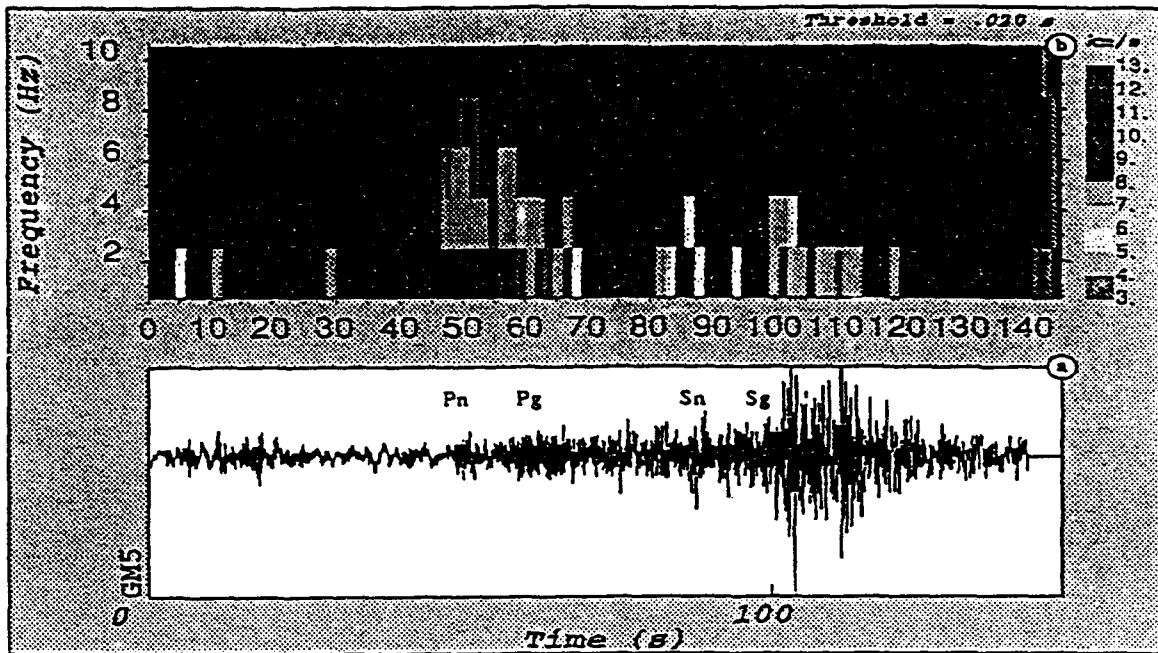


Figure 3 : Example of an event at the different processing levels : the time-frequency plot of the velocity (top), the 4 phase probability functions (middle), and the same after azimuth filtering (bottom).

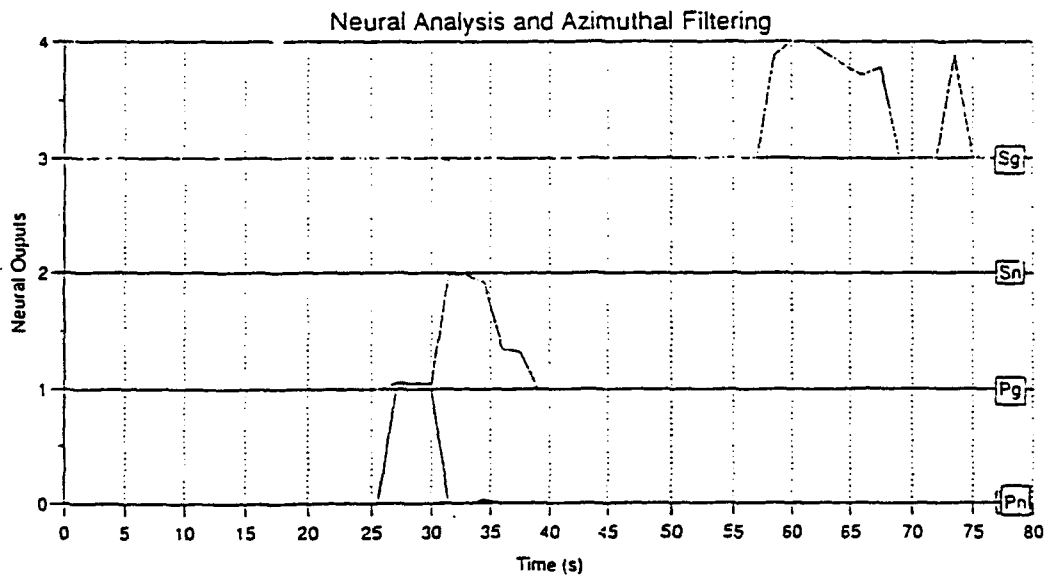
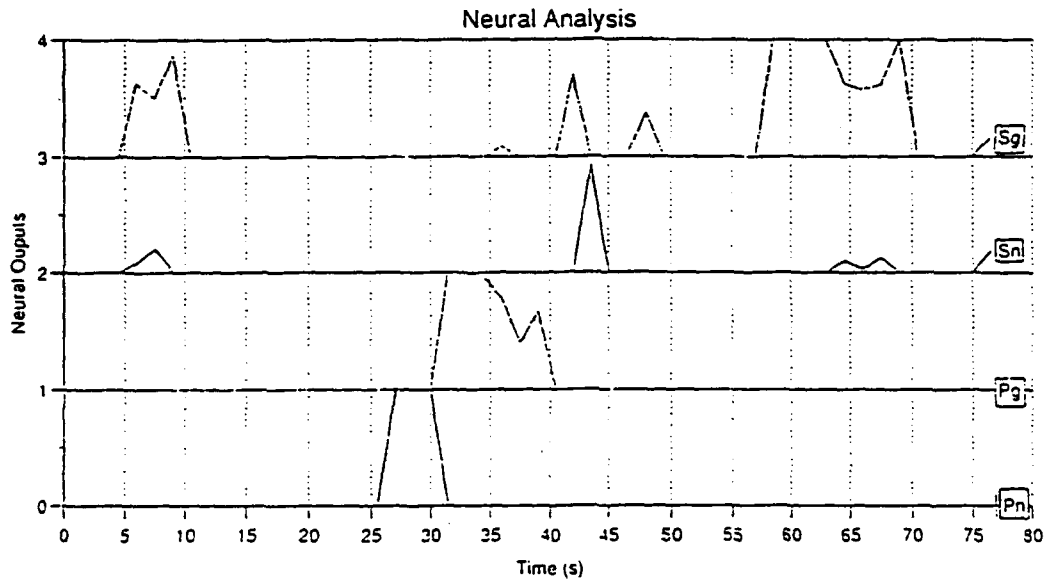
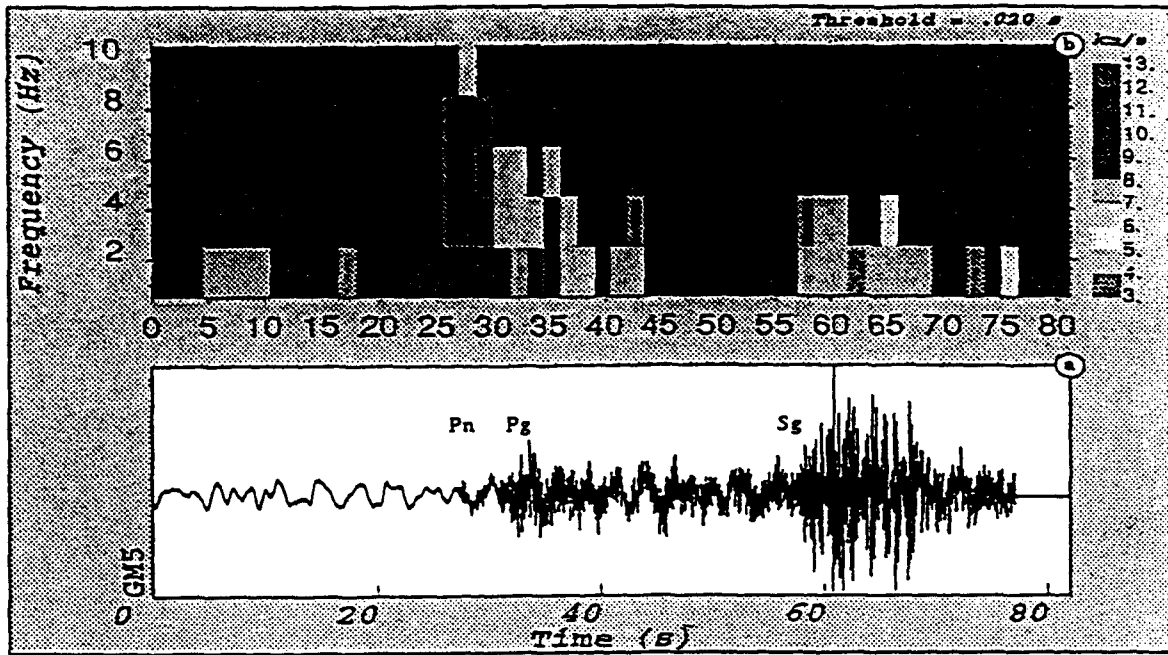


Figure 4 : Example of an event at the different processing levels : the time-frequency plot of the velocity (top), the 4 phase probability functions (middle), and the same after azimuth filtering (bottom).

AZIMUTH EVALUATION

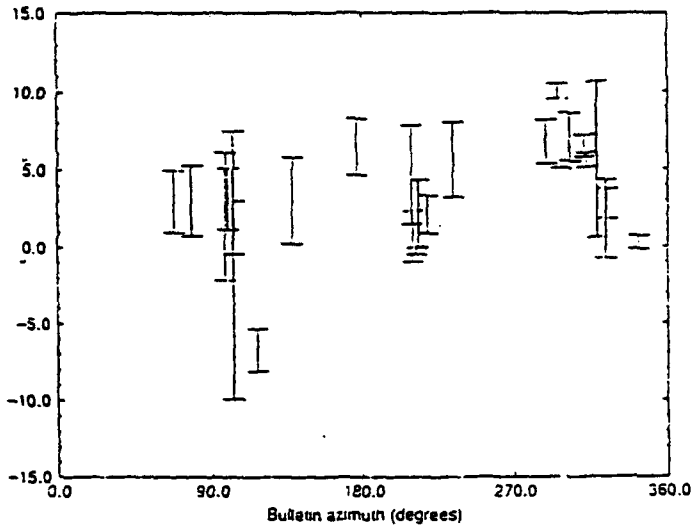


Figure 5 : Azimuth results : azimuth errors versus bulletin azimuths (reference)

DISTANCE EVALUATION

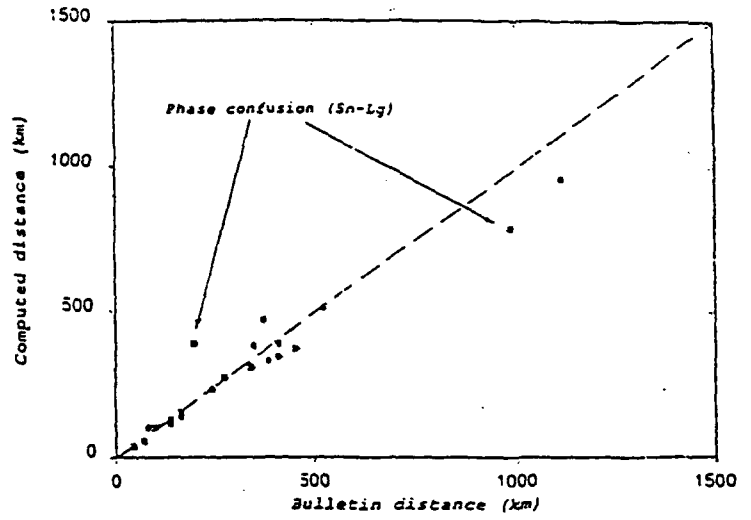


Figure 6 : computed distance (this study) versus bulletin distance (reference).

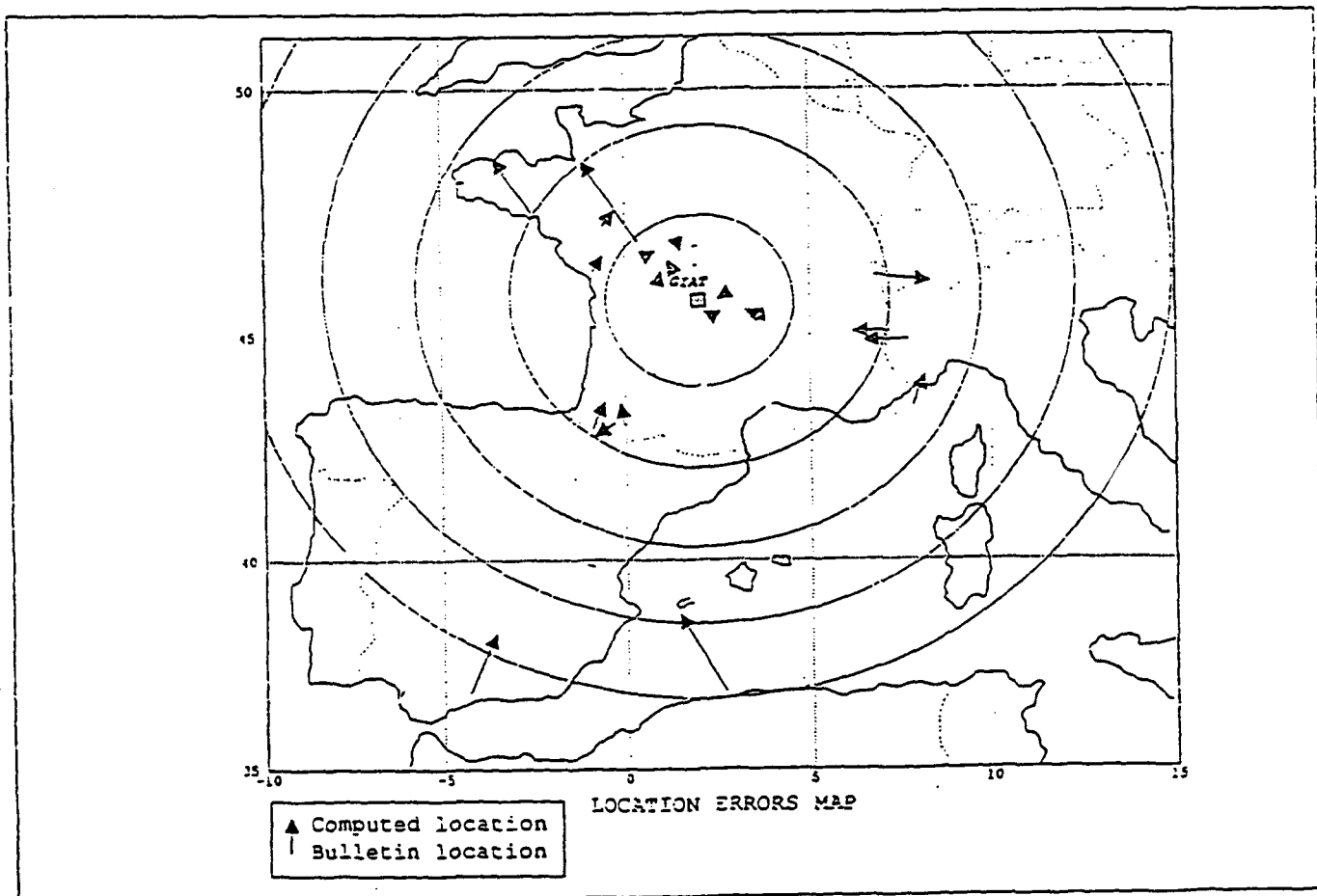


Figure 7 : Regional map showing the location errors for all the events.

THE GIAT MINI-ARRAY IN CENTRAL FRANCE: PRELIMINARY DETECTION AND PHASE IDENTIFICATION RESULTS

René Crusem and Jean-Pierre Massot
Laboratoire de Géophysique
BP 12
91680 Bruyères-le-Châtel
FRANCE

Contract No:
90-0356

OBJECTIVE

The French LDG (Laboratoire de Géophysique) has been installing and operating an experimental mini-array in Central France (GIAT) for seismic Verification and Monitoring purposes, since March, 1993. The objective of the work presented here was to adapt and use the software developed at Norsar, in order to assess the detection capabilities of the GIAT array, both for regional and teleseismic events.

RESEARCH ACCOMPLISHED

Data acquisition and processing:

The French GIAT mini-array presently consists of 9 vertical seismometers, and one 3-components station. Its size is about 3 kilometres (figure 1). The data are digitised at a rate of 50 samples a second, and are stored locally on a personal computer in files containing each about 17 mn of data. Once a file is completed, it is sent to the distant processing centre via phone, where it is automatically written to a Norsar type diskloop. The detection software recognises the arrival of new data, computes a set of filtered beams, and then uses a classical STA/LTA detector on each beam.

Detection configuration:

The results reported here were obtained over a 57 day period, between May 5 and June 30, 1993. During this period, a set of 83 beams was deployed, at different velocities (for regional phases) and for many azimuths. These beams were also attached to different sub-arrays, which were empirically and qualitatively determined according to the frequency content and correlation characteristics of the different wave types and the background noise (Kvaerna,

1989). STA/LTA thresholds were between 4.4 and 7.1 for coherent beams, and between 3.6 and 4.4 for incoherent beams. No horizontal beams could be used, since only one 3 components station was available.

Detection results:

During the period considered, an average of 161 detections was observed each day. Deviations from this mean can be very high (figure 2), due to transient noise occurring on one or more stations (it's origin can be cultural, meteorological, traffic, etc.). The smallest numbers of detections are sometimes observed on Saturdays or Sundays, but this is not always true.

As a reference for estimating detection capabilities, we used the LDG regional and teleseismic bulletins, which are obtained from the whole LDG network (about 40 stations covering France), and which are available and distributed once a week.

Only events for which both a location and a magnitude were reported in these bulletins were used for the comparisons. Thus, 184 regional events and 186 teleseismic events were selected, i.e. an average of about 3 regional events and 3 teleseismic events every day.

An event was declared to be detected by the mini-array if at least one phase was detected by at least one beam. Note that this does NOT mean that such an event could be located or identified automatically by the mini-array.

Results indicate that less than 5 % of all detections can be associated with natural seismic events. Another 5 to 10 % can be attributed to artificial sources such as quarry or rock blasts. In fact, from Mondays to Fridays, the mini-array detected an average of 5 quarry-blasts per day during working hours. Thus, nearly 90 % of all detections were never attributed to a known seismic source.

Detectability of regional events:

Figures 3 and 4 display the preliminary results obtained for regional events. It can be concluded from these figures that the 75% confidence threshold for detection is about $M_l = 3.4$ (M_l is the LDG local magnitude).

This value is about 0.7 magnitude units higher than the value obtained for the whole LDG network, which can be estimated as $M_l = 2.7$ (LDG local magnitude), for distances up to 6 to 8 degrees.

It is instructive to compare this threshold with those reported for the fennoscandian arrays (Mykkeltveit et al. 1990; Uski, 1990), which are close to $M_l = 2.3$ to 2.7 (where M_l is the local magnitude computed for Norway) at the 90% confidence level.

Thus, the difference between the detection capabilities at both sites is presently close to one unit of local magnitude. This is apparently due to the different calibrations used for these local magnitudes, which should be further investigated in the future. Also, there is about a factor two difference in L_g wave attenuation coefficients between Norway and France (Alsaker et al. 1991; Plantet et al. 1991).

Detectability for teleseismic events:

Figures 5 and 6 display the results obtained for the detectability of teleseismic events. The 75% confidence threshold can presently be estimated at $m_b = 4.9$, which is close to the whole LDG network threshold, though the LDG bulletin can probably no longer be used as a reference in the teleseismic case. Anyway, only one event with a magnitude above 5.4 was missed.

These results are close to those reported for GERESS (Gestermann et al. 1991).

Regional phase identification:

Regional phases observed in central France are mainly Pn, Pg, Sg and Lg, while Sn is rarely detected. For Fennoscandian arrays, Norsar uses both phase velocity (obtained from the f-k analysis) and polarisation results in order to identify regional phases. However, this is more difficult for GIAT, since only one (very noisy) 3 components station is available. So, presently, we only use velocities for identifying regional phases.

An analysis of 38 such phases, carefully checked by the analyst, led to the following preliminary rules (velocities are given in km/sec):

```
if VEL < 3.1 then phase is Noise
else: if VEL < 5.8 then phase is S
      if VEL > 3.1 and VEL < 4.2 then phase is Lg
      if VEL > 4.2 and VEL < 5.8 then phase is Sn
else: if VEL > 5.8 then phase is P
      if VEL > 5.8 and VEL < 7.4 then phase is Pg
      if VEL > 7.4 and VEL < 10.5 then phase is Pn
else: if VEL > 10.5 then phase is teleseismic
```

The main ambiguity which may appear is for Sg-Lg versus Sn discrimination, for velocities between 4.2 and 5.2. More experience is now needed before evaluating the performances of these phase identification rules.

CONCLUSIONS AND RECOMMENDATIONS

Despite the fact that the GIAT mini-array consists of only 10 stations, detection results for both regional and teleseismic events are encouraging: the 75 % confidence threshold is $ML=3.4$ for regional and $m_b=4.9$ for teleseismic events.

Such figures could only be obtained due to the high false detection rate (nearly 90%) that was allowed. It is expected that these false detections will be eliminated during the phase association procedure included in the RONAPP software, and that no or little spurious events will be found in the final automatic bulletin.

We are presently trying to further reduce the STA/LTA thresholds, to ameliorate the spike elimination algorithm, and to increase the total number of beams. We plan to run with an average of perhaps 400 detections a day, among

which less than 5% would be associated with real seismic events. We hope that this will further reduce the detection thresholds by about 0.2 to 0.3 magnitude units. However, it is not yet sure whether regional events with such low magnitudes (say 3.1 local LDG magnitude) could be automatically located, since for that purpose at least two phases must be detected.

A longer period of observation, and comparisons with other reference bulletins (for teleseismic events) should confirm these results.

Of course, adding more stations, especially 3-component stations, would also improve the results.

The next step is now to investigate in more details the phase identification and location capabilities of the GIAT mini-array. This will be done using both the classical RONAPP algorithm provided by Norsar, and a novel approach for phase picking and classification based on coherency analysis and neural networks (Cansi et al., 1993).

Finally, before distributing automatic bulletins, it will be necessary to address the important issue of discriminating between quarry blasts and natural seismic events.

Acknowledgement

We want to acknowledge the NORSAR staff, especially Svein Mykkeltveit, Tormod Kvaerna and Jan Fyen, for their hospitality and support during the stay of one of us (R.C.) in October-November 1992, and for kindly providing the NORSAR software package.

References

- Kvaerna, Tormod (1989) - On exploitation of small-aperture Noress type arrays for enhanced P-wave detectability, *Bull. Seismol. Soc. Am.*, 79, 888-900.
- Mykkeltveit, S., F. Ringdal, T. Kvaerna, and R. Alewine (1990) - Application of regional arrays in seismic verification research, *Bull. Seismol. Soc. Am.*, 80, 1777-1800.
- Uski, Marja (1990) - Event detection and location performance of the Finessa array in Finland, *Bull. Seismol. Soc. Am.*, 80, 1818-1832.
- Alsaker, A., L.B. Kvamme, R.A. Hansen, A. Dahle and H. Bungum (1991) - The ML scale in Norway, *Bull. Seismol. Soc. Am.*, 81, 379-398.
- Plantet, J.L., Y. Cansi, and M. Campillo (1991) - Regional seismic wave attenuation and evaluation of seismic sources; in *Recent Advances in Earthquake Engineering and Structural Dynamics*, Ouest Editions, France, ISBN 2-908261-22-7.
- Gestermann, N., H.-P. Harjes, M. Jost, J. Schweitzer, and J. Würster - Analysis of Geress-recordings during GSETT-2, 13th annual PL/DARPA seismic research symposium, 204-210. **PL-TR-91-2208, ADA241325**
- Cansi, Y., and A. Bottero (1993) - Automatic processing of seismic events recorded on a mini-array (signal analysis combined with neural networks); 15th PL/ARPA seismic research symposium, this volume. **PL-TR-93-2160, ADA271458**

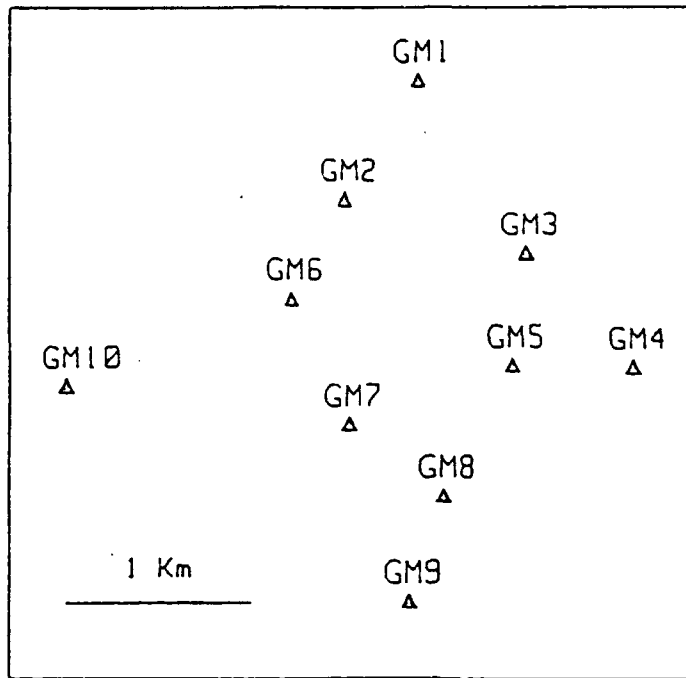


FIGURE 1. Location and geometry of the French GLAT mini-array in central France. The array consists of 9 vertical seismometers, and one "central" 3-components station (GM5). GM5 is located at $45^{\circ}44$ N and $2^{\circ}01$ E.

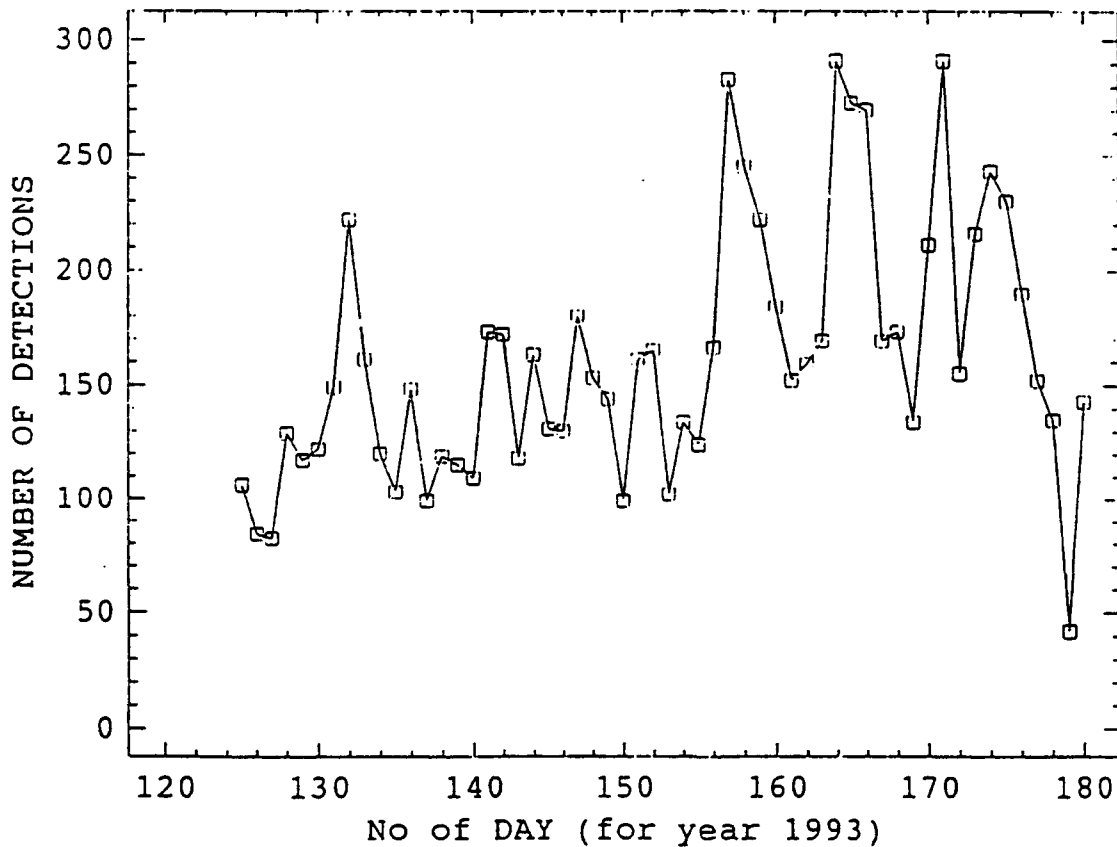


FIGURE 2. Number of detections per day at GLAT, from May 5 to June 30, 1993, deploying a set of 83 beams. Mean is 161. Deviations from the mean by more than a factor 2 are not rare. The effect of weekends does not appear clearly.

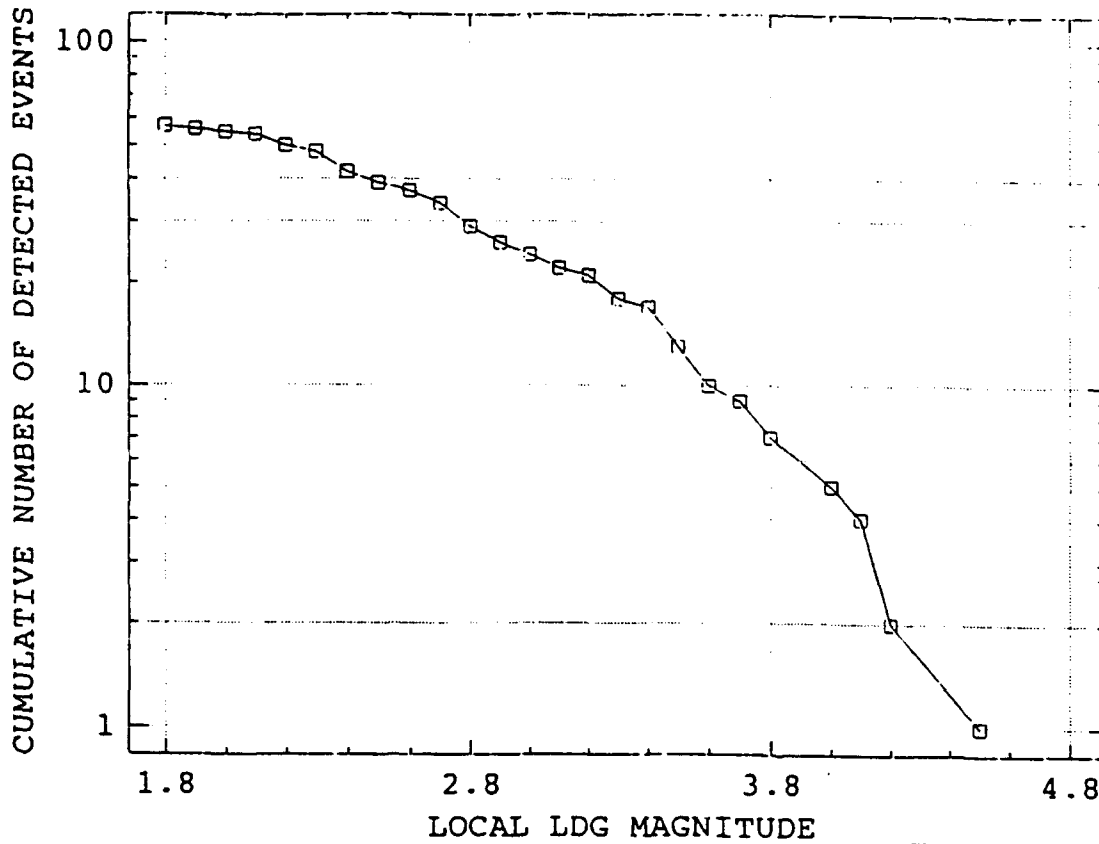


FIGURE 3. Regional event detectability at GIAT. The Y-axis displays the cumulated number of detected events, whose local LDG magnitude is higher than the value specified on the X-axis. Reference is the LDG regional bulletin.

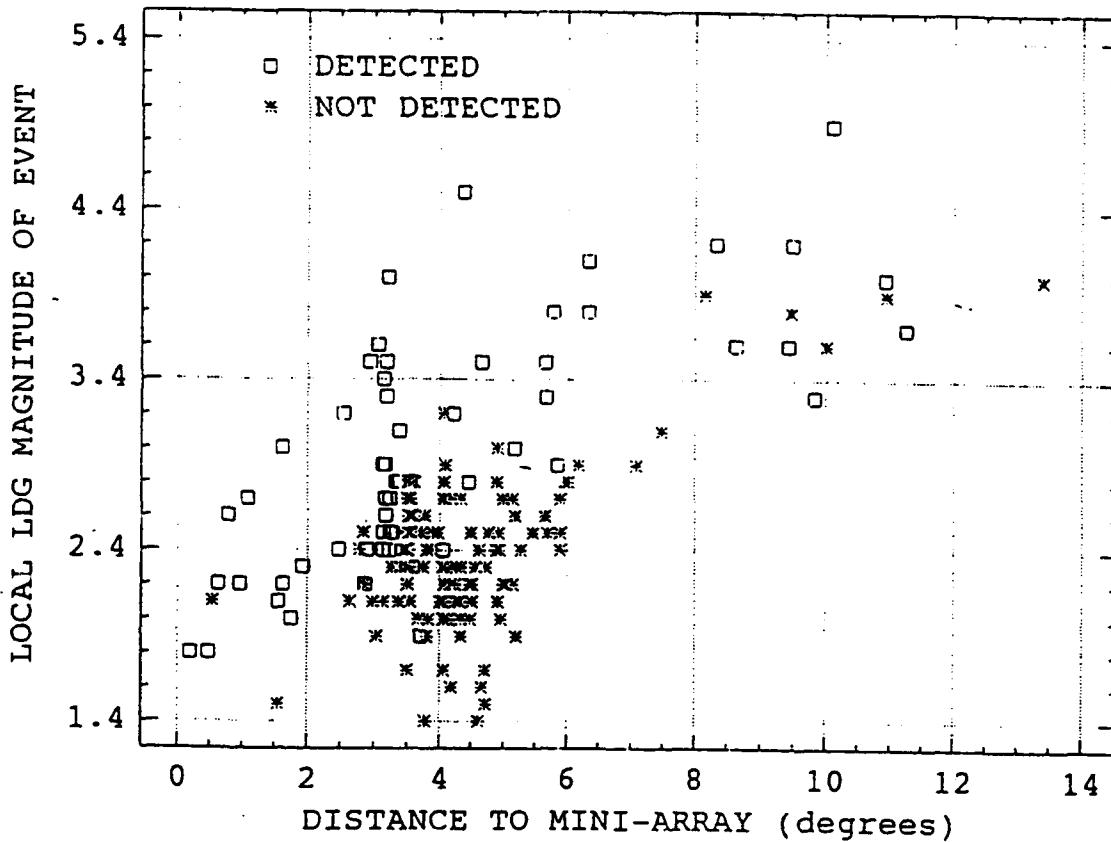


FIGURE 4. Regional event detectability at GIAT. Reference is the LDG regional bulletin. The 75% confidence threshold for detection is 3.4. Up to a distance of 8 degrees, no event with local magnitude greater than 3.2 was missed.

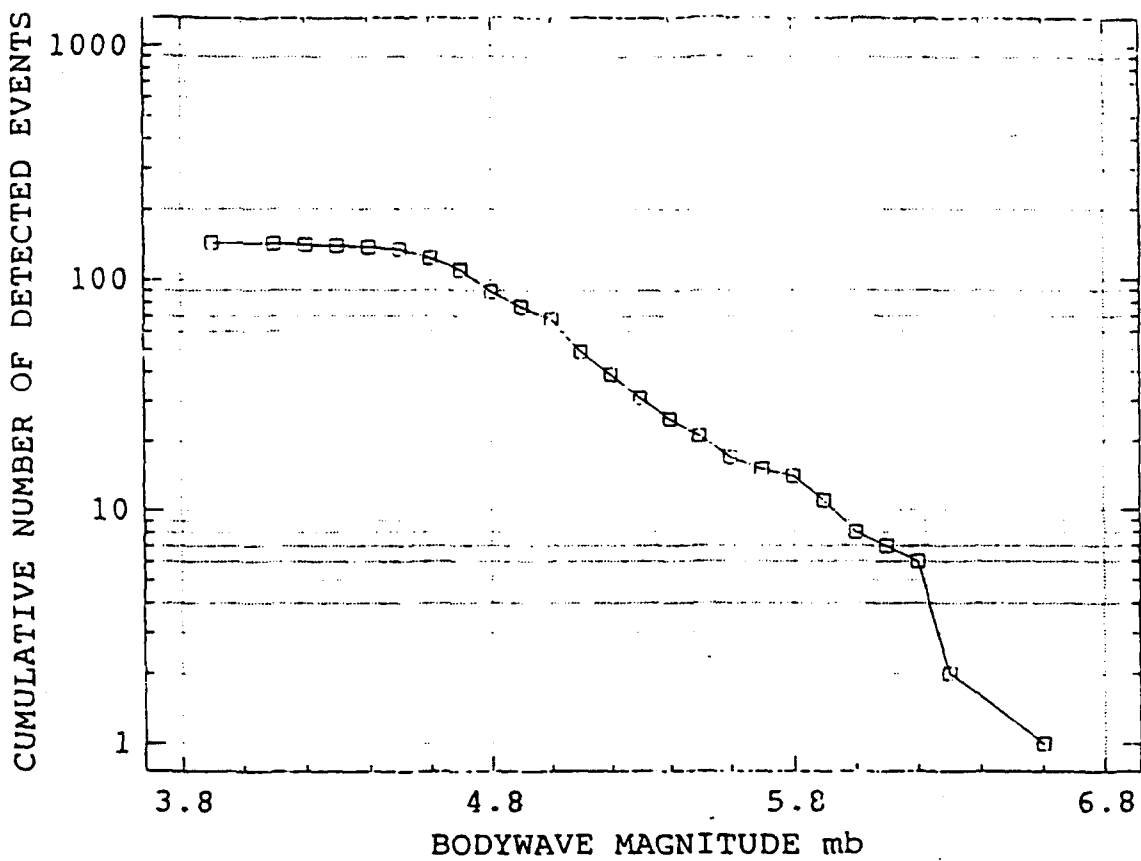


FIGURE 5. Teleseismic event detectability at GIAT. The Y-axis displays the cumulated number of detected events, whose body wave magnitude mb is higher than the value specified on the X-axis. Reference is the LDG teleseismic bulletin. Theoretical relation is linear with a slope equal to -1. Deviation from linearity is observed for an mb of about 4.8 and points out the detection threshold.

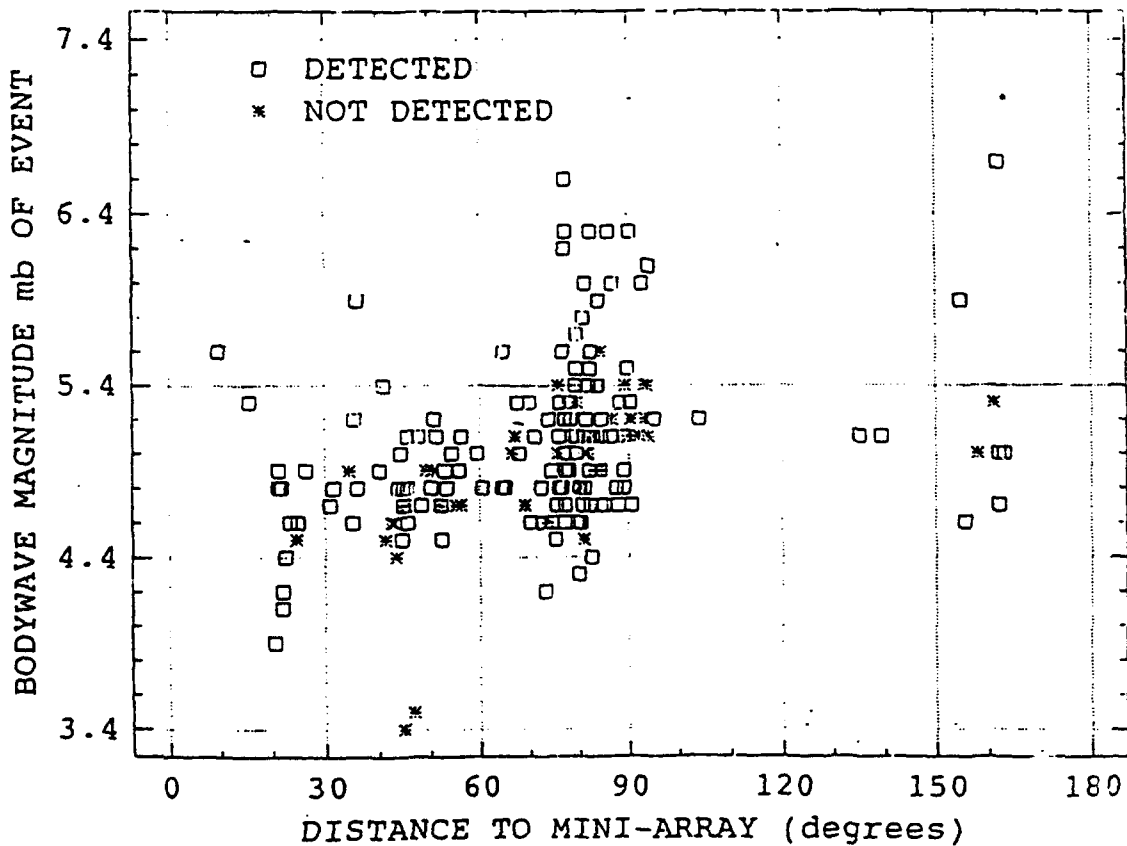


FIGURE 6. Teleseismic event detectability at GIAT. Reference is the LDG teleseismic bulletin. The 75% confidence threshold for detection is 4.9. Up to a distance of 60 degrees, no event with mb greater than 4.9 was missed.

Prof. Thomas Ahrens
Seismological Lab, 252-21
Division of Geological & Planetary Sciences
California Institute of Technology
Pasadena, CA 91125

Prof. Keiiti Aki
Center for Earth Sciences
University of Southern California
University Park
Los Angeles, CA 90089-0741

Prof. Shelton Alexander
Geosciences Department
403 Deike Building
The Pennsylvania State University
University Park, PA 16802

Prof. Charles B. Archambeau
CIRES
University of Colorado
Boulder, CO 80309

Dr. Thomas C. Bache, Jr.
Science Applications Int'l Corp.
10260 Campus Point Drive
San Diego, CA 92121 (2 copies)

Prof. Muawia Barazangi
Institute for the Study of the Continent
Cornell University
Ithaca, NY 14853

Dr. Jeff Barker
Department of Geological Sciences
State University of New York
at Binghamton
Vestal, NY 13901

Dr. Douglas R. Baumgardt
ENSCO, Inc
5400 Port Royal Road
Springfield, VA 22151-2388

Dr. Susan Beck
Department of Geosciences
Building #77
University of Arizona
Tucson, AZ 85721

Dr. T.J. Bennett
S-CUBED
A Division of Maxwell Laboratories
11800 Sunrise Valley Drive, Suite 1212
Reston, VA 22091

Dr. Robert Blandford
AFTAC/TT, Center for Seismic Studies
1300 North 17th Street
Suite 1450
Arlington, VA 22209-2308

Dr. Stephen Bratt
ARPA/NMRO
3701 North Fairfax Drive
Arlington, VA 22203-1714

Dr. Lawrence Burdick
IGPP, A-025
Scripps Institute of Oceanography
University of California, San Diego
La Jolla, CA 92093

Dr. Robert Burrige
Schlumberger-Doll Research Center
Old Quarry Road
Ridgefield, CT 06877

Dr. Jerry Carter
Center for Seismic Studies
1300 North 17th Street
Suite 1450
Arlington, VA 22209-2308

Dr. Eric Chael
Division 9241
Sandia Laboratory
Albuquerque, NM 87185

Dr. Martin Chapman
Department of Geological Sciences
Virginia Polytechnical Institute
21044 Derring Hall
Blacksburg, VA 24061

Mr Robert Cockerham
Arms Control & Disarmament Agency
320 21st Street North West
Room 5741
Washington, DC 20451,

Prof. Vernon F. Cormier
Department of Geology & Geophysics
U-45, Room 207
University of Connecticut
Storrs, CT 06268

Prof. Steven Day
Department of Geological Sciences
San Diego State University
San Diego, CA 92182

Marvin Denny
U.S. Department of Energy
Office of Arms Control
Washington, DC 20585

Dr. Zoltan Der
ENSCO, Inc.
5400 Port Royal Road
Springfield, VA 22151-2388

Prof. Adam Dziewonski
Hoffman Laboratory, Harvard University
Dept. of Earth Atmos. & Planetary Sciences
20 Oxford Street
Cambridge, MA 02138

Prof. John Ebel
Department of Geology & Geophysics
Boston College
Chestnut Hill, MA 02167

Eric Fielding
SNEE Hall
INSTOC
Cornell University
Ithaca, NY 14853

Dr. Petr Firbas
Institute of Physics of the Earth
Masaryk University Brno
Jecna 29a
612 46 Brno, Czech Republic

Dr. Mark D. Fisk
Mission Research Corporation
735 State Street
P.O. Drawer 719
Santa Barbara, CA 93102

Prof. Donald Forsyth
Department of Geological Sciences
Brown University
Providence, RI 02912

Dr. Art Frankel
U.S. Geological Survey
922 National Center
Reston, VA 22092

Dr. Cliff Frolich
Institute of Geophysics
8701 North Mopac
Austin, TX 78759

Dr. Holly Given
IGPP, A-025
Scripps Institute of Oceanography
University of California, San Diego
La Jolla, CA 92093

Dr. Jeffrey W. Given
SAIC
10260 Campus Point Drive
San Diego, CA 92121

Dr. Dale Glover
Defense Intelligence Agency
ATTN: ODT-1B
Washington, DC 20301

Dan N. Hagedorn
Pacific Northwest Laboratories
Battelle Boulevard
Richland, WA 99352

Dr. James Hannon
Lawrence Livermore National Laboratory
P.O. Box 808
L-205
Livermore, CA 94550

Prof. David G. Harkrider
Seismological Laboratory
Division of Geological & Planetary Sciences
California Institute of Technology
Pasadena, CA 91125

Prof. Danny Harvey
CIRES
University of Colorado
Boulder, CO 80309

Prof. Donald V. Helmberger
Seismological Laboratory
Division of Geological & Planetary Sciences
California Institute of Technology
Pasadena, CA 91125

Prof. Eugene Herrin
Institute for the Study of Earth and Man
Geophysical Laboratory
Southern Methodist University
Dallas, TX 75275

Prof. Robert B. Herrmann
Department of Earth & Atmospheric Sciences
St. Louis University
St. Louis, MO 63156

Prof. Lane R. Johnson
Seismographic Station
University of California
Berkeley, CA 94720

Prof. Thorne Lay
Institute of Tectonics
Earth Science Board
University of California, Santa Cruz
Santa Cruz, CA 95064

Prof. Thomas H. Jordan
Department of Earth, Atmospheric &
Planetary Sciences
Massachusetts Institute of Technology
Cambridge, MA 02139

Dr. William Leith
U.S. Geological Survey
Mail Stop 928
Reston, VA 22092

Prof. Alan Kafka
Department of Geology & Geophysics
Boston College
Chestnut Hill, MA 02167

Mr. James F. Lewkowicz
Phillips Laboratory/GPEH
29 Randolph Road
Hanscom AFB, MA 01731-3010(2 copies)

Robert C. Kemerait
ENSCO, Inc.
445 Pineda Court
Melbourne, FL 32940

Mr. Alfred Lieberman
ACDA/VI-OA State Department Building
Room 5726
320-21st Street, NW
Washington, DC 20451

Dr. Karl Koch
Institute for the Study of Earth and Man
Geophysical Laboratory
Southern Methodist University
Dallas, Tx 75275

Prof. L. Timothy Long
School of Geophysical Sciences
Georgia Institute of Technology
Atlanta, GA 30332

Dr. Max Koontz
U.S. Dept. of Energy/DP 5
Forrestal Building
1000 Independence Avenue
Washington, DC 20585

Dr. Randolph Martin, III
New England Research, Inc.
76 Olcott Drive
White River Junction, VT 05001

Dr. Richard LaCoss
MIT Lincoln Laboratory, M-200B
P.O. Box 73
Lexington, MA 02173-0073

Dr. Robert Masse
Denver Federal Building
Box 25046, Mail Stop 967
Denver, CO 80225

Dr. Fred K. Lamb
University of Illinois at Urbana-Champaign
Department of Physics
1110 West Green Street
Urbana, IL 61801

Dr. Gary McCartor
Department of Physics
Southern Methodist University
Dallas, TX 75275

Prof. Charles A. Langston
Geosciences Department
403 Deike Building
The Pennsylvania State University
University Park, PA 16802

Prof. Thomas V. McEvelly
Seismographic Station
University of California
Berkeley, CA 94720

Jim Lawson, Chief Geophysicist
Oklahoma Geological Survey
Oklahoma Geophysical Observatory
P.O. Box 8
Leonard, OK 74043-0008

Dr. Art McGarr
U.S. Geological Survey
Mail Stop 977
U.S. Geological Survey
Menlo Park, CA 94025

Dr. Keith L. McLaughlin
S-CUBED
A Division of Maxwell Laboratory
P.O. Box 1620
La Jolla, CA 92038-1620

Stephen Miller & Dr. Alexander Florence
SRI International
333 Ravenswood Avenue
Box AF 116
Menlo Park, CA 94025-3493

Prof. Bernard Minster
IGPP, A-025
Scripps Institute of Oceanography
University of California, San Diego
La Jolla, CA 92093

Prof. Brian J. Mitchell
Department of Earth & Atmospheric Sciences
St. Louis University
St. Louis, MO 63156

Mr. Jack Murphy
S-CUBED
A Division of Maxwell Laboratory
11800 Sunrise Valley Drive, Suite 1212
Reston, VA 22091 (2 Copies)

Dr. Keith K. Nakanishi
Lawrence Livermore National Laboratory
L-025
P.O. Box 808
Livermore, CA 94550

Prof. John A. Orcutt
IGPP, A-025
Scripps Institute of Oceanography
University of California, San Diego
La Jolla, CA 92093

Prof. Jeffrey Park
Kline Geology Laboratory
P.O. Box 6666
New Haven, CT 06511-8130

Dr. Howard Patton
Lawrence Livermore National Laboratory
L-025
P.O. Box 808
Livermore, CA 94550

Dr. Frank Pilotte
HQ AFTAC/TT
1030 South Highway A1A
Patrick AFB, FL 32925-3002

Dr. Jay J. Pulli
Radix Systems, Inc.
201 Perry Parkway
Gaithersburg, MD 20877

Dr. Robert Reinke
ATTN: FCTVTD
Field Command
Defense Nuclear Agency
Kirtland AFB, NM 87115

Prof. Paul G. Richards
Lamont-Doherty Geological Observatory
of Columbia University
Palisades, NY 10964

Mr. Wilmer Rivers
Teledyne Geotech
314 Montgomery Street
Alexandria, VA 22314

Dr. Alan S. Ryall, Jr.
ARPA/NMRO
3701 North Fairfax Drive
Arlington, VA 22203-1714

Dr. Richard Sailor
TASC, Inc.
55 Walkers Brook Drive
Reading, MA 01867

Prof. Charles G. Sammis
Center for Earth Sciences
University of Southern California
University Park
Los Angeles, CA 90089-0741

Prof. Christopher H. Scholz
Lamont-Doherty Geological Observatory
of Columbia University
Palisades, NY 10964

Dr. Susan Schwartz
Institute of Tectonics
1156 High Street
Santa Cruz, CA 95064

Secretary of the Air Force
(SAFRD)
Washington, DC 20330

Office of the Secretary of Defense
DDR&E
Washington, DC 20330

Thomas J. Sereno, Jr.
Science Application Int'l Corp.
10260 Campus Point Drive
San Diego, CA 92121

Dr. Michael Shore
Defense Nuclear Agency/SPSS
6801 Telegraph Road
Alexandria, VA 22310

Dr. Robert Shumway
University of California Davis
Division of Statistics
Davis, CA 95616

Dr. Matthew Sibol
Virginia Tech
Seismological Observatory
4044 Derring Hall
Blacksburg, VA 24061-0420

Prof. David G. Simpson
IRIS, Inc.
1616 North Fort Myer Drive
Suite 1050
Arlington, VA 22209

Donald L. Springer
Lawrence Livermore National Laboratory
L-025
P.O. Box 808
Livermore, CA 94550

Dr. Jeffrey Stevens
S-CUBED
A Division of Maxwell Laboratory
P.O. Box 1620
La Jolla, CA 92038-1620

Lt. Col. Jim Stobie
ATTN: AFOSR/NL
110 Duncan Avenue
Bolling AFB
Washington, DC 20332-0001

Prof. Brian Stump
Institute for the Study of Earth & Man
Geophysical Laboratory
Southern Methodist University
Dallas, TX 75275

Prof. Jeremiah Sullivan
University of Illinois at Urbana-Champaign
Department of Physics
1110 West Green Street
Urbana, IL 61801

Prof. L. Sykes
Lamont-Doherty Geological Observatory
of Columbia University
Palisades, NY 10964

Dr. David Taylor
ENSCO, Inc.
445 Pineda Court
Melbourne, FL 32940

Dr. Steven R. Taylor
Los Alamos National Laboratory
P.O. Box 1663
Mail Stop C335
Los Alamos, NM 87545

Prof. Clifford Thurber
University of Wisconsin-Madison
Department of Geology & Geophysics
1215 West Dayton Street
Madison, WS 53706

Prof. M. Nafi Toksoz
Earth Resources Lab
Massachusetts Institute of Technology
42 Carleton Street
Cambridge, MA 02142

Dr. Larry Turnbull
CIA-OSWR/NED
Washington, DC 20505

Dr. Gregory van der Vink
IRIS, Inc.
1616 North Fort Myer Drive
Suite 1050
Arlington, VA 22209

Dr. Karl Veith
EG&G
5211 Auth Road
Suite 240
Suitland, MD 20746

Prof. Terry C. Wallace
Department of Geosciences
Building #77
University of Arizona
Tucson, AZ 85721

Dr. Thomas Weaver
Los Alamos National Laboratory
P.O. Box 1663
Mail Stop C335
Los Alamos, NM 87545

Phillips Laboratory
ATTN: GPE
29 Randolph Road
Hanscom AFB, MA 01731-3010

Dr. William Wortman
Mission Research Corporation
8560 Cinderbed Road
Suite 700
Newington, VA 22122

Phillips Laboratory
ATTN: TSML
5 Wright Street
Hanscom AFB, MA 01731-3004

Prof. Francis T. Wu
Department of Geological Sciences
State University of New York
at Binghamton
Vestal, NY 13901

Phillips Laboratory
ATTN: PL/SUL
3550 Aberdeen Ave SE
Kirtland, NM 87117-5776 (2 copies)

Prof Ru-Shan Wu
University of California, Santa Cruz
Earth Sciences Department
Santa Cruz
, CA 95064

Dr. Michel Bouchon
I.R.I.G.M.-B.P. 68
38402 St. Martin D'Herès
Cedex, FRANCE

ARPA, OASB/Library
3701 North Fairfax Drive
Arlington, VA 22203-1714

Dr. Michel Campillo
Observatoire de Grenoble
I.R.I.G.M.-B.P. 53
38041 Grenoble, FRANCE

HQ DNA
ATTN: Technical Library
Washington, DC 20305

Dr. Kin Yip Chun
Geophysics Division
Physics Department
University of Toronto
Ontario, CANADA

Defense Intelligence Agency
Directorate for Scientific & Technical Intelligence
ATTN: DTIB
Washington, DC 20340-6158

Prof. Hans-Peter Harjes
Institute for Geophysics
Ruhr University/Bochum
P.O. Box 102148
4630 Bochum 1, GERMANY

Defense Technical Information Center
Cameron Station
Alexandria, VA 22314 (2 Copies)

Prof. Eystein Husebye
NTNF/NORSAR
P.O. Box 51
N-2007 Kjeller, NORWAY

TACTEC
Battelle Memorial Institute
505 King Avenue
Columbus, OH 43201 (Final Report)

David Jepsen
Acting Head, Nuclear Monitoring Section
Bureau of Mineral Resources
Geology and Geophysics
G.P.O. Box 378, Canberra, AUSTRALIA

Phillips Laboratory
ATTN: XPG
29 Randolph Road
Hanscom AFB, MA 01731-3010

Ms. Eva Johannisson
Senior Research Officer
FOA
S-172 90 Sundbyberg, SWEDEN

Dr. Peter Marshall
Procurement Executive
Ministry of Defense
Blacknest, Brimpton
Reading FG7-FRS, UNITED KINGDOM

Dr. Bernard Massinon, Dr. Pierre Mechler
Societe Radiomana
27 rue Claude Bernard
75005 Paris, FRANCE (2 Copies)

Dr. Svein Mykkeltveit
NTNT/NORSAR
P.O. Box 51
N-2007 Kjeller, NORWAY (3 Copies)

Prof. Keith Priestley
University of Cambridge
Bullard Labs, Dept. of Earth Sciences
Madingley Rise, Madingley Road
Cambridge CB3 0EZ, ENGLAND

Dr. Jorg Schlittenhardt
Federal Institute for Geosciences & Nat'l Res.
Postfach 510153
D-30631 Hannover , GERMANY

Dr. Johannes Schweitzer
Institute of Geophysics
Ruhr University/Bochum
P.O. Box 1102148
4360 Bochum 1, GERMANY

Trust & Verify
VERTIC
Carrara House
20 Embankment Place
London WC2N 6NN, ENGLAND